UNIVERSIDADE FEDERAL DE SÃO CARLOS

CENTRO DE CIÊNCIAS EXATAS E DE TECNOLOGIA
DEPARTAMENTO DE QUÍMICA

PROGRAMA DE PÓS-GRADUAÇÃO EM QUÍMICA

"DOPAGEM E FORMAÇÃO DE HETEROJUNÇÕES COMO ESTRATÉGIAS PARA O MELHORAMENTO DA PROPRIEDADE FOTOCATALÍTICA DE Ag_3PO_4".

Aline Barrios Trench*

Tese apresentada como parte dos requisitos para obtenção do título de DOUTOR EM CIÊNCIAS, área de concentração: FÍSICO–QUÍMICA

Orientador: Prof. Dr. Elson Longo

*** bolsista CAPES**

São Carlos - SP

2022

UNIVERSIDADE FEDERAL DE SÃO CARLOS

Centro de Ciências Exatas e de Tecnologia
Programa de Pós-Graduação em Química

Folha de Aprovação

Defesa de Tese de Doutorado da candidata Aline Barrios Trench, realizada em 27/06/2022.

Comissão Julgadora:

Prof. Dr. Elson Longo da Silva (UFSCar)

Prof. Dr. Mauro Coelho dos Santos (UFABC)

Prof. Dr. Miguel Ángel San-Miguel Barrera (UNICAMP)

Prof. Dr. Luís Fernando da Silva (UFSCar)

Prof. Dr. Valmor Roberto Mastelaro (IFSC/USP)

O Relatório de Defesa assinado pelos membros da Comissão Julgadora encontra-se arquivado junto ao Programa de Pós-Graduação em Química.

“O pensamento positivo e otimista somente nos traz confiança e esperança para um mundo melhor”

AGRADECIMENTOS

Agradeço primeiramente a Deus pela minha vida e bênçãos concedidas a mim,

aos meus pais, Edson e Zezé e à minha tia Pita por todo amor, apoio e incentivo,

ao meu marido, Vinícius, por me apoiar, ajudar e me proporcionar tantos momentos felizes,

à Graxa e Maju por me proporcionarem alegria todos os dias,

aos meus irmãos Estela e Bruno, que sempre torceram por mim,

ao prof. Elson Longo pelos ensinamentos científicos e pessoais,

ao prof, Juan Andrés pelos ensinamentos e por ter aceitado ser meu orientador no exterior,

aos meus amigos Cleiton, Lala, Laís, Lúcia, Roger, Lorena, Rodrigo, Camilinha (*In memoriam*) e Fiama por todo o carinho e paciência,

a todos meus colegas de laboratório,

à Secretaria de Pós-Graduação pelo suporte oferecido,

ao CDMF e a UJI pela excelente infraestrutura oferecida para o desenvolvimento das pesquisas,

à CAPES pela bolsa concedida.

RESUMO

DOPAGEM E FORMAÇÃO DE HETEROJUNÇÕES COMO ESTRATÉGIAS PARA O MELHORAMENTO DA PROPRIEDADE FOTOCATALÍTICA DE Ag_3PO_4. Nos últimos anos, a crescente atividade tecnológica e industrial em setores como farmacêutico e têxtil tem acarretado em efeitos colaterais ao ambiente e à saúde humana. Tais efeitos são relacionados à geração de resíduos nocivos e seus descartes inapropriados ao ambiente, principalmente aquático, impactando diretamente a saúde humana e animal. Dentre diversos processos para tratamento destes resíduos, a fotocatálise heterogênea tem sido considerada um método efetivo para tal propósito. Com isto, a busca por novos materiais e o melhoramento das propriedades de fotocatalisadores tem crescido abruptamente. Devido à sua intrínseca atividade fotocatalítica para a degradação de compostos orgânicos, o fosfato de prata (Ag_3PO_4) tem sido amplamente pesquisado com o intuito de melhoramento de suas propriedades para o tratamento de efluentes contaminados. A formação de heterojunção entre semicondutores e também, a dopagem destes, têm se mostrado eficientes no melhoramento da atividade fotocatalítica do Ag_3PO_4 para a degradação de corantes e fármacos. Desta forma, este estudo tem como principal objetivo a modificação do Ag_3PO_4 por meio da dopagem com tungstênio (W) e separadamente, por meio da formação de heterojunção com tungstato de prata (α-Ag_2WO_4). Em ambos os trabalhos, os materiais foram sintetizados pelo método de co-precipitação química e como principais resultados, a dopagem de W na estrutura do Ag_3PO_4 provocou a formação de clusters [AgO_4], [PO_4] e [WO_4] desordenados, os quais geram níveis de energia intermediários na região do *band gap*. Estes níveis retardam o processo de recombinação do par elétron-buraco, resultando na melhoria na performance fotocatalítica dos materiais dopados para a degradação do corante Rodamina B, do antibiótico Cefalexina e do pesticida Imidacloprido, sob irradiação de luz visível. Além disto, a presença de W no Ag_3PO_4 apresentou um aumento de 16 vezes na performance bactericida contra a bactéria *Staphylococcus aureus* resistente à meticilina. Para a formação de heterojunção, foi observado que o material contendo 24% m/m de α-Ag_2WO_4 apresentou atividade fotocatalítica superior para a degradação do corante Rodamina B, em comparação aos materiais separados. Baseado nos potenciais de redução das bandas de valência e de condução do α-Ag_2WO_4 e Ag_3PO_4, obtidos experimentalmente pelo método de eletronegatividade de Mulliken, foi proposto o mecanismo de transferência de cargas de heterojunção do tipo I para estes materiais. Além disto, foi observada a formação de nanopartículas de prata metálica na interface dos semicondutores, atuando como uma ponte e aumentando a transferência e separação de cargas entre os semicondutores. Desta forma, neste estudo foi possível a obtenção de materiais fotocatalisadores e o melhoramento das propriedades fotocatalíticas do Ag_3PO_4 por meio da dopagem com W e da formação de heterojunção com o α-Ag_2WO_4.

Palavras-chave: Fosfato de prata. Dopagem. Heterojunção.

ABSTRACT

DOPING AND HETEROJUNCTION FORMATION AS STRATEGIES TO IMPROVE THE PHOTOCATALYTIC PROPERTY OF Ag_3PO_4. In recent years, the growing technological and industrial activities in sectors such as pharmaceuticals and textiles have shown side effects on the environment and human health. Such effects are related to the generation of harmful waste and its inappropriate disposal to the environment, mainly aquatic, directly impacting human and animal health. Among several processes for the treatment of these residues, heterogeneous photocatalysis has been considered an effective method for this purpose. With this, the search for new materials and the improvement of the properties of photocatalysts have grown abruptly. Due to its intrinsic photocatalytic activity for the degradation of organic compounds, silver phosphate (Ag_3PO_4) has been widely researched in order to improve its properties for the treatment of contaminated effluents. The formation of heterojunctions between semiconductors and also their doping have been shown to be efficient in improving the photocatalytic activity of Ag_3PO_4 for the degradation of dyes and drugs. Thus, this study had as main objective the modification of Ag_3PO_4 through doping with tungsten (W) and separately, through the formation of heterojunction with silver tungstate (α-Ag_2WO_4). In both works, the materials were synthesized by the chemical co-precipitation method and as main results, the doping of W in the Ag_3PO_4 structure caused the formation of disordered [AgO_4], [PO_4], and [WO_4] clusters, which generate intermediate energy levels in the band gap region. These levels delay the electron-hole pair recombination process, resulting in an improvement in the photocatalytic performance of doped materials for the degradation of Rhodamine B dye, Cephalexin antibiotic, and Imidacloprid pesticide, under visible light irradiation. In addition, the presence of W in Ag_3PO_4 showed a 16-fold increase in bactericidal performance against methicillin-resistant *Staphylococcus aureus* bacteria. For the formation of heterojunction, it was observed that the material containing 24 wt% of α-Ag_2WO_4 showed superior photocatalytic activity for the degradation of Rhodamine B dye compared to the separated materials. Based on the reduction potentials of the valence and conduction bands of α-Ag_2WO_4 and Ag_3PO_4, obtained experimentally by the Mulliken electronegativity method, a type I heterojunction charge transfer mechanism was proposed for these materials. In addition, the formation of metallic silver nanoparticles at the semiconductors interface was observed, acting as a bridge and increasing the transfer and separation of charges between the semiconductors. Thus, in this study it was possible to obtain photocatalyst materials and improve the photocatalytic properties of Ag_3PO_4 through doping with W and the formation of heterojunction with α-Ag_2WO_4.

Keywords: Silver phosphate. Doping. Heterojunction.

SUMÁRIO

1 – PUBLICATIONS

1.1 – Thesis Publications

1- Trench, Aline B.; Machado, Thales R.; Gouveia, Amanda F.; Foggi, Camila C.; Teodoro, Vinícius; Sánchez-Montes, Isaac; Teixeira, Mayara M.; Da Trindade, Letícia G.; Jacomaci, Natalia; Perrin, Andre; Perrin, Christiane; Aquino, Jose M.; Andrés, Juan; Longo, Elson. Rational Design of W-Doped Ag_3PO_4 as an Efficient Antibacterial Agent and Photocatalyst for Organic Pollutant Degradation. ACS Omega, v. 5, p. 23808-23821, 2020.

2 - Trench, Aline B.; Alvarez, Roman; Teodoro, Vinícius; Da Trindade, Letícia G.; Machado, Thales R.; Teixeira, Mayara M.; De Souza, Daniele; Pinatti, Ivo M.; Simões, Alexandre Z.; Gobato, Yara Galvão; Andrés, Juan ; Longo, Elson . Interface matters: Design of an efficient α-Ag_2WO_4/Ag_3PO_4 photocatalyst. MATERIALS CHEMISTRY AND PHYSICS, v. 280, p. 125710, 2022.

1.2 – Another Publications

3 - Teodoro, Vinícius; Gouveia, Amanda Fernandes; Machado, Thales Rafael; Trench, Aline Barrios; Jacomaci, Natalia; Assis, Marcelo; Marques, Gilmar Eugenio; Teodoro, Marcio Daldin; San-Miguel, Miguel Angel; Andrés, Juan; Bettini, Jefferson; Longo, Elson. Connecting morphology and photoluminescence emissions in β-Ag_2MoO_4 microcrystals. CERAMICS INTERNATIONAL, v. 48, p. 3740-3750, 2022.

4 - Trench, Aline Barrios; Teodoro, Vinícius; Da Trindade, Let'cia Guerreiro; Machado, Thales Rafael; Minguez-Vega, Gladys; Cordoncillo, Eloisa; Donate-Buendia, Carlos; Andres, Juan; Longo, Elson. High photocatalytic activity of Ag/Ag_3PO_4:W heterostructure formed by femtosecond laser irradiation. Ecletica Química Journal, v. 47, p. 20-27, 2022.

5 - Da Trindade, Letícia G.; Borba, Katiúscia M.N.; Trench, Aline B.; Zanchet, Letícia; Teodoro, Vinícius ; Pontes, Fenelon M.L. ; Longo, Elson ; Mazzo, Tatiana M. . Effective strategy to coupling Zr-MOF/ZnO: Synthesis, morphology and photoelectrochemical properties evaluation. JOURNAL OF SOLID STATE CHEMISTRY, v. 293, p. 121794, 2021.

6 - Pinatti, Ivo M.; Trench, Aline B.; Tello, Ana C. M.; Pereira, Paula F. S.; Souza, Josiane C.; Teodoro, Marcio D.; Rosa, Ieda L. V.; Andrés, Juan; Longo, Elson; Simões, Alexandre Z. . Structure, Photoluminescence Emissions, and Photocatalytic Activity of Ag SeO : A Joint Experimental and Theoretical Investigation. Inorganic Chemistry, v. 60, p. 5937-5954, 2021.

7 - Teodoro, Vinícius; Barrios Trench, Aline; Guerreiro Da Trindade, Letícia; Jacomaci, Natalia; Beltran-Mir, Hector; Andrés, Juan; Cordoncillo, Eloisa; Bettini, Jefferson; Longo, Elson. Behavior of Bi_2S_3 under ultrasound irradiation for Rhodamine B dye degradation. CHEMICAL PHYSICS LETTERS, v. 785, p. 139123, 2021.

8 - Pinatti, Ivo M.; Tello, Ana C.M.; Trench, Aline B.; De Foggi, Camila C.; Pereira, Paula F.S.; Teixeira, Mayara M.; Jacomaci, Natalia; Andrés, Juan ; Longo, Elson. Zinc-substituted Ag_2CrO_4: A material with enhanced photocatalytic and biological activity. JOURNAL OF ALLOYS AND COMPOUNDS, v. 835, p. 155315, 2020.

9 - Da Silva, Jussara S.; Machado, Thales R.; Trench, Aline B.; Silva, Airton D.; Teodoro, Vinícius; Vieira, Paulo C. ; Martins, Tiago A. ; Longo, Elson. Enhanced photocatalytic and antifungal activity of hydroxyapatite/α-$AgVO_3$ composites. MATERIALS CHEMISTRY AND PHYSICS, v. 252, p. 123294, 2020.

10 - Da Trindade, L. G.; Christinelli, W. A.; Zanchet, L.; Coelho, D.; Trench, A. B.; Martini, Emilse M. A.; Correa, Daniel S.; Mattoso, Luiz H. C.; Pereira, E. C. . The effect of alkyl chain of the imidazolium ring on the poly(o-methoxyaniline)/ionic liquid supercapacitor performance. JOURNAL OF SOLID STATE ELECTROCHEMISTRY, v. 23, p. 1109, 2019.

11 - Da Trindade, Letícia G.; Borba, Katiúscia M.N.; Zanchet, Letícia; Lima, Demétrius W.; Trench, Aline B.; Rey, Fernando ; Diaz, Urbano ; Longo, Elson; Bernardo-Gusmão, Katia; Martini, Emilse M.A. . SPEEK-based proton exchange membranes modified with MOF-encapsulated ionic liquid. MATERIALS CHEMISTRY AND PHYSICS, v. 236, p. 121792, 2019.

12 - Da Trindade, Letícia G.; Minervino, Gabriela B.; Trench, Aline B.; Carvalho, Maria H.; Assis, Marcelo; Li, Máximo S.; De Oliveira, Adilson J.A.; Pereira, Ernesto C.; Mazzo, Tatiana

M.; Longo, Elson. Influence of ionic liquid on the photoelectrochemical properties of ZnO particles. CERAMICS INTERNATIONAL, v. 44, p. 10393-10401, 2018.

13 - Trench, Aline Barrios; Machado, Thales Rafael; Gouveia, Amanda Fernandes; Assis, Marcelo; Da Trindade, Letícia Guerreiro; Santos, Clayane ; Perrin, Andre; Perrin, Christiane; Oliva, Mónica; Andrés, Juan; Longo, Elson. Connecting structural, optical, and electronic properties and photocatalytic activity of Ag_3PO_4 :Mo complemented by DFT calculations. APPLIED CATALYSIS B-ENVIRONMENTAL, v. 238, p. 198-211, 2018.

14 - Da Trindade, Letícia G.; Zanchet, Letícia; Trench, Aline B. ; Souza, Josiane Carneiro; Carvalho, Maria H.; De Oliveira, Adilson J. A.; Pereira, Ernesto C.; Mazzo, Tatiana M.; Longo, Elson. Flower-like ZnO/ionic liquid composites: structure, morphology, and photocatalytic activity. IONICS, v. 1, p. 1-14, 2018.

15 - Gonçalves, R.; Christinelli, W.A.; Trench, A.B.; Cuesta, A.; Pereira, E.C. . Properties improvement of poly(o-methoxyaniline) based supercapacitors: experimental and theoretical behaviour study of self-doping effect. ELECTROCHIMICA ACTA, v. 228, p. 57-65, 2017.

16 - Christinelli, W.A.; Da Trindade, L.G.; Trench, A.B.; Quintans, C.S.; Paranhos, C.M.; Pereira, E.C. . High-performance energy storage of poly (o-methoxyaniline) film using an ionic liquid as electrolyte. ENERGY, v. 141, p. 1829-1835, 2017.

17 - Christinelli, Wania Ap.; Trench, Aline B.; Pereira, Ernesto C. . Electrochromic properties of poly(o-methoxyaniline)-poly(3-thiophene acetic acid) layer by layer films. SOLAR ENERGY MATERIALS AND SOLAR CELLS, v. 157, p. 703-708, 2016.

18 - Marreto, Paola D.; Trench, Aline B.; Vicentini, Fernando C.; Figueiredo-Filho, Luiz C. S.; Medeiros, Roberta A.; Pereira, Ernesto. C.; Fatibello-Filho, Orlando. Square-Wave Voltammetric Determination of Nanomolar Levels of Linuron in Environmental Water Samples Using a Glassy Carbon Electrode Modified with Platinum Nanoparticles within a Dihexadecyl Phosphate Film. Australian Journal of Chemistry (Print), v. 68, p. 800, 2015

19 - Sartori, Elen Romão; Trench, Aline Barrios; Rocha-Filho, Romeu C.; Fatibello-Filho, Orlando. Determination of Propylthiouracil In Pharmaceuticals By Differential Pulse

Voltammetry Using A Cathodically Pretreated Boron-Doped Diamond Electrode. Journal of the Brazilian Chemical Society (Impresso), v. 24, p. 1504-1511, 2013.

20 - Braz, E. J. R. S.; Santos, V. B.; Trench, A. B.; Fatibello Filho, O. . Construção de Uma Célula Eletrolítica para o Ensino de Eletrólise a Partir de Materiais de Baixo Custo. Quimica Nova na Escola, v. 35, p. 107-111, 2012.

2 – INTRODUCTION

Water is an essential asset to life and needs to be preserved. However, with rapid industrial and population growth and the effects of climate change, water sources have been threatened [1, 2]. Thus, the reuse of contaminated water is extremely important for today's society.

Among the various pollutants existing in contaminated water, industrial waste stands out for being more toxic and non-biodegradable when compared to municipal waste, as it consists of heavy metals, fats, oils, greases, phenols, and ammonia. [3]. Residues from agriculture, pharmaceutical, and textile industries release herbicides, drugs, and dyes into effluents that are responsible for chronic diseases that are harmful to human health [4], and it is very important to carry out adequate water treatments to remove these organic pollutants. However, the presence of these pollutants in surface water, groundwater, and in municipal sewage treatment plants [5] demonstrates the inefficiency of conventional treatments used, and the development of efficient methods is of paramount importance.

There are different treatment methods for the removal of organic pollutants, such as membrane filtration [6], adsorption [7], biological methods, such as phytoremediation [8] and bioaugmentation [9], chemical methods, such as chemical precipitation [10] and chemical coagulation [11], and advanced oxidation processes (AOPs) [12]. The AOPs are ecologically correct methodologies for the removal of organic pollutants and stand out when compared to conventional methods as they generate thermodynamically stable oxidation products, such as carbon dioxide, water, and biodegradable organics [13].

Photocatalysis stands out among AOPs due to its simplicity, low cost, reproducibility, being non-toxic, and having high efficiency in degrading organic pollutants [14, 15]. Heterogeneous photocatalysis is based on the activation of a semiconductor by means of light absorption with energy greater than or equal to the band-gap energy of the semiconductor. In this way, the electrons are photoexcited from the valence band (VB) to the conduction band (CB), generating holes in the VB. These holes are highly oxidizing and can be actively used in the degradation of organic pollutants. Furthermore, adsorbed water molecules can be oxidized by the holes in the VB, generating hydroxyl radicals. In CB, adsorbed oxygen can be reduced by photoexcited electrons, generating superoxide ions, which can react with protons from water oxidation to form a hydroperoxyl radical. These reactive oxygen species (ROS) generated during the photocatalysis process can also act to degrade organic pollutants along with the holes. [16]. Thus, photocatalysis process can take advantage of solar energy for

the degradation of pollutants, making this methodology economically viable. Since the discovery of the photoelectrochemical water separation reaction using the TiO_2 semiconductor by Fujishima and Honda in 1972, photocalysis has advanced rapidly [1]. Since then, semiconductors such as doped TiO_2 [17] and other metal oxides such ZnO [18], SnO_2 [19], Bi_2O_3 [20], and WO_3 [21] were used as photocatalysts for the degradation of organic pollutants. However, studies show that there are some disadvantages in using these semiconductors such as (1) fast electron/hole pair recombination, resulting in a lower number of photogenerated ROS to perform the photodegradation process, impairing the photocatalytic efficiency and (2) low absorption in the visible region due to the high band gap value of these semiconductors, making it impossible to use sunlight in photocatalytic processes [22]. These factors affected the practical use of these semiconductors, making the search for efficient photocatalysts of great relevance.

In 2010, the use of the Ag_3PO_4 photocatalyst for the degradation of organic pollutants using visible light was reported for the first time [23]. Since then, several studies aiming to explore its photocatalytic applications have been reported [24, 25]. Studies aimed at investigating the main surface responsible for the high photocatalytic activity of Ag_3PO_4 indicate that the surface (110) is the main responsible. This is due to its high reactivity caused by the presence of a large amount of undercoordinated Ag cations [26, 27].

The crystal structure of Ag_3PO_4 was first investigated in 1925 by Wyckoff, being established as a body-centered cubic structure with a P4-3n space group and a lattice parameter of approximately 6.004 Å [23]. This semiconductor has an indirect band gap of 2.36 eV and a direct band gap of 2.43 eV. The VB of Ag_3PO_4 (+2.85 V vs. NHE) is positive enough to generate the hydroxyl radical, which can act in the degradation of organic pollutants along with the photogenerated holes [24]. On the other hand, the CB of Ag_3PO_4 (+0.45 V vs. NHE) is more positive than the potential $O_2/\bullet O_2$ (−0.046 eV vs. NHE), so the electrons could only reduce the Ag^+ from the Ag_3PO_4 crystal lattice, leading to the Ag^0 deposition on the semiconductor surface. This phenomenon, known as photocorrosion, destroys the structure of Ag_3PO_4, in addition to reducing the light absorption capacity of Ag_3PO_4, which directly influences its photocatalytic activity and stability [23]. In addition, this semiconductor has low efficiency in the separation of photogenerated electron/hole pairs due to rapid recombination [28].

To overcome these challenges and improve the photocatalytic property of Ag_3PO_4, different types of modifications were carried out, such as morphology control [29], cation/anion doping, and heterojunction construction. Doping is considered an efficient way to improve the photocatalytic activity of materials. In this method, ions (cations or anions) are

introduced into the structure of the material, which can generate defects in the semiconductor. The defects generated can act as capture centers, preventing the recombination of photogenerated electron/hole pairs. In addition, these defects can increase the material's ability to absorb light in the visible region, as well as cause significant changes in the material's band gap energy value. Zhang *et al*.[30] reported that the introduction of Bi^{3+} ions can replace the P^{5+} ions of Ag_3PO_4, resulting in a decrease in band gap energy. Doping with 2 wt% of Bi achieved a degradation of 90.7% of methyl orange after 6 minutes of visible light irradiation, whereas pure Ag_3PO_4 degraded only 27.3% under the same conditions. Song and contributors [31] reported that doping with Ni^{2+} generated an impurity energy band that facilitated the use of photons, as well as the efficiency of charge carrier separation. The photodegradation efficiency of methyl orange under visible light irradiation was 89% in 4 minutes for the doped material, while for pure Ag_3PO_4 it was only 12%. In another study, Masaoudi *et al.* [32] investigated the doping of Ag_3PO_4 with Cu and it was observed that the band gap of the doped nanoparticles was reduced. This resulted in increased photocatalytic degradation of Rhodamine-B under visible light due to increased production of hydroxyl and superoxide radicals. Afif and contributors [33] doped Ag_3PO_4 with Mn and the results showed that this insertion decreased the broad absorption in the visible region. Furthermore, the surface hydroxyl defects and oxygen vacancies of Ag_3PO_4 were compensated by Mn doping, increasing the photocatalytic activity under visible light irradiation of the doped samples. Trench *et al*.[34] observed that doping with Mo generated defects in the structure of Ag_3PO_4 that led to the formation of new intermediate energy levels between VB and CB. The new levels generated served as a trap for the electron/hole pairs, preventing their recombination and consequently improving the photocatalytic performance of the doped materials. Thus, it becomes evident that doping is an efficient approach to improve the photocatalytic properties of Ag_3PO_4. Another approach considered efficient to improve the photocatalytic property of Ag_3PO_4 is the coupling with another semiconductor to form a heterojunction [35]. The junction of two semiconductors can enhance their individual photocatalytic properties, since the separation and transfer of electron/hole pairs can be more effective. In addition, high band gap energy semiconductors can be coupled to smaller band gap semiconductors, forming a visible light active photocatalyst [24].

The types of heterojunctions can be defined by the positions of the VB and CB of the semiconductors and by their electron affinities. As can be seen in image 1, in type I heterojunction, the position of the CB of semiconductor A is greater than the CB of semiconductor B. On the other hand, VB of semiconductor A is lower than VB of

semiconductor B. In this way, under light irradiation, the photogenerated electrons in semiconductor A migrate to CB from semiconductor B and the photogenerated holes in semiconductor A migrate to VB from semiconductor B. In type II heterojunction, the CB and VB levels of semiconductor A are higher than the CB and VB levels of semiconductor B. In this way, the photogenerated electrons in semiconductor A will migrate to the CB in semiconductor B, while the photogenerated holes in semiconductor B will migrate to the VB of semiconductor A. In type III heterojunction, the positions of CB and VB of semiconductor

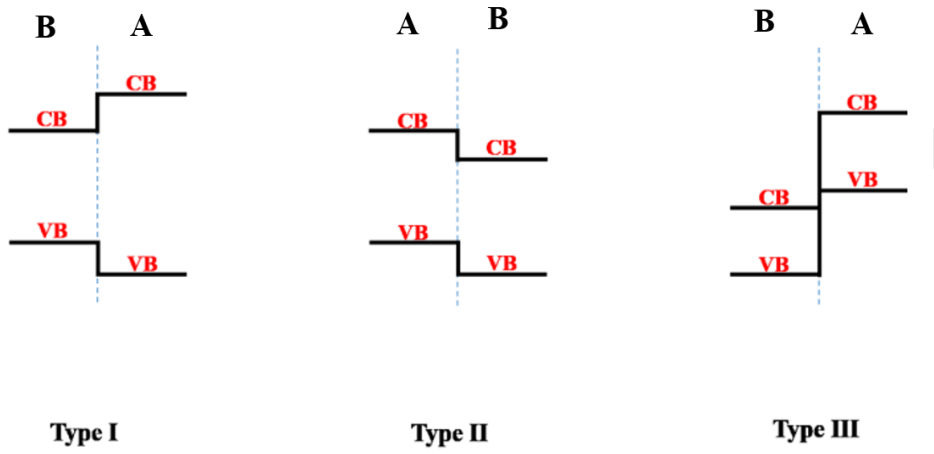

A are much higher than the VB and CB of semiconductor B, making it impossible for the electron/hole pairs to migrate. Thus, because this type of heterojunction does not allow separation and charge transfer, it becomes unsuitable for photocatalytic improvement [36].

Figure 1. Types of heterojunction (adapted from Li *et al*.[24])

Several studies have addressed the use of heterojunctions (type I and II) of Ag_3PO_4 in order to produce a photocatalyst with photocatalytic properties superior to those of isolated materials. Li *et al*. [37] developed a $SrCoO_3/Ag_3PO_4$ heterojunction by the hydrothermal method and the photocatalytic activity of this material was tested for tetracycline degradation under visible light irradiation. The $SrCoO_3/Ag_3PO_4$ heterojunction (1:1.5) showed a tetracycline degradation rate constant that is 1.7 times greater than Ag_3PO_4 and 3.78 times greater than $SrCoO_3$. This result was related to the higher separation rate of photogenerated electron/hole pairs. Chi and contributors [38] studied the heterojunction of porous TiO_2/Ag_3PO_4 nanotubes for methylene blue photodegradation. The heterojunctions showed higher photocatalytic activities than the isolated materials and this efficiency was due to the

formation of a Z-scheme type mechanism between the two semiconductors. Li *et al.*[39] investigated the heterojunction of $Ag_3PO_4/BiNbO_4$ for the photodegradation of Rhodamine B under irradiation of a solar simulator. The heterojunctions showed excellent photocatalytic performance, the best response being presented for a sample containing 10 wt% of $BiNbO_4$, which degraded 100% of the dye in 30 minutes. Santos and contributors [40] reported that the Ag_3PO_4/NiO heterojunction showed excellent photocatalytic efficiency compared to pure materials. The higher photocatalytic activity was related to the low recombination of the electron/hole pairs due to the formation of a type I heterojunction. In this way, the construction of heterojunctions can be an efficient way to improve the photocatalytic performance of Ag_3PO_4.

The silver tungstate (Ag_2WO_4) is a semiconductor of the oxoargentate family and presents polymorphism, with the phases known as α-Ag_2WO_4, β-Ag_2WO_4, and γ-Ag_2WO_4. The α-Ag_2WO_4 phase is thermodynamically stable and the phases β-Ag_2WO_4 and γ-Ag2WO_4 are considered metastable [41, 42]. The structure of α-Ag_2WO_4 was identified by Cavalcante *et al.* [43] and is composed of octahedral clusters of [WO_6] and clusters of [AgO_n] (n = 7, deltahedral [AgO_7]; n = 6, octahedral [AgO_6]; n= 4, tetrahedral [AgO_4], and n = 2, angular [AgO_2]) [44]. This phase receives special attention because it has different applications such as luminescent [45], antimicrobials [46], and sensors [47]. In addition, α-Ag_2WO_4 has photocatalytic property for the degradation of organic pollutants [44, 48, 49], but has disadvantages by absorbing small amount of visible light due to its high band gap energy and low stability due to photocorrosion [50].

As reported above, doping is an efficient method to improve the photocatalytic property of a semiconductor. In this sense, the tungsten element (W) can be used as a dopant for this purpose. Demircivi *et al*. [51] reported the doping of $BaTiO_3$ with W for photocatalytic degradation of tetracycline. The doping improved the photocatalytic property of $BaTiO_3$, leading to a degradation of 80% in 180 minutes. In another study, Shan and contributors [52] observed the same effect of doping with W on the photocatalytic property of $BiVO_4$ for degradation of dyes.

Thus, this study had as main objective the modification of Ag_3PO_4 through doping with W and separately, through the formation of heterojunction with α-Ag_2WO_4 to improve the photocatalytic activity of Ag_3PO_4.

3 – PUBLISHED ARTICLES

The published articles that compose this doctoral thesis with the associated experimental approach are found at the following pages.

3.1 – Rational Design of W-Doped Ag_3PO_4 as an Efficient Antibacterial Agent and Photocatalyst for Organic Pollutant Degradation.

ACS OMEGA

http://pubs.acs.org/journal/acsodf Article

Rational Design of W-Doped Ag_3PO_4 as an Efficient Antibacterial Agent and Photocatalyst for Organic Pollutant Degradation

Aline B. Trench,* Thales R. Machado,* Amanda F. Gouveia, Camila C. Foggi, Vinícius Teodoro, Isaac Sánchez-Montes, Mayara M. Teixeira, Letícia G. da Trindade, Natalia Jacomaci, Andre Perrin, Christiane Perrin, Jose M. Aquino, Juan Andrés, and Elson Longo*

Cite This: *ACS Omega* 2020, 5, 23808–23821 Read Online

Rational Design of W-Doped Ag_3PO_4 as an Efficient Antibacterial Agent and Photocatalyst for Organic Pollutant Degradation

Aline B. Trench,* Thales R. Machado,* Amanda F. Gouveia, Camila C. Foggi, Vinícius Teodoro, Isaac Sanchez-Montes, Mayara M. Teixeira, Letícia G. da Trindade, Natalia Jacomaci, Andre Perrin, Christiane Perrin, Jose M. Aquino, Juan Andres, and Elson Longo´*

*Corresponding Authors

Aline B. Trench – CDMF Department of Chemistry, Federal University of São Carlos, 13565-905 São Carlos, SP, Brazil; Email: aline_trench@hotmail.com

Thales R. Machado – CDMF Department of Chemistry, Federal University of São Carlos, 13565-905 São Carlos, SP, Brazil; orcid.org/0000-0002-3246-6329; Email: tmachado.quimica@gmail.com

Elson Longo – CDMF Department of Chemistry, Federal University of São Carlos, 13565-905 São Carlos, SP, Brazil; orcid.org/0000-0001-8062-7791; Email: elson.liec@ gmail.com

Authors

Amanda F. Gouveia − Institute of Chemistry, State University of Campinas, 13083-970 Campinas, SP, Brazil; orcid.org/ 0000-0003-3441-3674

Camila C. Foggi – CDMF Department of Chemistry, Federal University of Sao Carlos, 13565-905 São Carlos, SP, Brazil; orcid.org/0000-0002-1210-1234

Vinícius Teodoro – CDMF Department of Chemistry, Federal University of Sao Carlos, 13565-905 Sa˜ o Carlos, SP, Brazil

Isaac Sánchez-Montes − Department of Chemistry, Federal University of Sao Carlos, 13565-905 São Carlos, SP, Brazil

Mayara M. Teixeira – CDMF Department of Chemistry, Federal University of Sao Carlos, 13565-905 São Carlos, SP, Brazil; orcid.org/0000-0001-9038-0024

Letícia G. da Trindade − Department of Chemistry, Sao Paulo State University, 17033-360 Bauru, SP, Brazil

Natalia Jacomaci − Chemistry Institute, Sao Paulo State University, 14800-060 Araraquara, SP, Brazil

Andre Perrin − University of Rennes 1, F-35042 Rennes-Cedex, France

Christiane Perrin − University of Rennes 1, F-35042 Rennes Cedex, France

Jose M. Aquino − Department of Chemistry, Federal University of São Carlos, 13565-905 São Carlos, SP, Brazil

Juan Andreś − Department of Analytical and Physical Chemistry, University Jaume I, 12071 Castellon, Spain; orcid.org/0000-0003-0232-3957

ABSTRACT

Bacterial and organic pollutants are major problems with potential adverse impacts on human health and the environment. A promising strategy to alleviate these impacts consists in designing innovative photocatalysts with a wider spectrum of application. In this paper, we report the improved photocatalytic and antibacterial activities of chemically precipitated Ag_3PO_4 microcrystals by the incorporation of W at doping levels 0.5, 1, and 2 mol %. The presence of W directly influences the crystallization of Ag_3PO_4, affecting the morphology, particle size, and surface area of the microcrystals. Also, the characterization via experimental and theoretical approaches evidenced a high density of disordered [AgO_4], [PO_4], and [WO_4] structural clusters due to the substitution of P^{5+} by W^{6+} into the Ag_3PO_4 lattice. This leads to new defect-related energy states, which decreases the band gap energy of the materials (from 2.27 to 2.04 eV) and delays the recombination of e′−h• pairs, leading to an enhanced degradation process. As a result of such behaviors, W-doped Ag_3PO_4 (Ag_3PO_4:W) is a better visible-light photocatalyst than Ag_3PO_4, demonstrated here by the photodegradation of potential environmental pollutants. The degradation of rhodamine B dye was 100% in 4 min for Ag_3PO_4:W 1%, and for Ag_3PO_4, the obtained result was 90% of degradation in 15 min of reaction. Ag_3PO_4:W 1% allowed the total degradation of cephalexin antibiotic in only 4 min, whereas pure Ag_3PO_4 took 20 min to achieve the same result. For the degradation of imidacloprid insecticide, Ag_3PO_4:W 1% allowed 90% of degradation, whereas Ag_3PO_4 allowed 40%, both in 20 min of reaction. Moreover, the presence of W-dopant results in a 16-fold improvement of bactericidal performance against methicillin-resistant Staphylococcus aureus. The outstanding results using the Ag_3PO_4:W material demonstrated its potential multifunctionality for the control of organic pollutants and bacteria in environmental applications.

INTRODUCTION

In the past years, great efforts have been devoted to the search and development of new environmentally friendly photocatalysts for the control of pollutants and water purification as a way to solve great problems associated with the increasing pollution at the surface of the Earth.[1,2] Since Fujishima and Honda demonstrated in 1972 that titanium dioxide (TiO2) could be used as a photoanode to split water excited by ultraviolet light, TiO_2-based catalysts appeared as the most promising approach to solve the global energy crisis and environmental problems due to their low cost and high stability.[3,4] However, the development of such materials is limited because TiO^2 can only be activated under ultraviolet light, which is

a small fraction (around 5%) of solar light, making it more difficult to harvest the remaining solar energy[5,6] and obtain a fast recombination rate of photoinduced electron−hole (e′−h•) pairs.

The limitation of the visible-light harvesting capacity of TiO_2 has motivated researchers to design new single-phase photocatalyst materials with superior visible-light photoactivity.[7] Silver orthophosphate (Ag_3PO_4), a traditional Ag-based semiconductor, is a potential candidate because of its appropriate band gap energy (2.36 eV), nontoxicity, and high photocatalytic activity for the degradation of organic pollutants under visible-light irradiation. The delocalized π* antibonding states formed on the conduction band (CB) can facilitate the separation of charge carriers. Moreover, the inductive effect of PO_4^{3-} anions further promotes the separation of charge carriers.[8] Although Ag_3PO_4 has been found to exhibit a higher photocatalytic activity in the degradation of organic dyes than TiO_2, [9−12] this material can also be considered a promising antibacterial agent for environmental remediation.[13−16] Further technological breakthroughs have been presented combining Ag_3PO_4 and ceftazidime for sterilization and residue removal[17] as well as Ag_3PO_4 and lidocaine to prevent infections.[18] However, the practical application of Ag_3PO_4 is restricted by the photocorrosion resulting from its poor photostability and rapid recombination of photogenerated e′−h• pairs.[19,20]

Consequently, it was necessary to overcome those drawbacks by developing modified Ag_3PO_4 materials to obtain optimized photocatalytic activity and stability.[21] As recently discussed and summarized by Li *et al*.,[22] the progress in the field includes the control of the Ag_3PO_4 exposed facets, incorporation of dopants in the Ag_3PO_4 crystalline lattice, coupling Ag_3PO_4 with metal nanoparticles, and the construction of heterostructured composites. In particular, the use of cations (Bi^{3+}, Ba^{2+}, Ni^{2+}, and Mn^{2+}) [23−26] and anions (SO_4^{2-} and CO_3^{2-})[27,28] as dopants may not only retard charge pair recombination but also enable enhanced visible-light absorption by providing defect states in the band-gap region to improve the photocatalytic activity.[29]

Our group was strongly involved in the theoretical and experimental studies on the structural, optical, and photocatalytic properties of pure and doped Ag_3PO_4.[30−32] Very recently, we reported a new Mo-doped silver orthophosphate (Ag_3PO_4:Mo) material with enhanced photocatalytic activity.[33] This work points out that Mo acts as a dopant, provoking the appearance of defects in the Ag_3PO_4 structure, which significantly improves its photocatalytic performance (100% rhodamine B (RhB) degradation within 5 min). The results were reinforced by the findings of Hussien *et al*.,[34] who observed 98% of methylene blue degradation within 5 min. Considering previous successful research studies, our present aim was to obtain W-doped Ag_3PO_4 (Ag_3PO_4:W) for wider environmental applications. Until now,

little is known about this doping process or its consequences on Ag_3PO_4 final properties and only Ag_3PO_4/WO_3 composites were prepared.[35–37] In this sense, it is expected that the the W^{6+} dopant replaces P^{5+} cations in the Ag_3PO_4 lattice, possibly generating different types of structural and electronic defects and modifying the intermediate energy levels in the band-gap region, which are essential to improve the performance of Ag_3PO_4.

Based on the above considerations, a detailed experimental work via structural, morphological, and compositional characterizations of Ag_3PO_4:W microcrystals was performed. The obtained data was complemented by first-principles calculations. The degradation of organic pollutants including RhB, the antibiotic cephalexin (CFX), and the insecticide imidacloprid (IMC) by Ag_3PO_4:W samples was investigated. We also studied the antibacterial activity of the materials by testing them against methicillin-resistant Staphylococcus aureus (MRSA).

RESULTS AND DISCUSSION

X-ray Diffraction (XRD) and Rietveld Refinement. First crystallographic studies showed that Ag_3PO_4 crystallizes in a cubic structure ($P\bar{4}3n$ space group) based on a body-centered cubic stacking of an isolated regular [PO_4] tetrahedral cluster with P−O bond distances of 1.548 Å. Each Ag^+ cation is located at a fully occupied oxygen site of −4 symmetry.[38,39] Further refinements showed that the position of the Ag^+ cation was in fact split from the 12h site of 2-fold symmetry with half occupancy.[40,41] Consequently, the [AgO_4] tetrahedral cluster was distorted with two different Ag−O distances, 2.357 Å × 2 and 2.404 Å × 2.42.

Powder XRD patterns of pure Ag_3PO_4 and Ag_3PO_4:W (0.5− 2%) are displayed in Figure 1, and their respective Rietveld refinements are illustrated in Figure S1. The patterns are clearly in full agreement with the data relative to Ag_3PO_4 with a cubic structure, as reported in the Inorganic Crystal Structure Database (ICSD) no. 1400039 and no. 1530.40 No impurities such as α-Ag_2WO_4 were found in the samples. This contrasts with our previous results obtained for the doping of Ag_3PO_4 with Mo,[33] in which a well-crystallized secondary phase related to the presence of β-Ag_2MoO_4 was clearly detected above the limit of 2% Mo doping level. No diffraction peaks of expected structural phases related to W were observed, indicating the incorporation of the W cation into the Ag_3PO_4 structure as a doping element.

Table S1 gathers the crystal data from Rietveld refinements for our samples of pure Ag_3PO_4 and Ag_3PO_4:W with 0.5, 1, and 2% W. It can be seen that the lattice constant and

volume slightly increase from 0 to 1%, while an opposite behavior occurs when the W concentration increases to 2%. The overall difference in lattice constants and volume is almost negligible. Under such conditions, it is not possible to accurately determine the doping limit by simply examining the XRD powder patterns.

From the results of Rietveld refinements for the pure Ag3PO4 sample, we constructed theoretical models, as illustrated in Figure 2a,b. The optimized calculations lead to a structure for pure Ag_3PO_4 (Figure 2a) composed of [PO_4] and [AgO_4] clusters, with [PO_4] clusters forming a tetrahedral arrangement with equal P−O bond length (1.5642 Å) and O− P−O angles (109.47°) and [AgO4] clusters presenting two values of O−Ag−O angles (149.87 and 93.87°) with equal Ag−O bond length (2.4306 Å). The result concerning the length of Ag−O bonds goes against that observed in the literature, where two different bond distances were found.[42] This is because the theoretical optimized structure is ideal and perfect in vacuum, without the presence of defects.

The W doping into the Ag_3PO_4 structure induced structural distortions in the crystal lattice and coordination parameters of clusters, as shown in Figure 2b, which can be seen as changes in bond lengths and angles of the [PO_4] and [AgO_4] clusters. Specifically, the W doping process had been shown to induce different average bond lengths for all of the clusters composing the Ag_3PO_4 structure. It was also possible to observe larger P− O and Ag−O bond lengths in the [PO_4] and [AgO_4] clusters, respectively, compared to the pure sample. The resulting cluster of the doping process, the tetrahedral [WO_4] cluster, also presented a distorted nature (distinct average bond lengths and angles) and possessed a longer bond length than the [PO_4] cluster of the pure sample. These behaviors lead to a range of average values and an increase in the local structure disorder, which can profoundly affect the final properties of the studied materials.

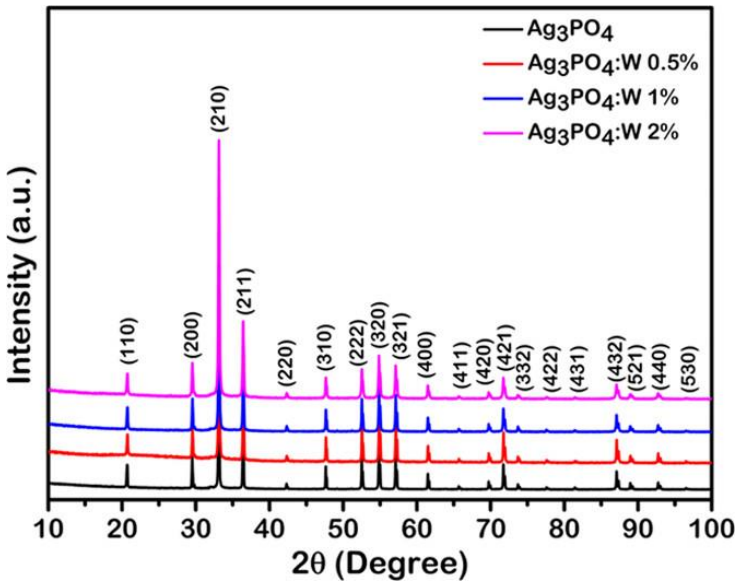

Figure 1. XRD patterns of Ag_3PO_4, Ag_3PO_4:W 0.5%, Ag_3PO_4:W 1%, and Ag_3PO_4:W 2% samples.

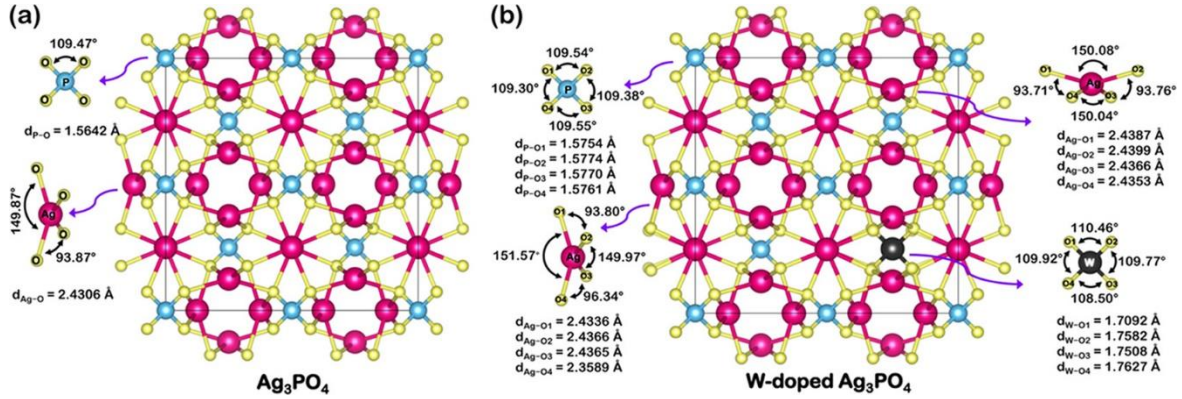

Figure 2. Schematic representation of the 2 × 2 × 2 supercell periodic models built for (a) pure Ag_3PO_4 and (b) Ag_3PO_4:W.

Micro-Raman Spectroscopy. Figure 3a shows the Raman spectra obtained for pure Ag_3PO_4 and Ag_3PO_4:W 0.5, 1, and 2% samples. The spectrum of the pure Ag_3PO_4 is in good agreement with the data previously reported by our research group.[31,33] Eighteen Raman-active modes were expected, but only a few of them were experimentally observed due to an overlapping and/or weak relative intensity. The 1000 cm^{-1} (weak) and 911 cm^{-1} (strong) bands are attributed to T_2 asymmetric and A_1 symmetric stretching modes of the [PO_4] tetrahedron, respectively. A weak scattering band was observed near 701 cm^{-1}, related to a symmetric stretching of the [PO_4] tetrahedron. Based on our previous results, it is not assigned to any first-order normal mode of the Ag_3PO_4 structure and thus could originate from a combination mode, implying the 250 and 458 cm^{-1} wave numbers (for T_2 and A_1, respectively), for instance, in their

calculated spectrum. The T_2 band observed at approximately 549 cm^{-1} is attributed to the bending mode of the [PO_4] tetrahedron, as well the expected modes located at approximately 400 (E) and 220 cm^{-1} (T_2), the last two being not observable due to their weak intensity. The band near 100 cm^{-1} can be associated with translation and/or rotational modes of the T_2 symmetry. All observed Raman bands for all samples are related to Ag_3PO_4 with no secondary phase, indicating the effectiveness of W doping into the Ag_3PO_4 structure.

As it can be seen in Figure 3a, the samples of pure Ag_3PO_4 and Ag_3PO_4:W doped up to 1% presented Raman scattering bands, whereas an increase of W dopant to 2% led to an absence of almost all observed modes for Ag_3PO_4, including the most intense one (A_1) at approximately 911 cm^{-1}. The only observed mode for this sample can be related to translational and/or rotational modes of the structure, while the vibrational modes linked to [PO_4] clusters were absent in the observed spectrum. This band absence is associated with a relative excessive amount of dopant, i.e., the solubility limit of the W dopant in the Ag_3PO_4 structure, which causes a symmetry breaking of the local structure as a result of the high structural disorder density in the composing clusters. This symmetry breaking provokes a break of degrees of freedom, resulting in the absence of [PO_4] clusters subjected to Raman scattering. The point of solubility limit was not observed in XRD patterns due to some technique conditions that were able to detect the structural order at a long range, i.e., the unit cell periodicity. The phase transformation of a dopant into a secondary phase initiates from a short-range structural ordering, which includes bond breaking for later structural rearrangement of the composing clusters. The point of structural changes for a possible rearrangement in the secondary phase was observed for the Ag_3PO_4:W 2% sample. Therefore, as the main goal of this work was to study the W doping effects on the structural, optical, photocatalytic, and antibacterial properties of Ag_3PO_4, all of the other characterization techniques were only employed for pure Ag_3PO_4 and Ag_3PO_4:W 0.5 and 1% samples, since the solubility limit was reached in the Ag_3PO_4:W 2% sample.

It can be observed in Figure 3a that the increase of W dopant concentration caused an increase in the T_2 band intensity located at approximately 1000 cm^{-1}, besides the emergence of two other bands located at approximately 549 cm^{-1} (T_2) and 701 cm^{-1}, which were not observed for the pure Ag_3PO_4 sample. The introduction of W dopant into the crystal lattice provokes local structural changes due to its difference in electron density in comparison with the host P ions in [PO_4] clusters. This difference leads to changes in bond angles and lengths of the W-modified cluster and structural changes in the adjacent clusters (Figure 2b). These structural variations cause a polarization of the clusters, capable of affecting their

electron densities. The Raman scattering arises from polarizability of the structure that allows the light scattering; hence, the higher the polarizability, the higher the Raman scattering. A similar behavior was previously reported for Mo-doped Ag_3PO_4 samples, which was considered as the signature of a local disorder.[33] Therefore, the W doping into the Ag_3PO_4 lattice leads to structural distortions that induce cluster polarization, resulting in a higher polarizability and consequently the appearance of two Raman bands.

A remarkable broadening of the most intense Raman band (A_1 mode, at approximately 911 cm^{-1}) was observed with the increase in the W doping concentration compared to pure Ag_3PO_4. As already mentioned in the XRD section, the theoretical calculations indicated that the incorporation of W into the Ag_3PO_4 structure induces four different average bond lengths for the [PO_4] cluster, in contrast to the pure Ag_3PO_4, which presented only one bond length for the same cluster. Since the A_1 Raman mode observed in the spectra is related to the symmetric stretching of O−P−O bonds, its average bond length directly influences the frequency of the vibrational mode and consequently the Raman shift value. For a given vibrational mode, there is a specific range of frequency allowed for the structure. Therefore, the greater the range of frequencies of a vibrational mode, the greater the bandwidth of the respective Raman shift band due to several allowed frequencies scattering the incident light. Therefore, the observed broadening of the most intense Raman shift band as a function of W doping concentration corroborates the theoretical calculation results, since the W doping provokes a range of bond lengths for [PO_4] clusters.

Furthermore, a shift in the value of the A_1 Raman band was observed with an increase in the W doping concentration compared to pure Ag_3PO_4. As can be seen in Figure 3b, such an increase led to a displacement of the Raman band to lower frequency values, which were 911.4, 909.9, and 908.7 cm^{-1} for pure Ag_3PO_4, Ag_3PO_4:W 0.5%, and Ag_3PO_4:W 1% samples, respectively. Hereupon, the displacements were 1.5 cm^{-1} from pure Ag_3PO_4 to 0.5%W and 1.2 cm^{-1} from the latter to 1%W samples. Based on Badger's rule improved by Herschbach and Laurie, the bond length and vibrational frequency of a stretching mode has an inversely linear correlation, i.e., the longer the bond length, the lower the vibrational frequency.[43–45] These results were clearly observed in the experimental Raman spectra of the samples, indicating the introduction of W as a substitutional dopant in the Ag_3PO_4 structure. According to our theoretical calculations previously described in the XRD section, the introduction of W into the Ag_3PO_4 structure resulted in longer bond lengths of [PO_4] clusters, which corroborates the observed displacement of the A_1 Raman band to lower frequencies. Therefore, these

experimental observations and the theoretical calculations support the introduction of W into Ag_3PO_4 as a substitutional dopant.

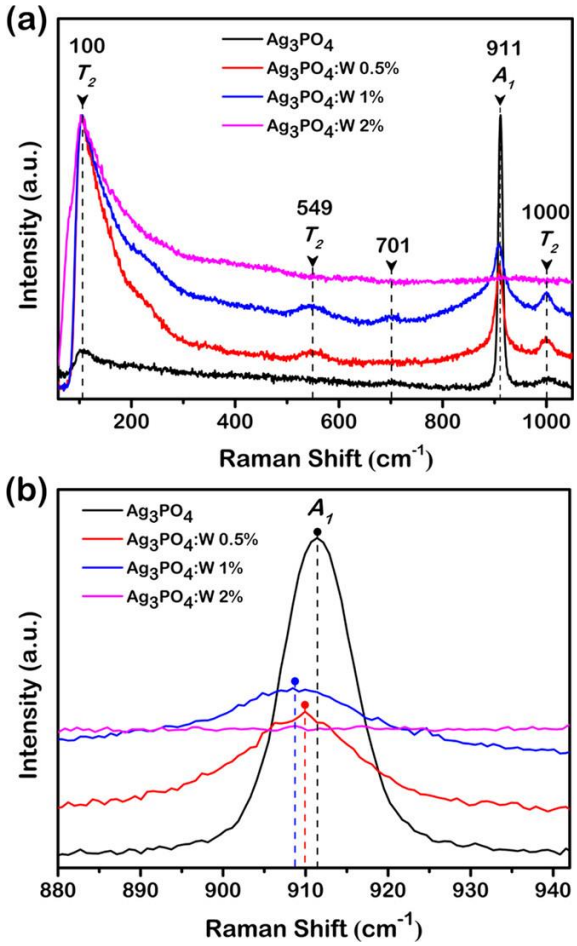

Figure 3. (a) Raman spectra and (b) A1 Raman mode of Ag_3PO_4, Ag_3PO_4:W 0.5%, Ag_3PO_4:W 1%, and Ag_3PO_4:W 2%

X-ray Photoelectron Spectroscopy (XPS) Analysis. This technique was used to identify the surface composition and valence states present in the Ag_3PO_4, Ag_3PO_4:W 0.5 and 1% samples. The survey spectra shown in Figure 4a indicated the presence of sole main peaks associated with the elements Ag, P, W, O, and C (adsorbed and/or from the XPS instrument). The elemental surface quantification (Table 1) confirms the presence of W in both Ag3PO4:W 0.5 and 1% samples at the doping levels. The Ag/P atomic ratio gradually increases with the introduction of W, which can be related to the substitution process of P^{5+} by W^{6+}. Moreover, the samples presented a Ag/P ratio lower than the expected value of 3 for the Ag_3PO_4 structure. Since no secondary phases were identified in all of these samples, this could imply distinct composition comparing the bulk and surface of the particles. Other adsorbed species such as water and CO_2 can also interfere in the quantitative results. A similar trend was observed in our recent publication regarding the Ag3PO4:Mo structure.[33]

Figure 4b shows the high-resolution XPS spectra of W in the 4f region of Ag_3PO_4:W 0.5 and 1% samples. Two main peaks at 37.8 and 35.7 eV can be observed, corresponding to the binding energies of W $4f_{5/2}$ and W $4f_{7/2}$ doublet, respectively, with a spin−orbit separation of 2.1 eV corresponding to the oxidation state W^{6+}. [46] Figure S2 shows the high-resolution XPS spectra of Ag in the 3d region for pure, Ag_3PO_4:W 0.5%, and Ag_3PO_4:W 1% samples. The peaks centered at ∼374 and ∼368 eV are associated with Ag $3d_{3/2}$ and Ag $3d_{5/2}$ doublet, respectively.[47] Then, these peaks were further deconvoluted, revealing two components in each peak; those with the highest intensities centered at 373.9 and 367.9 eV correspond to Ag^+ , while the other less intense peaks at 374.9 and 368.9 eV are attributed to the presence of Ag^0 in our samples.[48] The values calculated for the quantification of Ag^0 at the surface were 18.3, 20.7, and 19.6% for Ag_3PO_4, Ag_3PO_4:W 0.5%, and Ag_3PO_4:W 1%, respectively. The reduction of Ag^+ to Ag^0 can be related to an interaction between the sample and the XPS equipment, as in the case of transmission electron microscopy (TEM) characterization, since the samples are sensitive to the exposure to electromagnetic waves and electron beam.[33] The slightly higher values of Ag^0 in doped samples can be explained by the higher disorder in the Ag_3PO_4 structure induced by W^{6+}, which facilitates the reduction and extrusion processes. Figure S3 shows the high-resolution XPS spectra of O in the Ag_3PO_4 and Ag_3PO_4:W samples fitted in three components at 533.3, 531.9, and 530.5 eV. These components are related to adsorbed water molecules, surface hydroxyl groups, and lattice oxygen in the Ag_3PO_4 structure, respectively.[42,49] Figure S4 shows the highresolution XPS spectra of P, where it is possible to observe two components at 134.2 and 132.8 eV attributable to P $2p_{1/2}$ and P $2p_{3/2}$ doublet, respectively, of P^{5+}.[49]

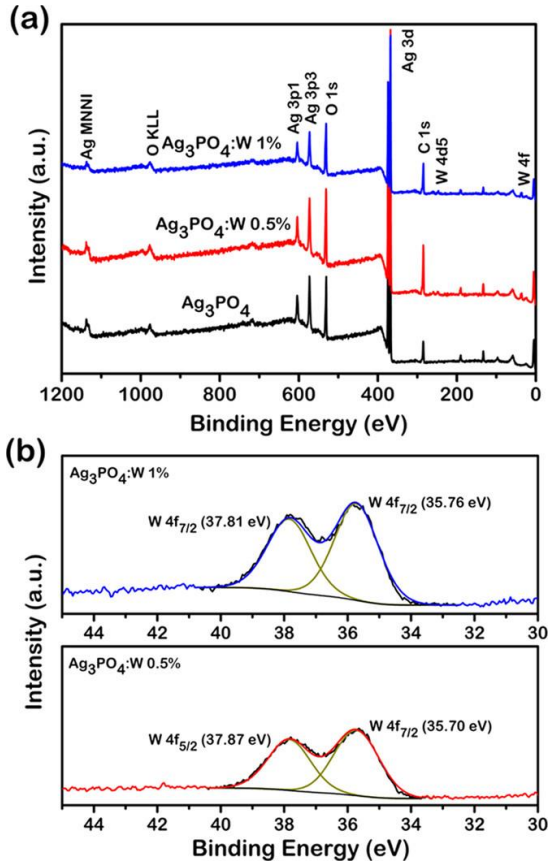

Figure 4. (a) XPS spectra of Ag_3PO_4, Ag_3PO_4:W 0.5%, and Ag_3PO_4:W 1% samples and (b) W 4f high-resolution spectra of Ag_3PO_4:W 0.5% and Ag_3PO_4:W 1%.

Table 1. Elemental surface quantification by XPS of the distinct samples.

Sample	Ag (at%)	P (at%)	W (at%)	O (at%)	Ag/P
Ag_3PO_4	30.25	20.63	–	49.12	1.5
Ag_3PO_4:W 0.5%	29.84	16.58	1.21	52.36	1.7
Ag_3PO_4:W 1.0%	29.30	14.20	1.67	54.83	2.0

Field Emission Scanning Electron Microscopy (FESEM), TEM, and Brunauer−Emmett−Teller (BET) Analyses. The morphologies of Ag_3PO_4 samples are dependent on reagents, additives, procedure, pH, etc. used in the synthesis method.[21] Figure 5a−c displays the FESEM images of pure Ag_3PO_4, Ag_3PO_4:W 0.5%, and Ag_3PO_4:W 1%. The pure Ag_3PO_4 sample is composed of particles with an irregular spherical shape and an average diameter of 440 nm (Table 2 and Figure S5), which is in accordance with Ag_3PO_4 samples prepared under similar conditions.[50] The presence of W dopant affects mainly the shape (insets in Figure 5b,c) and size of the particles, and diameters in the range of 251 and 257 nm are

observed for Ag_3PO_4:W 0.5 and 1% samples, respectively. Such behaviors were also observed for Mo-doped Ag_3PO_4 [33] and can be related to the substitution process of P^{5+} by W^{6+}, which disturbs the crystallization process of the Ag_3PO_4 system. These results were corroborated with the data obtained by the adsorption−desorption isotherms at 77 K/ N_2 (Figure S6) a gradual decrease in particle size and, as a consequence, an increase in specific surface area are observed as the W concentration increases (Table 2).

Figure 5d−l shows the TEM images of the Ag_3PO_4:W 1% sample. The HAADF image in Figure 5d indicates the presence of several particles with distinct sizes, corresponding to Ag_3PO_4:W 1% (yellow dotted circle) and Ag^0 (red dotted circle). To confirm this result, an elementary composition analysis of the sample was conducted by EDS mapping, and the results are exhibited in panels (e)−(h) in Figure 5. The sample presented a homogeneous distribution of Ag, P, W, and O elements, with no clear signs of W dopant segregation, corroborating with the incorporation of W in the Ag_3PO_4 structure. These results also confirm the formation of Ag^0 nanoparticles on the Ag_3PO_4 surface, which is induced by the electron beam of the TEM characterization, as recently demonstrated by our research group.[31] The crystalline features of our sample were analyzed by HR-TEM. Figure 5i shows an image of the border region of a single particle, and Figure 5j presents a magnified view of the corresponding lattice fringes. The interplanar distance at this spot was 0.25 nm, which can be indexed to the (211) plane of Ag_3PO_4 according to the ICSD database no. 14000. Figure 5k displays an HR-TEM image of some small nanoparticles formed on the Ag_3PO_4 surface, while Figure 5l brings a magnified view of these structures. The interplanar distance of 0.20 nm in this last figure can be indexed to the (200) plane of the cubic structure of Ag^0 according to the ICSD database no. 604630.

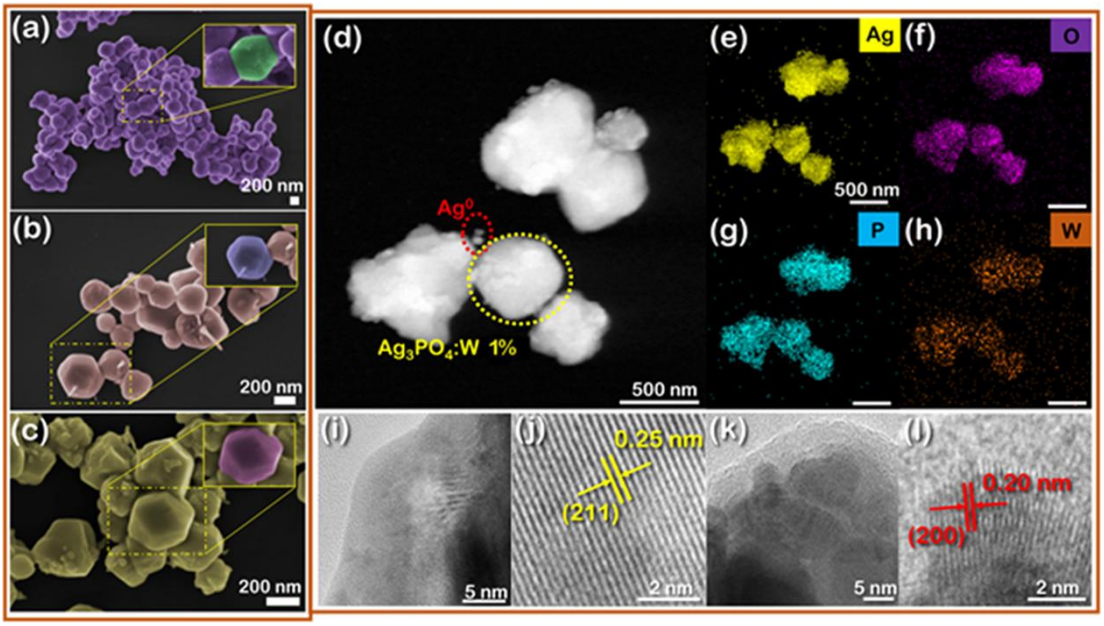

Figure 5. FESEM images of (a) Ag_3PO_4, (b) Ag_3PO_4:W 0.5%, and (c) Ag_3PO_4:W 1%. TEM images of the Ag_3PO_4:W 1% sample: (d) high-angle annular dark-field (HAADF) image showing two regions comprising Ag_3PO_4:W 1% and Ag^0 structures (yellow and red dotted circles, respectively), (e−h) EDS mapping of Ag, O, P, and W elements, (i, j) high-resolution TEM (HR-TEM) images of a border region of the Ag_3PO_4:W 1% crystal, and (k, l) HR-TEM images of Ag^0 nanostructures.

Table 2. Surface area and particle size values obtained by BET and particle size values obtained by FE-SEM for the samples of Ag_3PO_4, Ag_3PO_4:W 0.5%, and Ag_3PO_4:W 1%.

Sample	FE-SEM	BET	
	Particle Size (nm)	Particle Size (nm)	Surface Area (m^2/g)
Ag_3PO_4	442	498	1.89
Ag_3PO_4:W 0.5%	251	207	4.52
Ag_3PO_4:W 1%	257	143	6.57

UV−Visible Diffuse Reflectance Spectroscopy and Electronic Properties. Figure 6a shows the UV−visible spectra of the Ag_3PO_4, Ag_3PO_4:W 0.5%, and Ag_3PO_4:W 1% samples. Considering that Ag_3PO_4 has an indirect band gap,[51] the Kubelka−Munk [52] equation and Tauc method [53] were used to calculate the experimental band-gap energy (E_{gap}) values. The pure Ag_3PO_4 sample presented a E_{gap} value of 2.27 eV, which is consistent with that reported in the literature.[21] It can be noted that with the increase of the doping concentration, there was consequently a decrease in the E_{gap} value from 2.22 eV for the Ag_3PO_4:W 0.5% sample to 2.04 eV for the Ag_3PO_4:W 1% sample. This behavior can be associated with an enhanced structural disorder induced by the W cation in the Ag_3PO_4 lattice, which allows the appearance of new intermediate levels in the forbidden zone between the VB and CB. This result is consistent with that observed for the Ag_3PO_4:Mo structure,33 where the doping by Mo also played key roles in the Ag_3PO_4 electronic structure.

From the calculations, we constructed the band structure for the pure Ag_3PO_4 and Ag_3PO_4:W to analyze the electronic properties of the models. Figure 6b,c reveals that both models caused a direct transition between the Γ-points, with E_{gap} values of 2.52 and 2.44 eV,

respectively. Therefore, the disorder created by the W doping on the Ag_3PO_4 structure provokes a small decrease of the band gap, which is in agreement with our experimental data. To verify how the atomic orbitals are involved and affected by the W doping in the electronic transitions, the density of states (DOS) was analyzed (Figure S7). The VB of pure Ag_3PO_4 is mainly constituted by Ag and O atoms with a small contribution of P atoms with an effective hybridization of the Ag 4d and O 2p orbitals on the top of the VB formed mainly by the ligand orbital. By W doping on the Ag_3PO_4 sample, the top of the VB loses part of the ligand orbital, consequently increasing the antiligand orbital region. This is generally associated with a loss of symmetry in the [AgO_4] clusters. The CB of both models is mostly derived from Ag atoms with a small contribution of P and O atoms as well as W atoms in the Ag_3PO_4:W model. The knowledge of the density of states allows us to explain how the atomic orbitals are involved in the properties of the materials.

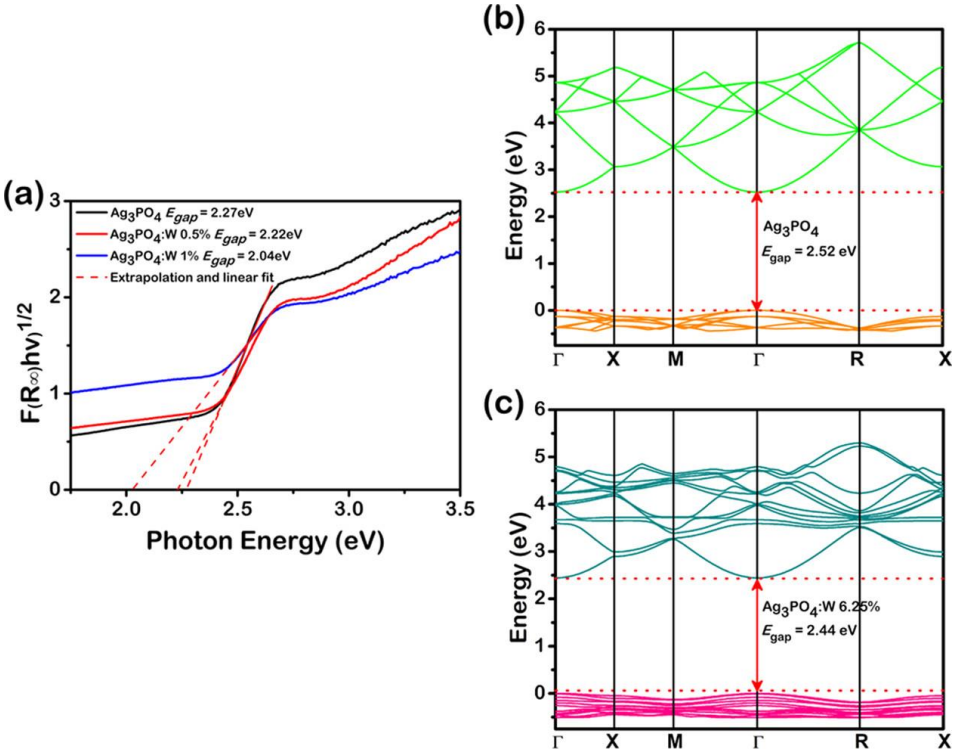

Figure 6. (a) UV−visible absorption spectra and band-gap energies for Ag_3PO_4, Ag_3PO_4:W 0.5%, and Ag_3PO_4:W 1% samples. Calculated band structures of (b) Ag_3PO_4 and (c) Ag_3PO_4:W models.

Photocatalytic Activity of Ag_3PO_4:W Microcrystals against RhB Dye. Photocatalytic tests were performed for the pure Ag_3PO_4 sample and Ag_3PO_4:W 0.5 and 1% samples by the degradation of RhB under visible-light irradiation. Figure 7a−c shows the

UV−visible absorption spectra obtained by collecting aliquots at given times (0, 5, 10, and 15 min) and subsequently measuring their absorbance at 554 nm. Figure 7d shows the variation of RhB concentration (C_N/C_0) as a function of irradiation time, where C_0 and C_N are the equilibrium adsorption concentrations at t0 and at the irradiation time t, respectively. From the control experiment (without the addition of a photocatalyst), the photolysis of RhB upon visible-light irradiation was almost negligible. The doped samples presented higher photocatalytic activity than the pure material, especially the Ag_3PO_4:W 1% sample, allowing a complete degradation of the dye in less than 5 min of irradiation. The kinetics of the photocatalytic degradation can be described using the pseudo-first-order reaction, and the rate constants (k′) for the degradation of RhB with and without the presence of photocatalysts were calculated by the Langmuir−Hinshelwood plot (Figure 7e). As mentioned above, the Ag_3PO_4:W 1% sample revealed a better photocatalytic activity, with a k′ of 4.49×10^{-1} min^{-1} , approximately 3 times higher than that of the pure Ag_3PO_4 sample ($k' = 1.64 \times 10^{-1}$ min^{-1}) and even higher than that of the Ag_3PO_4:W 0.5% sample ($k' = 3.23 \times 10^{-1}$ min^{-1}).

To follow more precisely the degradation rate, another experiment was performed with intervals of 1 min for the Ag_3PO_4:W 1% sample, as shown in Figure 8a, revealing a complete degradation in approximately 4 min of irradiation under visible light. This result confirms that the material proposed has promising photocatalytic properties comparable to other efficient Ag_3PO_4 doped photocatalysts. To study the photocatalytic stability of the doped material with W, cycling tests were performed for the same sample (Figure 8b). It can be seen that the doped sample maintains its stability until the second cycle, but its catalytic activity decreases in the third cycle. It is well reported that Ag_3PO_4 undergoes a photocorrosion process, where the photoexcited electrons cause the reduction of Ag^+ to Ag^0 during the photocatalysis. Ag^0 is formed mainly on the active surfaces of the material, hampering the absorption of light and, thus, decreasing the photocatalytic activity.[54,55] In the Ag_3PO_4:W 1% sample, this mechanism is facilitated since the presence of W dopant causes structural disturbances, generates defects on the particle surface, and consequently changes the surface energy of the microcrystals. These features can reduce the stability of Ag^+ to photocorrosion, as also observed by doping the Ag_3PO_4 structure with Mo.[33] However, even with a loss in photocatalytic activity, the photocatalyst degrades 60% of the dye within 5 min in the third cycle of reuse.

In general, a complete semiconductor photocatalytic cycle involves light harvesting, photogeneration of charge carriers, charge separation and transfer, and surface redox reactions to allow the formation of reactive oxygen species (ROS) that play crucial roles

in photocatalysis.[56,57] Therefore, to understand the photodegradation mechanism of the doped Ag_3PO_4 samples and the higher photocatalytic performance of Ag_3PO_4:W 1%, photocatalytic experiments with radical scavengers were conducted using this sample as a photocatalyst. As shown in Figure 8c, the addition of AO caused the degradation to decrease from almost 100% to less than 20%, relative to the same visible-light irradiation time, showing that $h^{\bullet}$ is the major active species in the photodegradation mechanism. The addition of BQ presented a slight influence on the photodegradation efficiency, and the addition of tertbutyl alcohol (TBA) did not exhibit significant influence. These results indicate that O_2' and OH* species had, respectively, minor and negligible participation in the observed mechanism. At this point, it is important to remark that the use of electron spin resonance would further confirm the nature of the radicals involved in the degradation process.

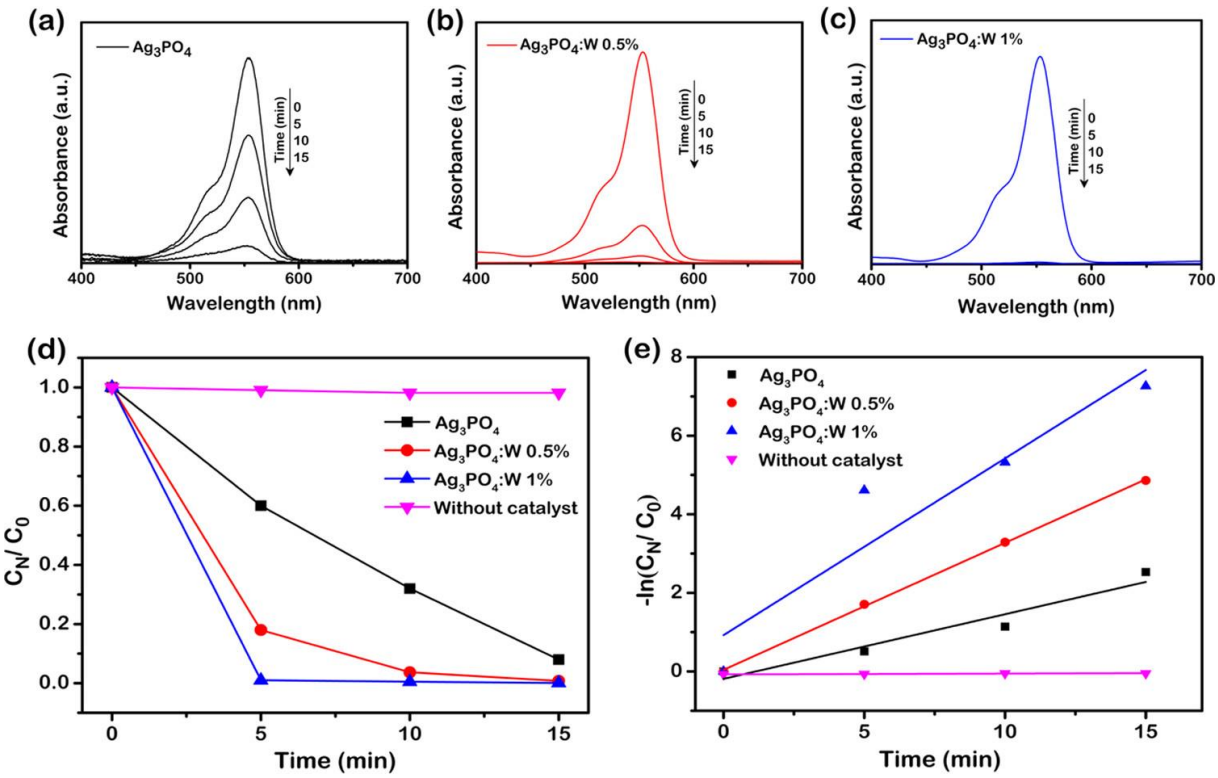

Figure 7. UV−visible absorption spectra of RhB upon photodegradation in the presence of (a) Ag_3PO_4, (b) Ag_3PO_4:W 0.5%, and (c) Ag_3PO_4:W 1%. (d) Photocatalytic degradation of RhB (1.0×10^{-1} mol L^{-1}) in the absence and in the presence of Ag_3PO_4 and Ag_3PO_4 doped with different amounts of W and (e) Langmuir−Hinshelwood plot for the determination of the rate constant.

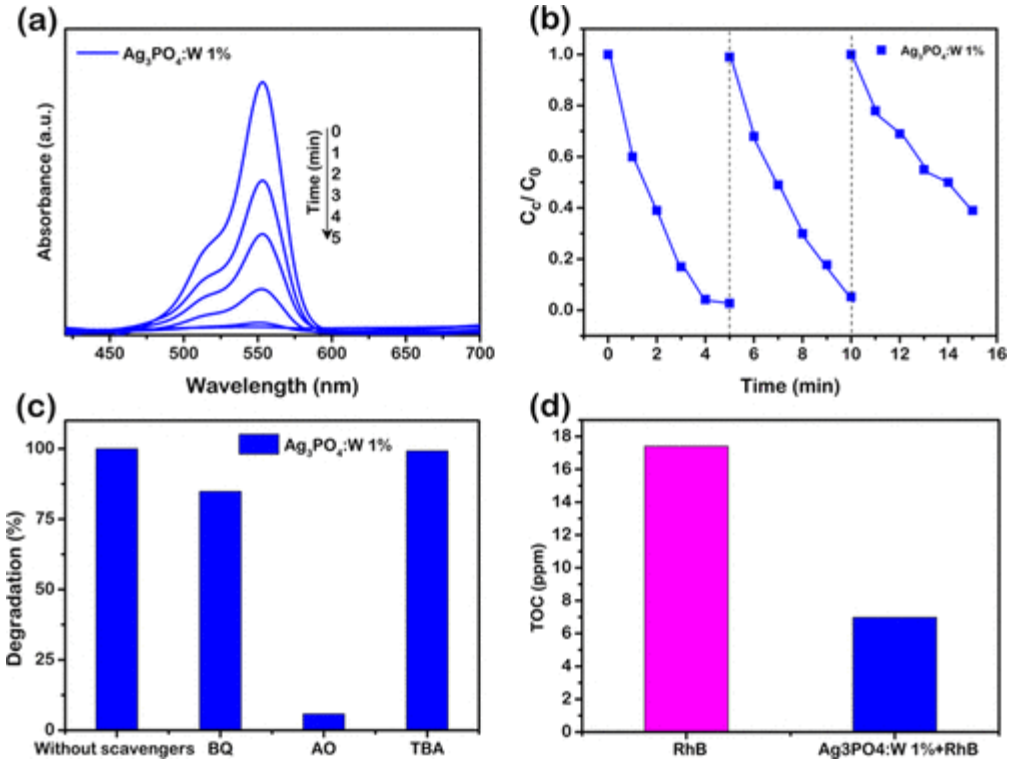

Figure 8. (a) UV−visible absorption spectra of RhB photodegradation in the presence of Ag_3PO_4:W 1% collected in time less than 5 min and (b) run cycles of RhB degradation using Ag_3PO_4:W 1% under visible-light irradiation. (c) Influence of the scavengers on the degradation of RhB in the presence of Ag_3PO_4:W 1% under visible-light irradiation and (d) analysis of total organic carbon (TOC) for degradation of RhB in the presence of Ag_3PO_4:W 1% under 30 min of visible-light irradiation.

To further evaluate the photocatalytic activity of Ag_3PO_4 and Ag_3PO_4:W 1%, the decrease in the total organic carbon (TOC) concentration during the photodegradation processes was also investigated. Because the TOC analyzer has low sensibility, the concentration of contaminant was doubled in these tests (20 mg L^{-1}). Thus, the mass of the catalyst was increased accordingly to 100 mg, and the irradiation time was extended to 30 min. The remaining TOC fraction of the RhB solution can be seen in Figure 8d. As expected for the Ag_3PO_4:W 1% photocatalyst, the TOC removal was much higher than when the pure material was used. In this case, the TOC decreased by 60% after 30 min, indicating that Ag_3PO_4:W 1% could mineralize RhB and its degradation byproducts under visible-light irradiation even in a short time. For the Ag_3PO_4 sample, the degradation percentage was approximately 32%. A similar degradation extent for RhB (~52%) was reported using Ag_3PO_4:Mo 0.5% after 30 min of treatment.[33]

W-doped samples are composed of distorted clusters, which present significant changes in bond lengths and angles with respect to their equilibrium positions (Figure 2b). This symmetry breaking process leads to an electronic reorganization and the spontaneous formation of donor and acceptor levels within the band gap, causing the gradual decrease in the Egap observed for the W-doped Ag_3PO_4 samples (Figure 6a−c). Hence, the higher amount of dopant in the Ag_3PO_4:W 1% sample results in a greater density of defect-related energy states, which can increase the visible-light absorption, more efficiently serve as charge carrier traps to delay $e'-h^{\bullet}$ recombination, and consequently improve the photocatalytic property of the material. In addition, the smaller particle sizes of the Ag_3PO_4:W 1% sample (Table 2) also prevent charge carrier recombination, since there is a decrease in the distance for their migration from the core to the surface of the microcrystals. The higher surface area in comparison to the other samples could also develop an additional role for the best RhB degradation observed by increasing the dye adsorption capability of the photocatalyst.

Photocatalytic Activity of Ag_3PO_4:W against CFX and IMC. Once the photocatalytic activity of materials doped with W, especially the sample Ag_3PO_4:W 1%, showed promising results, even better than those seen in Mo-doped Ag_3PO_4,[33] it was also investigated whether this property extends to another class of organic contaminants. For this, additional experiments were carried out for the highest active photocatalyst (Ag_3PO_4:W 1%) to test the photodegradation of CFX and IMC insecticide solutions. As can be seen in Figure 9a, a behavior similar to that of RhB was found in the photodegradation of CFX, using the pure and doped material. The total removal of CFX was achieved after 20 min using Ag_3PO_4 against 4 min using the W-doped material. The conversion to CO_2 is also superior for Ag_3PO_4:W 1% (28%) than for pure Ag_3PO_4 (10%), as shown by the mineralization analysis in Figure 9b. On the other hand, the lower efficiency of Ag_3PO_4:W 1% compared to its yield in RhB mineralization (60%) indicates that, for CFX, the degradation of byproducts is more recalcitrant than that of the original molecule. A similar result about the tardive mineralization process of antibiotics was published by Chen *et al.*,[58] in which the photocatalytic mineralization of ciprofloxacin (1 mg L^{-1}) using Gab/ Ag_3PO_4/ hematite under solar light was ∼30% in 30 min.

Figure 9c shows the evolution of the IMC concentration as a function of time of irradiation for the photocatalysts used. In this case, a moderate removal of IMC (∼55%) was achieved after 30 min using the pure Ag_3PO_4 sample, suggesting that the IMC molecule is recalcitrant toward oxidation provoked by the use of this material. Clearly, a significant improvement in the IMC degradation was obtained using Ag_3PO_4:W 1%, where almost 100% removal of insecticide was achieved after 30 min. However, the degradation of IMC did not

result in significant levels of mineralization in the time interval probed but only in accumulation of byproducts in the reaction medium, as shown in Figure 9d. For the pure and 1% doped materials, the degradation was ~14 and ~26%, respectively.

These results evidenced that some of the degradation byproducts are more stable toward the photocatalytic process, as also observed elsewhere.[59,60] Specifically, Katsumata *et al.* found a high level of conversion to CO_2 (83%) in the photocatalytic treatment of bisphenol A (10 mg L^{-1}) using Ag_3PO_4 under visible light after 180 min.[61] This indicates that for the Ag_3PO_4:W 1% sample, the mineralization level obtained for CFX and IMC could be improved by increasing the irradiation time. Hence, it clearly appears that the Ag_3PO_4:W 1% sample has superior photocatalytic properties compared to the pure material and thus could be an interesting option to degrade a wide range of pollutants.

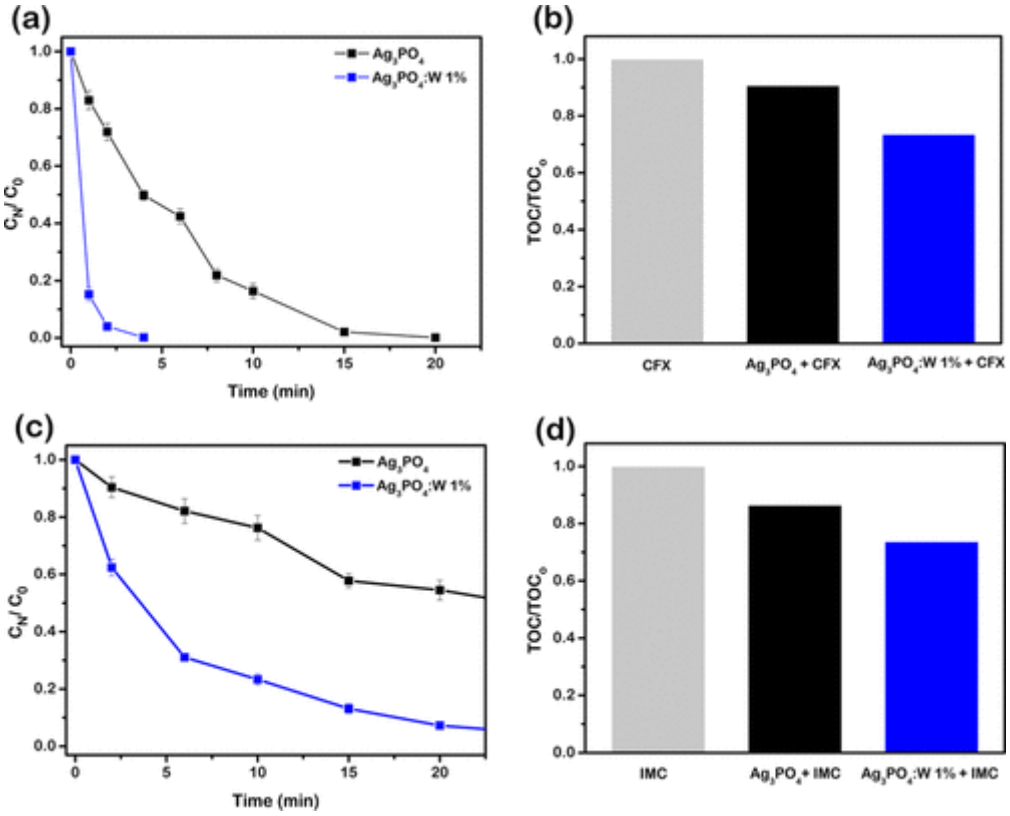

Figure 9. (a) Photocatalytic degradation of CFX in the presence of Ag_3PO_4 and Ag_3PO_4:W 1% in a linear plot and (b) analysis of total organic carbon for degradation of CFX in the presence of Ag_3PO_4 and Ag_3PO_4:W 1% under 30 min of visible-light irradiation. (c) Photocatalytic degradation of IMC in the presence of Ag_3PO_4 and Ag_3PO_4:W 1% in a linear plot and (d) analysis of total organic carbon for degradation of IMC in the presence of Ag_3PO_4 and Ag_3PO_4:W 1% under 30 min of visible-light irradiation.

Antibacterial Activity. Antimicrobial resistance is one of the most difficult issues humanity deals with, and the World Health Organization (WHO) has been emphasizing the urgency of new options of treatments with low resistance development.[62] In this sense, there is a need to develop novel antibacterial agents to combat bacteria, such as Staphylococcus aureus, which has the ability to develop resistance to all classes of clinically available antibiotics and is often detected in both hospital and municipal wastewaters.[63] Although some previous studies successfully demonstrated the antibacterial capacity of compounds such as Ag_3PO_4, [13,15,16] this is the first time that the Ag_3PO_4:W activity is reported against methicillin-resistant S. aureus (MRSA). Antibacterial tests were performed using pure Ag_3PO_4 and W-doped Ag_3PO_4 samples, and the results are displayed in Figure 10. All probed materials showed antimicrobial activity against MRSA, and the minimal inhibitory and minimal bactericidal concentration (MIC/ MBC) values for the Ag_3PO_4, Ag_3PO_4:W 0.5%, and Ag_3PO_4:W 1% samples were 125, 31.25, and 7.81 μg mL^{-1}, respectively. It can be observed that the antibacterial capacity of the material increases as the W concentration increases.

The substitution of P^{5+} by W^{6+} yields a decrease in particle size and a consequent increase in surface area (Table 2), which could be the main cause for the excellent bactericidal activity of the Ag_3PO_4:W 1% sample. It is known that smaller materials have high antimicrobial capacities in comparison with larger materials,[64] and the increase in the surface area of the particles holds the advantage of efficiently binding to microorganisms for enhanced antimicrobial action.[65] Wu *et al*.[13] observed the correlation among particle size, specific surface area, and antibacterial activity in Ag_3PO_4 micro- and nanoparticles. In this case, as the particle size decreased, the specific surface area increased, consequently enhancing the antibacterial activity against Escherichia coli and Bacillus subtilis.

The results obtained through the Rietveld refinement complemented by the theoretical results show that the tetrahedral $[WO_4]$ cluster presented a distorted nature and exhibited longer bond length than the $[PO_4]$ cluster of the pure Ag_3PO_4. The increase of this structural local disorder profoundly alters the properties of the material, leading to an enhanced $e'-h^{\bullet}$ separation, which is directly proportional to the ROS production.66 These species, in turn, are responsible for injuries to the plasmatic membrane of microorganisms and changes in the cytoplasmic region, rendering them inhomogeneous in comparison with healthy microorganisms. ROS is also associated with disintegration of DNA, RNA, and microbial proteins, causing severe cellular injuries, making them unviable.[67] Thus, as Ag_3PO_4:W 1% has

a greater density of defects, the e′−h• separation is facilitated, and it becomes the best and most effective antimicrobial agent.

Based on the photocatalytic and bactericidal results, it can be assumed that the proposed W-doped Ag_3PO_4 microcrystals have the potential to be industrially used as a catalyst for wastewater decontamination from organic pollutants, employing sunlight irradiation for these processes, as well as to act as a bactericidal agent for the inactivation of resistant bacteria in wastewater or in product packaging. Both properties were proven to be superior to those of the pure material. However, although higher RhB degradation is detected in the third cycle of reusing the Ag_3PO_4:W 1% sample in comparison with pure Ag_3PO_4, the recycling efficiency improvement of the W containing microcrystals is still an issue that needs to be addressed to achieve a better stability for this photocatalyst.

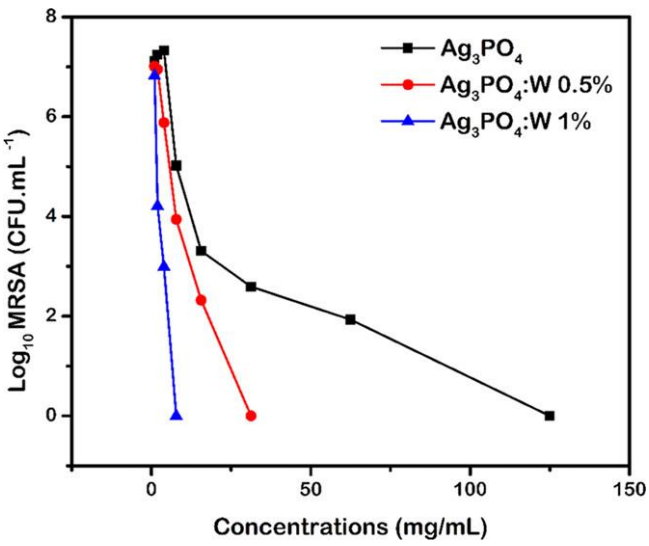

Figure 10. Bacterial growth values (Log_{10}) as a function of the concentrations (mg mL^{-1}) of Ag_3PO_4 and Ag_3PO_4:W.

CONCLUSIONS

In summary, new single-phased photocatalysts based on Ag_3PO_4 doped with W were easily obtained by the chemical precipitation method without any evidence of W dopant segregation up to 1% of doping. The experimental results and first-principles calculations revealed that the structural disorder and morphological changes caused by W incorporation in the Ag_3PO_4 crystalline lattice are closely related to the final properties of the materials, and the Ag_3PO_4:W 1% sample stood out with respect to its photocatalytic and bactericidal activities. In this sense, the Ag_3PO_4:W 1% sample exhibited a remarkable enhancement of photodegradation of RhB with a total discoloration of the dye in only 4 min (90% in 15 min for pure Ag_3PO_4)

and a TOC decrease of 60% in 30 min (32% in 30 min for pure Ag_3PO_4). Tests for the photodegradation of antibiotic CFX and insecticide IMC also revealed that Ag_3PO_4:W 1% microcrystals are more interesting to degrade a wide range of pollutants than pure Ag_3PO_4. The bactericidal activity of the materials was investigated against MRSA. The MIC/MBC value for Ag_3PO_4:W 1% was 7.81 μg mL^{-1} , which is significantly lower in comparison to that of pure A Ag_3PO_4 (125 μg mL^{-1}), evidencing the highest potential for the Wdoped material to be used as an antimicrobial agent. The present results provide a deep understanding of the photocatalytic and antibacterial activities of Ag_3PO_4:W, standing as a potential material for applications in environmental remediation.

EXPERIMENTAL SECTION

Synthesis of Pure Ag_3PO_4 and Ag_3PO_4:W Microcrystals. Pure Ag_3PO_4 and Ag_3PO_4:W samples were synthesized by the CP method in aqueous medium at room temperature. The salts used in the preparation of the materials were $(NH_4)_2HPO_4$ (0.001 M) (98.6%, J.T. Baker), $AgNO_3$ (0.003 M) (99.8%, Vetec), and $Na_2WO_4{\cdot}2H_2O$ (99.5%, SigmaAldrich). Two solutions were prepared: the first one was $(NH_4)_2HPO_4$ diluted in 50 mL of deionized water at 30 °C under agitation to dissolve the salt and the second one was composed of $AgNO_3$ diluted in 50 mL of deionized water at 30 °C under stirring. The dopant was added in the first solution after complete dissolution of the $(NH_4)_2HPO_4$ salt. The salt contents used were 0.000, 0.005, 0.01, and 0.02 moles. The syntheses were conducted by first adding the second solution to the first one and then keeping this mixture under stirring for 10 min to obtain yellow precipitates. The obtained materials were centrifuged several times with deionized water to remove soluble species and oven-dried at 60 °C for 24 h. For practical reasons, these samples were named pure Ag_3PO_4 and Ag_3PO_4:W 0.5, 1, and 2%.

Characterization Techniques. The obtained materials were characterized by XRD using a D/Max-2500PC diffractometer (Rigaku, Japan) with Cu Kα1 radiation (λ = 1.54056 Å) in the 2θ range of 10−100°, a scanning speed of 1° min−1 , and a step size of 0.02°. For the Rietveld refinements, we used the general structural analysis system (GSAS) software package with graphic interface EXPGUI. The theoretical diffraction pattern was obtained from ICSD no. 14000, which is based on the body-centered cubic structure with the $P\bar{4}3n$ space group. For the micro-Raman spectra, an iHR550 spectrometer (Horiba Jobin-Yvon, Japan) was used coupled to a CCD detector and an argon ion laser (Melles Griot) operating at 514.5 nm with a maximum power of 200 mW. The spectra were measured in the range of 50−1100 cm−1 . Measurements of X-ray photoelectron spectroscopy (XPS) were performed on a Scienta

Omicron ESCA+ spectrometer (Germany) using monochromatic Al Kα (1486.7 eV). The maximum deconvolution was performed using a line of 70% Gaussian and 30% Lorentzian with a baseline of the nonlinear (Shirley-type) sigmoid. For calibration of the binding energy of the elements, the peak C 1s at 248.8 eV was used as reference. Transmission electron microscopy (TEM) and high-resolution TEM (HR-TEM) were performed using an FEI Tecnai G2F20 microscope (Netherlands) operating at 200 kV. A high-angle annular dark-field (HAADF) image and elemental mapping by energy-dispersive X-ray spectroscopy (EDS) were recorded in the scanning TEM (STEM) mode. The morphologies of the samples were characterized by field emission gun scanning electron microscopy (FESEM) in an FEI instrument (Inspection Model F50) operating at 10 kV. The BET surface area (SBET) and particle sizes of the samples were studied using N2 adsorption and desorption isotherms measured at 77 K on a Micrometrics ASAP 2420 A surface area and porosimetry analyzer. Prior to the N_2 adsorption measurement, the samples were degassed at 200 °C under vacuum for 4 h. The SBET of the samples was calculated using the Brunauer−Emmett− Teller (BET) method in the relative pressure (P/P_0) range of 0.05−0.16. To obtain ultraviolet−visible (UV−visible) absorption spectra, a Varian Cary 5G spectrophotometer was used in diffuse reflection mode.

Computational Methods. First-principles calculations for the Ag_3PO_4 and Ag_3PO_4:W structures were performed using the CRYSTAL14 software package.[68,69] Moreover, density functional theory (DFT) calculations at the B3LYP hybrid functional level were made.[70,71] The thresholds controlling the accuracy of Coulomb's law calculations and the exchange integrals were set to 10^{-8} , 10^{-8} , 10^{-8} , 10^{-8} , and 10^{-14}, and the percentage of Fock/Kohn−Sham matrix mixing was set to [40]. The diagonalization of the Fock matrix was performed using an adequate number of k-point grids in the reciprocal space. The basis sets obtained from the CRYSTAL website[72] for the atomic centers of Ag, P, O, and W were described by PS311d31G, 85-21d1G, 6-31d1, and PS-311(d31)G, respectively, where PS stands for Hay and Wadt's nonrelativistic small-core pseudopotential.[73] The lattice parameters and internal atomic coordinates of the bulk Ag_3PO_4 were fully optimized until all force components were less than 10−6 eV Å−2 . From these optimized parameters, two 2 × 2 × 2 supercell periodic models were built for pure Ag_3PO_4 and Ag_3PO_4:W samples to accurately describe the structural and electronic properties derived from the experimental synthesis. In the supercell model, there were 16 Ag_3PO_4 units (Z = 16). To build the Ag_3PO_4:W model, one P cation was replaced by one W cation. Therefore, it was necessary to create a load balance to ensure the electroneutrality of the system by generating a Ag^+ vacancy near the P atom replaced

by the W atom. Our Ag_3PO_4:W model contains 6.25 mol % W in the structure. Unfortunately, to obtain lower percentages of W doping, a larger supercell model would be required, and the computational cost is prohibitive. The same theoretical strategy was used to construct an Ag_3PO_4:Mo model, as recently reported.33 The band structure and density-of-states (DOS) models were constructed along the appropriate high-symmetry directions of the corresponding irreducible Brillouin zone implemented in the CRYSTAL program.

Photocatalytic Measurements. The photocatalytic activity of both pure and doped samples was tested for degradation of RhB (95%, Aldrich) under visible-light irradiation. For the tests, 50 mg of each photocatalyst, Ag_3PO_4 and Ag_3PO_4:W, was added in a beaker containing a solution of RhB (50 mL, 10 mg L^{-1}). This solution was placed in an ultrasonic bath (Branson, model 1510; frequency 42 kHz) for 30 min and then stirred for another 30 min for a better absorption−adsorption equilibrium process, always keeping the solutions protected from light. After this stage, an aliquot at time 0 was collected, the solution was placed under irradiation of six lamps (Philips TL-D, 15 W), and the system was kept under stirring at a controlled temperature of 20 °C. Subsequent aliquots were collected at determined intervals and centrifuged to remove the photocatalyst powder. Dye degradation was monitored by measuring the peak absorbance of RhB (λmax = 554 nm) using a UV−visible spectrophotometer (V-660, JASCO). A control experiment was carried out under the same conditions but without photocatalysts.

To understand the roles of reactive oxygen species (ROS) in the photocatalytic process, experiments on scavengers were performed by adding 0.1 M tert-butyl alcohol (TBA) (Alfa Aesar), 1×10^{-3} M ammonium oxalate (AO) (Alfa Aesar), and 1×10^{-3} M benzoquinone (BQ) (Alfa Aesar) as scavengers of the hydroxyl radical (OH*), hole ($h^{\bullet}$), and superoxide radical (O_2'), respectively. In addition, we studied the efficiency of this novel material regarding the oxidation of another class of contaminant, i.e., the degradation process of synthetic solutions (10 mg L^{-1}) of CFX (95%, Vita Nova) and IMC (commercial solution, AdamaBrasil), which are types of antibiotic and insecticide, respectively. The CFX and IMC concentrations were monitored by high-performance liquid chromatography (HPLC) using Shimadzu LC-20A equipment and a reversedphase C18 column (150 mm × 4.6 mm, 5 μm particle size from Phenomenex) as the stationary phase. For CFX determination, a mixture of 10 mmol L^{-1} KH_2PO_4 (eluent A) buffer solution (pH 3, adjusted with phosphoric acid) and methanol (eluent B) was used as the mobile phase at 1.0 mL min^{-1} , with the following gradient elution protocol: from 10% (V/V) eluent B to 90% in 10 min and then returning to 10% in 3 min. CFX was

detected at 262 nm, and the injection volume was 15 μL. A mixture of 0.1% formic acid (eluent A) and methanol (eluent B) at 1.0 mL min^{-1} in gradient mode was used as the mobile phase for the IMC determination: from 20% (V/V) eluent B to 90% in 8 min and then returning to 20% in 3 min. IMC was detected at 270 nm, and the injection volume was 25 μL. Finally, the mineralization (i.e., conversion to CO_2) extent was also measured by analysis of the total organic carbon (TOC) concentration (TOC analyzer, GE Sievers Innovox) using 6 mol L^{-1} H_3PO_4 (a.r., Mallinckrodt) and 30% (m/m) $Na_2S_2O_8$ (99%, Sigma-Aldrich) as acidifier and oxidant reagents, respectively.

Antibacterial Measurements. In this study, the antibacterial activity of Ag_3PO_4 and Ag_3PO_4:W was investigated against MRSA from the American Type Culture Collection (ATCC 33591). Antibacterial activity probes were performed according to the protocol previously described.[74] Briefly, MRSA cells were cultured from the frozen stock onto Mueller−Hinton agar plates and incubated at 37 °C for 24 h. Colonies of fresh cells were transferred to tryptic soy broth (TSB) and incubated until reaching the mid-log stage of microbial growth. The minimal inhibitory and minimal bactericidal concentration (MIC/MBC) susceptibility tests were performed using the broth microdilution method of the Clinical and Laboratory Standards Institute, documents M27- A3 (2008),75 with some modifications. Microbial growth control consisted of bacterial suspension in culture medium without particles, while negative controls consisted of uninoculated culture medium.[76] To ensure data reproducibility, the experiments were performed in triplicate, on three different occasions.

ACKNOWLEDGMENTS

The authors acknowledge financial support of the Brazilian research financing institutions: Fundação de Amparo à Pesquisa do Estado de Sao Paulo (FAPESP, 2013/07296-2, 2017/12594-3, 2019/01732-1, and 2019/13507-2), Coordenaçao de Aperfeiçoamento de Pessoal de Nivel Superior Brasil (CAPES) Finance Code 001 and Conselho Nacional de Desenvolvimento Científico e Tecnológico (CNPq, 142035/2017-3). The authors acknowledge the Research Center on Advanced Materials and Energy for N_2 physisorption analysis. J.A. acknowledges Universitat Jaume I for projects UJI-B2016-25 and UJI-B2019-30 and Ministerio de Ciencia, Innovación y Universidades (Spain), project PGC2018-094417-B-I00 for supporting this research financially. We also acknowledge the Servei Informatica, Universitat Jaume I, for a generous allotment of computer time, with special thanks to A.O. Machado, M.Sc., for critical reading of the manuscript.

REFERENCES

(1) Zhang, S.; Li, B.; Wang, X.; Zhao, G.; Hu, B.; Lu, Z.; Wen, T.; Chen, J.; Wang, X. Recent Developments of Two-dimensional Graphene-based Composites in Visible-light Photocatalysis for Eliminating Persistent Organic Pollutants from Wastewater. Chem. Eng. J. 2020, 390, No. 124642.

(2) Chen, Z.; Zhang, S.; Liu, Y.; Alharbi, N. S.; Rabah, S. O.; Wang, S.; Wang, X. Synthesis and Fabrication of g-C_3N_4-based Materials and Their Application in Elimination of Pollutants. Sci. Total Environ. 2020, 731, No. 139054.

(3) Fujishima, A.; Honda, K. Electrochemical Photolysis of Water at a Semiconductor Electrode. Nat. Mater. 1972, 238, 37−38.

(4) Chen, X.; Zhang, Z.; Chi, L.; Nair, A. K.; Shangguan, W.; Jiang, Z. Recent Advances in Visible-light-driven Photoelectrochemical Water Splitting: Catalyst Nanostructures and Reaction Systems. Nano-Micro Lett. 2016, 8, 1−12.

(5) Li, X.; Li, J.; Bai, J.; Dong, Y.; Li, L.; Zhou, B. The Inhibition Effect of Tert-butyl Alcohol on the TiO_2 Nano Assays Photoelectrocatalytic Degradation of Different Organics and Its Mechanism. Nano-Micro Lett. 2016, 8, 221−231.

(6) Li, X.; Jiang, Y.; Cheng, W.; Li, Y.; Xu, X.; Lin, K. Mesoporous TiO_2/Carbon Beads: One-pot Preparation and their Application in Visible-light-induced Photodegradation. Nano-Micro Lett. 2015, 7, 243−254.

(7) Kim, H. G.; Hwang, D. W.; Lee, J. S. An Undoped, Single-phase Oxide Photocatalyst Working under Visible Light. J. Am. Chem. Soc. 2004, 126, 8912−8913.

(8) Martin, D. J.; Liu, G.; Moniz, S. J.; Bi, Y.; Beale, A. M.; Ye, J.; Tang, J. Efficient Visible Driven Photocatalyst, Silver Phosphate: Performance, Understanding and Perspective. Chem. Soc. Rev. 2015, 44, 7808−7828.

(9) Dong, L.; Wang, P.; Wang, S.; Lei, P.; Wang, Y. A Simple Way for Ag_3PO_4 Tetrahedron and Tetrapod Microcrystals with High Visible-light-responsive Activity. Mater. Lett. 2014, 134, 158−161.

(10) Liang, Q.; Ma, W.; Shi, Y.; Li, Z.; Yang, X. Hierarchical Ag_3PO_4 Porous Microcubes with Enhanced Photocatalytic Properties Synthesized with the Assistance of Trisodium Citrate. CrystEngComm 2012, 14, 2966−2973.

(11) Yi, Z.; Ye, J.; Kikugawa, N.; Kako, T.; Ouyang, S.; StuartWilliams, H.; Yang, H.; Cao, J.; Luo, W.; Li, Z.; Liu, Y.; Withers, R. L. An Orthophosphate Semiconductor with Photooxidation Properties under Visible-light Irradiation. Nat. Mater. 2010, 9, 559−564.

(12) Hsieh, M. S.; Su, H. J.; Hsieh, P. L.; Chiang, Y. W.; Huang, M. H. Synthesis of Ag_3PO_4 Crystals with Tunable Shapes for Facetdependent Optical Property, Photocatalytic Activity, and Electrical Conductivity Examinations. ACS Appl. Mater. Interfaces 2017, 9, 39086−39093.
(13) Wu, A.; Tian, C.; Chang, W.; Hong, Y.; Zhang, Q.; Qu, Y.; Fu, H. Morphology-controlled Synthesis of Ag_3PO_4 Nano/microcrystals and their Antibacterial Properties. Mater. Res. Bull. 2013, 48, 3043− 3048.
(14) Liu, J.-K.; Luo, C.-X.; Wang, J.-D.; Yang, X.-H.; Zhong, X.-H. Controlled Synthesis of Silver Phosphate Crystals with High Photocatalytic Activity and Bacteriostatic Activity. CrystEngComm 2012, 14, 8714.
(15) Deng, C.-H.; Gong, J.-L.; Ma, L.-L.; Zeng, G.-M.; Song, B.; Zhang, P.; Huan, S.-Y. Synthesis, Characterization and Antibacterial Performance of Visible Light-responsive Ag_3PO_4 Particles Deposited on Graphene Nanosheets. Process Saf. Environ. Prot. 2017, 106, 246− 255.
(16) Seo, Y.; Yeo, B.-E.; Cho, Y.-S.; Park, H.; Kwon, C.; Huh, Y.-D. Photo-enhanced Antibacterial Activity of Ag_3PO_4. Mater. Lett. 2017, 197, 146−149.
(17) Zhang, Y.; Zhang, X.; Hu, R.; Yang, Y.; Li, P.; Wu, Q. Bifunctional Nano-Ag_3PO_4 with Capabilities of Enhancing Ceftazidime for Sterilization and Removing Residues. RSC Adv. 2019, 9, 17913−17920.
(18) Shao, J.; Ma, J.; Lin, L.; Wang, B.; Jansen, J. A.; Walboomers, X. F.; Zuo, Y.; Yang, F. Three-dimensional Printing of Drug-loaded Scaffolds for Antibacterial and Analgesic Applications. Tissue Eng., Part C 2019, 25, 222−231.
(19) Weng, B.; Qi, M.-Y.; Han, C.; Tang, Z.-R.; Xu, Y.-J. Photocorrosion Inhibition of Semiconductor-based Photocatalysts: Basic Principle, Current Development, and Future Perspective. ACS Catal. 2019, 9, 4642−4687.
(20) Zwara, J.; Grabowska, E.; Klimczuk, T.; Lisowski, W.; ZaleskaMedynska, A. Shape-dependent Enhanced Photocatalytic Effect under Visible Light of Ag_3PO_4 Particles. J. Photochem. Photobiol., A 2018, 367, 240−252.
(21) Chen, X.; Dai, Y.; Wang, X. Methods and Mechanism for Improvement of Photocatalytic Activity and Stability of Ag_3PO_4: A Review. J. Alloys Compd. 2015, 649, 910−932.
(22) Li, X.; Xu, P.; Chen, M.; Zeng, G.; Wang, D.; Chen, F.; Tang, W.; Chen, C.; Zhang, C.; Tan, X. Application of Silver Phosphatebased Photocatalysts: Barriers and Solutions. Chem. Eng. J. 2019, 366, 339−357.
(23) Zhang, S.; Zhang, S.; Song, L. Super-high Activity of Bi^{3+} Doped Ag_3PO_4 and Enhanced Photocatalytic Mechanism. Appl. Catal., B 2014, 152−153, 129−139.

(24) Afif, M.; Saulaeman, U.; Riapanitra, A.; Andreas, R.; Yin, S. Use′ of Mn Doping to Suppress Defect Sites in Ag_3PO_4: Applications in Photocatalysis. Appl. Surf. Sci. 2019, 466, 352−357.
(25) Yu, H.; Kang, H.; Jiao, Z.; Lü, G.; Bi, Y. Tunable Photocatalytic Selectivity and Stability of Ba-doped Ag_3PO_4 Hollow Nanosheets. Chin. J. Catal. 2015, 36, 1587−1595.
(26) Song, L.; Chen, Z.; Li, T.; Zhang, S. A Novel Ni^{2+}-doped Ag_3PO_4 Photocatalyst with High Photocatalytic Activity and Enhancement Mechanism. Mater. Chem. Phys. 2017, 186, 271−279.
(27) Cao, W.; Gui, Z.; Chen, L.; Zhu, X.; Qi, Z. Facile Synthesis of Sulfate-doped Ag_3PO_4 with Enhanced Visible Light Photocatalystic Activity. Appl. Catal., B 2017, 200, 681−689.
(28) Luo, J.; Luo, Y.; Li, Q.; Yao, J.; Duan, G.; Liu, X. Synthesis of Doughnut-like Carbonate-doped Ag_3PO_4 with Enhanced Visible Light Photocatalytic Activity. Colloids Surf., A 2017, 535, 89−95.
(29) Liu, X.; Ma, R.; Zhuang, L.; Hu, B.; Chen, J.; Liu, X.; Wang, X. Recent Developments of Doped g-C_3N_4 Photocatalysts for the Degradation of Organic Pollutants. Crit. Rev. Environ. Sci. Technol. 2020, 1−40.
(30) Botelho, G.; Andres, J.; Gracia, L.; Matos, L. S.; Longo, E. Photoluminescence and Photocatalytic Properties of Ag_3PO_4 Microcrystals: An Experimental and Theoretical Investigation. ChemPlusChem 2016, 81, 202−212.
(31) Botelho, G.; Sczancoski, J. C.; Andres, J.; Gracia, L.; Longo, E. Experimental and Theoretical Study on the Structure, Optical Properties, and Growth of Metallic Silver Nanostructures in Ag_3PO_4. J. Phys. Chem. C 2015, 119, 6293−6306.
(32) Cruz-Filho, J. F.; Costa, T. M. S.; Lima, M. S.; Silva, L. J.; Santos, R. S.; Cavalcante, L. S.; Longo, E.; Luz, G. E. Effect of Different Synthesis Methods on the Morphology, Optical Behavior, and Superior Photocatalytic Performances of Ag_3PO_4 Sub-microcrystals using White-light-emitting Diodes. J. Photochem. Photobiol., A 2019, 377, 14−25.
(33) Trench, A. B.; Machado, T. R.; Gouveia, A. F.; Assis, M.; da Trindade, L. G.; Santos, C.; Perrin, A.; Perrin, C.; Oliva, M.; Andres, J.; Longo, E. Connecting Structural, Optical, and Electronic Properties and Photocatalytic Activity of Ag_3PO_4:Mo Complemented by DFT Calculations. Appl. Catal., B 2018, 238, 198−211.
(34) Hussien, M. S. A.; Yahia, I. S. Visible Photocatalytic Performance of Nanostructured Molybdenum-doped Ag_3PO_4: Doping Approach. J. Photochem. Photobiol., A 2018, 356, 587−594.

(35) Li, H.; Zhang, Y.; Zhang, Q.; Wang, Y.; Fan, Y.; Gao, X.; Niu, J. Boosting Visible-light Photocatalytic Degradation of Indomethacin by an Efficient and Photostable Ag_3PO_4/NG/WO_3 Composites. Appl. Surf. Sci. 2019, 490, 481−491.

(36) Lu, J.; Wang, Y.; Liu, F.; Zhang, L.; Chai, S. Fabrication of a Direct Z-scheme Type WO_3/Ag_3PO_4 Composite Photocatalyst with Enhanced Visible-light Photocatalytic Performances. Appl. Surf. Sci. 2017, 393, 180−190.

(37) Shi, H.; Yang, S.; Han, C.; Niu, Z.; Li, H.; Huang, X.; Ma, J. Fabrication of Ag/Ag_3PO_4/WO_3 Ternary Nanoparticles as Superior Photocatalyst for Phenol Degradation under Visible light Irradiation. Solid State Sci. 2019, 96, No. 105967.

(38) Helmholz, L. The Crystal Structure of Silver Phosphate. J. Chem. Phys. 1936, 4, 316−322.

(39) Masse, R.; Tordjman, I.; Durif, A. Refinement of Crystalstructure of Silver Monophosphate, Ag_3PO_4-Existence of Hightemperature Form. Z. Kristallogr. 1976, 144, 76−81.

(40) Ng, H. N.; Calvo, C.; Faggiani, R. A New Investigation of the Structure of Silver Orthophosphate. Acta Crystallogr. B 1978, 34, 898−899.

(41) Deschizeaux-Cheruy, M. N.; Aubert, J. J.; Joubert, J. C.;́ Capponi, J. J.; Vincent, H. Relation entre Structure et Conductivite Ionique Basse Temperature de Ag_3PO_4. Solid State Ionics 1982, 7, 171−176.

(42) Katsumata, H.; Sakai, T.; Suzuki, T.; Kaneco, S. Highly Efficient Photocatalytic Activity of g-C_3N_4/Ag_3PO_4 Hybrid Photocatalysts through Z-scheme Photocatalytic Mechanism under Visible Light. Ind. Eng. Chem. Res. 2014, 53, 8018−8025.

(43) Herschbach, D. R.; Laurie, V. W. Anharmonic Potential Constants and their Dependence upon Bond Length. J. Chem. Phys. 1961, 35, 458−464.

(44) Zavitsas, A. A. Factors Affecting the Relation between Stretching Frequencies and Bond Lengths. Diatomic and polyatomic species without adjustable fitting parameters. Spectrochim. Acta, Part A 2015, 151, 553−565.

(45) Holland, P. L. Metal-dioxygen and Metal-dinitrogen Complexes: Where are the Electrons Dalton Trans. 2010, 39, 5415−5425.

(46) Bertus, L. M.; Faure, C.; Danine, A.; Labrugere, C.; Campet, G.; Rougier, A.; Duta, A. Synthesis and Characterization of WO_3 thin Films by Surfactant Assisted Spray Pyrolysis for Electrochromic Applications. Mater. Chem. Phys. 2013, 140, 49−59.

(47) Liu, Y.; Fang, L.; Lu, H.; Li, Y.; Hu, C.; Yu, H. One-pot Pyridine-assisted Synthesis of Visible-light-driven Photocatalyst Ag/ Ag_3PO_4. Appl. Catal., B 2012, 115−116, 245−252.

(48) Zhang, H.; Wang, G.; Chen, D.; Lv, X.; Li, J. Tuning Photoelectrochemical Performances of Ag-TiO_2 Nanocomposites via Reduction/Oxidation of Ag. Chem. Mater. 2008, 20, 6543−6549.

(49) Cheng, Z.; Bing, F.; Liu, Q.; Zhang, Z.; Fang, X. Novel Zscheme Visible-light-driven Ag_3PO_4/Ag/SiC Photocatalysts with Enhanced Photocatalytic Activity. J. Mater. Chem. A 2014, 3, 1−3.

(50) Xu, Y.-S.; Zhang, W.-D. Morphology-controlled Synthesis of Ag_3PO_4 Microcrystals for High Performance Photocatalysis. CrystEngComm 2013, 15, 5407.

(51) Ma, X.; Lu, B.; Li, D.; Shi, R.; Pan, C.; Zhu, Y. Origin of Photocatalytic Activation of Silver Orthophosphate from Firstprinciples. J. Phys. Chem. C 2011, 115, 4680−4687.

(52) Kubelka, P.; Munk, F. Ein Beitrag zur Optik der Farbanstriche. Z. Tech. Phys. 1931, 12, 593−601.

(53) Wood, D. L.; Tauc, J. Weak Absorption Tails in Amorphous Semiconductors. Phys. Rev. B: Condens. Matter Mater. Phys. 1972, 5, 3144−3151.

(54) Ge, M.; Zhu, N.; Zhao, Y.; Li, J.; Liu, L. Sunlight-assisted Degradation of Dye Pollutants in Ag_3PO_4 Suspension. Ind. Eng. Chem. Res. 2012, 51, 5167−5173.

(55) Tang, C.; Liu, E.; Wan, J.; Hu, X.; Fan, J. Co_3O_4 Nanoparticles Decorated Ag_3PO_4 Tetrapods as an Efficient Visible-light-driven Heterojunction Photocatalyst. Appl. Catal., B 2016, 181, 707−715.

(56) Teoh, W. Y.; Scott, J. A.; Amal, R. Progress in Heterogeneous Photocatalysis: From Classical Radical Chemistry to Engineering Nanomaterials and Solar Reactors. J. Phys. Chem. Lett. 2012, 3, 629− 639.

(57) Banerjee, S.; Pillai, S. C.; Falaras, P.; O'Shea, K. E.; Byrne, J. A.; Dionysiou, D. D. New Insights into the Mechanism of Visible Light Photocatalysis. J. Phys. Chem. Lett. 2014, 5, 2543−2554.

(58) Chen, L.; Yang, S.; Huang, Y.; Zhang, B.; Kang, F.; Ding, D.; Cai, T. Degradation of Antibiotics in Multi-component Systems With Novel Ternary AgBr/Ag_3PO_4@natural Hematite Heterojunction Photocatalyst under Simulated Solar Light. J. Hazard. Mater. 2019, 371, 566−575.

(59) Wang, F.; Feng, Y.; Chen, P.; Wang, Y.; Su, Y.; Zhang, Q.; Zeng, Y.; Xie, Z.; Liu, H.; Liu, Y.; Lv, W.; Liu, G. Photocatalytic Degradation of Fluoroquinolone Antibiotics using Ordered Mesoporous g-C_3N_4 under Simulated Sunlight Irradiation: Kinetics, Mechanism, and Antibacterial Activity Elimination. Appl. Catal., B 2018, 227, 114−122.

(60) Ahmadi, M.; Ramezani Motlagh, H.; Jaafarzadeh, N.; Mostoufi, A.; Saeedi, R.; Barzegar, G.; Jorfi, S. Enhanced Photocatalytic Degradation of Tetracycline and Real Pharmaceutical Wastewater using MWCNT/TiO_2 Nano-composite. J. Environ. Manage. 2017, 186, 55−63.
(61) Katsumata, H.; Taniguchi, M.; Kaneco, S.; Suzuki, T. Photocatalytic Degradation of Bisphenol A by Ag_3PO_4 under Visible Light. Catal. Commun. 2013, 34, 30−34.
(62) Global Action Plan on Antimicrobial Resistance. ⟨https://www. who.int/antimicrobial-resistance/global-action-plan/en/⟩ (accessed June 9, 2020).
(63) Vestergaard, M.; Frees, D.; Ingmer, H. Antibiotic Resistance and the MRSA Problem. Microbiol. Spectrum 2019, 7 (2), 1−23.
(64) Macedo, N. G.; Machado, T. R.; Roca, R. A.; Assis, M.; Foggi, C. C.; Puerto-Belda, V.; Mínguez-Vega, G.; Rodrigues, A.; SanMiguel, M. A.; Cordoncillo, E.; Beltran-Mir, H.; Andre´ s, J.; Longo, E. Tailoring the Bactericidal Activity of Ag Nanoparticles/α-Ag_2WO_4 Composite Induced by Electron Beam and Femtosecond Laser Irradiation: Integration of Experiment and Computational Modeling. ACS Appl. Bio Mater. 2019, 2, 824−837.
(65) Joya, Y. F.; Liu, Z.; Wang, T. Characterization and Antibacterial Functions of Ag−TiO_2 and W−TiO_2 Nanostructured thin Films Prepared by Sol-gel/Laser-induced Technique. Appl. Phys. B 2011, 105, 525−536.
(66) Jiang, X.; He, W.; Zhang, X.; Wu, Y.; Zhang, Q.; Cao, G.; Zhang, H.; Zheng, J.; Croley, T. R.; Yin, J.-J. Light-induced Assembly of Metal Nanoparticles on ZnO Enhances the Generation of Charge Carriers, Reactive Oxygen Species, and Antibacterial Activity. J. Phys. Chem. C 2018, 122, 29414−29425.
(67) Hong, Y.; Zeng, J.; Wang, X.; Drlica, K.; Zhao, X. Post-stress Bacterial Cell Death Mediated by Reactive Oxygen Species. Proc. Natl. Acad. Sci. U.S.A. 2019, 116, 10064−10071.
(68) Dovesi, R.; Orlando, R.; Erba, A.; Zicovich-Wilson, C. M.; Civalleri, B.; Casassa, S.; Maschio, L.; Ferrabone, M.; De La Pierre, M.; D'Arco, P.; Noel, Y.; Causa¨, M.; Re` rat, M.; Kirtman, B.´ CRYSTAL14: A Program for the ab Initio Investigation of Crystalline Solids. Int. J. Quantum Chem. 2014, 114, 1287−1317.
(69) Dovesi, R.; Saunders, V. R.; Roetti, C.; Orlando, R.; ZicovichWilson, C. M.; Pascale, F.; Civalleri, B.; Doll, K.; Harrison, N. M.; Bush, I. J.; D'Arco, P.; Llunel, M.; Causa, M.; Noe` l, Y.¨ CRYSTAL14 User's Manual, Theoretical Chemistry Group; University of Turin: Italy, 2014.
(70) Becke, A. D. Density-functional Thermochemistry. III. The Role of Exact Exchange. J. Chem. Phys. 1993, 98, 5648−5652.

(71) Lee, C.; Yang, W.; Parr, R. G. Development of the Colle-salvetti Correlation-energy Formula into a Functional of the Electron Density. Phys. Rev. B: Condens. Matter Mater. Phys. 1988, 37, 785−789.
(72) Crystal. ⟨http://www.crystal.unito.it/Basis_Sets/Ptable.html⟩ (accessed June 5, 2020).
(73) Hay, P. J.; Wadt, W. R. Ab Initio Effective Core Potentials for Molecular Calculations. Potentials for the Transition Metal Atoms Sc to Hg. J. Chem. Phys. 1985, 82, 270−283.
(74) de Foggi, C. C.; de Oliveira, R. C.; Fabbro, M. T.; Vergani, C. E.; Andres, J.; Longo, E.; Machado, A. L. Tuning the Morphological, Optical, and Antimicrobial Properties of α-Ag_2WO_4 Microcrystals Using Different Solvents. Cryst. Growth Des. 2017, 17, 6239−6246.
(75) CLSI. Methods for Dilution Antimicrobial Susceptibility Tests for Bacteria that Grow Aerobically; Clinical and Laboratory Standards Institute: Wayne, PA, 2006.
(76) Foggi, C. C.; Fabbro, M. T.; Santos, L. P. S.; de Santana, Y. V. B.; Vergani, C. E.; Machado, A. L.; Cordoncillo, E.; Andres, J.; Longo,´ E. Synthesis and Evaluation of α-Ag_2WO_4 as Novel Antifungal Agent. Chem. Phys. Lett. 2017, 674, 125−129.

Supporting Information

Rational design of W-doped Ag_3PO_4 as an efficient antibacterial agent and photocatalyst for organic pollutants degradation

Aline B. Trench,[†*] Thales R. Machado,[†*] Amanda F. Gouveia,[‡] Camila C. Foggi,[†] Vinícius Teodoro,[†] Isaac Sánchez-Montes,[†] Mayara M. Teixeira,[†] Letícia G. Trindade,[ǀ] Natalia Jacomaci,[¬]
Andre Perrin,[⊥] Christiane Perrin,[⊥] Jose M. Aquino,[†] Juan Andrés,[└] Elson Longo[†*]

[†] CDMF – Department of Chemistry, Federal University of São Carlos, 13565-905, São Carlos, SP, Brazil.

[‡] Institute of Chemistry, State University of Campinas, 13083-970, Campinas, SP, Brazil.

[ǀ] Department of Chemistry, São Paulo State University, 17033-360, Bauru, SP, Brazil.

[¬] Chemistry Institute, São Paulo State University, 14800-060, Araraquara, SP, Brazil.

[⊥] University of Rennes 1, Campus de Beaulieu, F-35042, Rennes-Cedex, France.

[└] Department of Analytical and Physical Chemistry, University Jaume I, 12071, Castellón, Spain.

Corresponding Author

* E-mail: aline_trench@hotmail.com (A.B. Trench)

*E-mail: tmachado.quimica@gmail.com (T.R. Machado)

*E-mail: elson.liec@gmail.com (E. Longo)

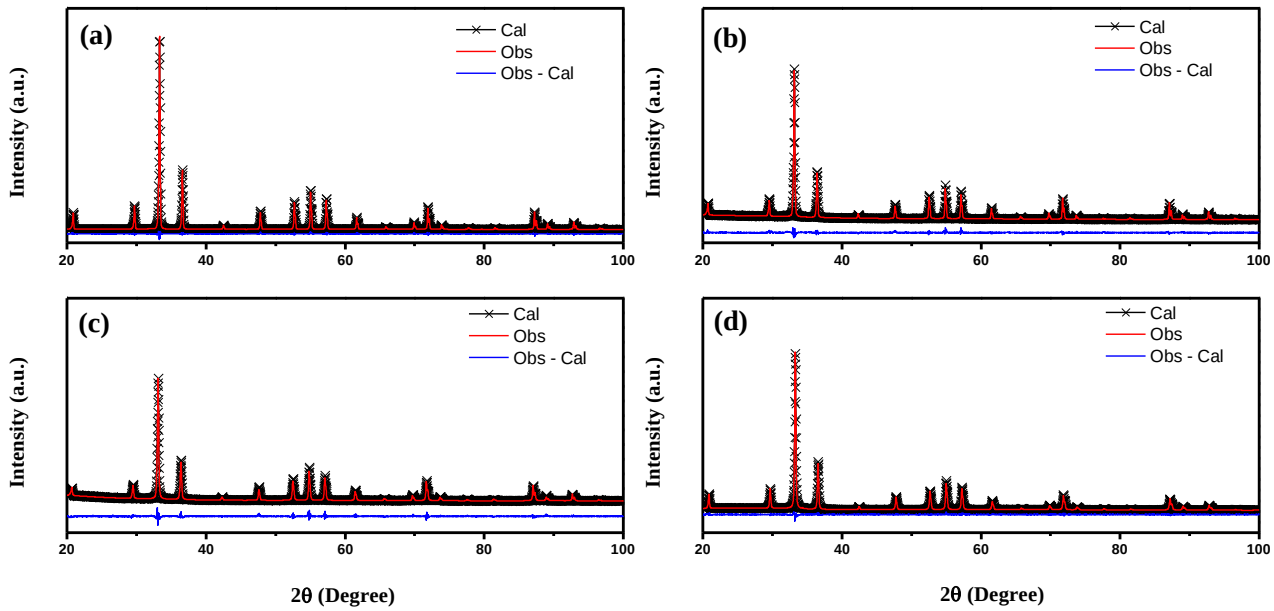

Figure S1. Rietveld refinement plots of pure Ag_3PO_4 (a), Ag_3PO_4: W 0.5% (b), Ag_3PO_4:W 1% (c), and Ag_3PO_4:W 2% (d).

Table S1. Rietveld refinements of pure Ag_3PO_4 and Ag_3PO_4:W powders.

Sample	**Lattice Parameters**	**Cell volume (Å)^3**	**R_{Bragg}**	**χ^2**	**R_{wp}**	**R_p**
	a=b=c (Å)			**(%)**	**(%)**	**(%)**
Ag_3PO_4	6.015570(18)	217.6860(20)	0.0605	2.36	8.75	6.43
W 0.5%	6.01740(4)	217.885(5)	0.0636	1.72	6.38	4.82
W 1%	6.01839(7)	217.992(8)	0.0651	1.95	7.45	5.52
W 2%	6.01685(15)	217.825(16)	0.0473	2.38	6.28	4.79

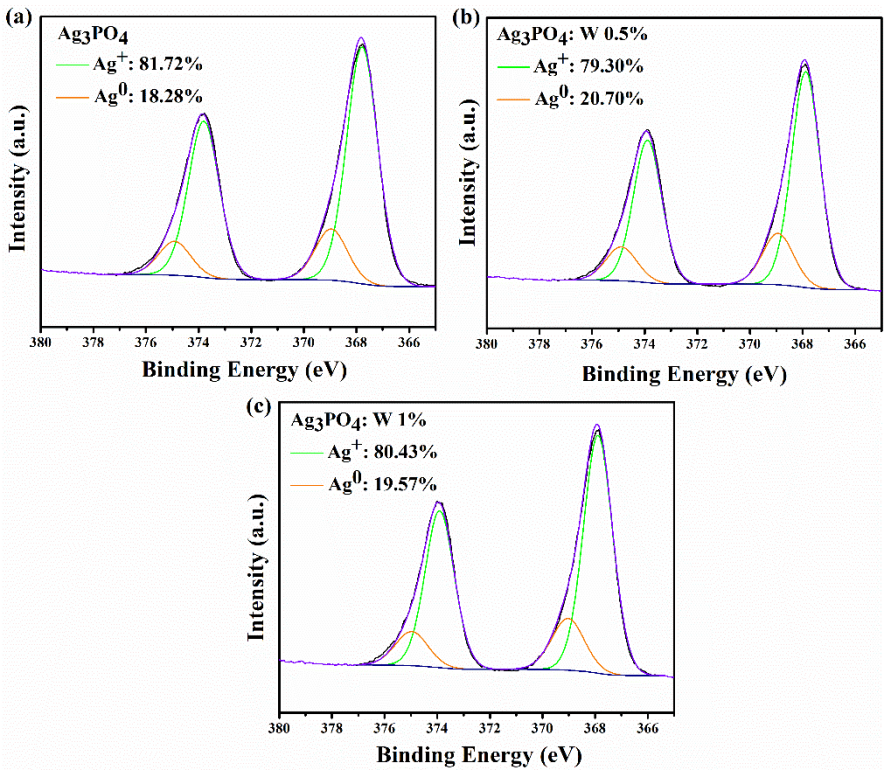

Figure S2. High-resolution XPS spectra of Ag 3d for Ag_3PO_4, Ag_3PO_4: W 0.5%, and Ag_3PO_4: W 1% samples.

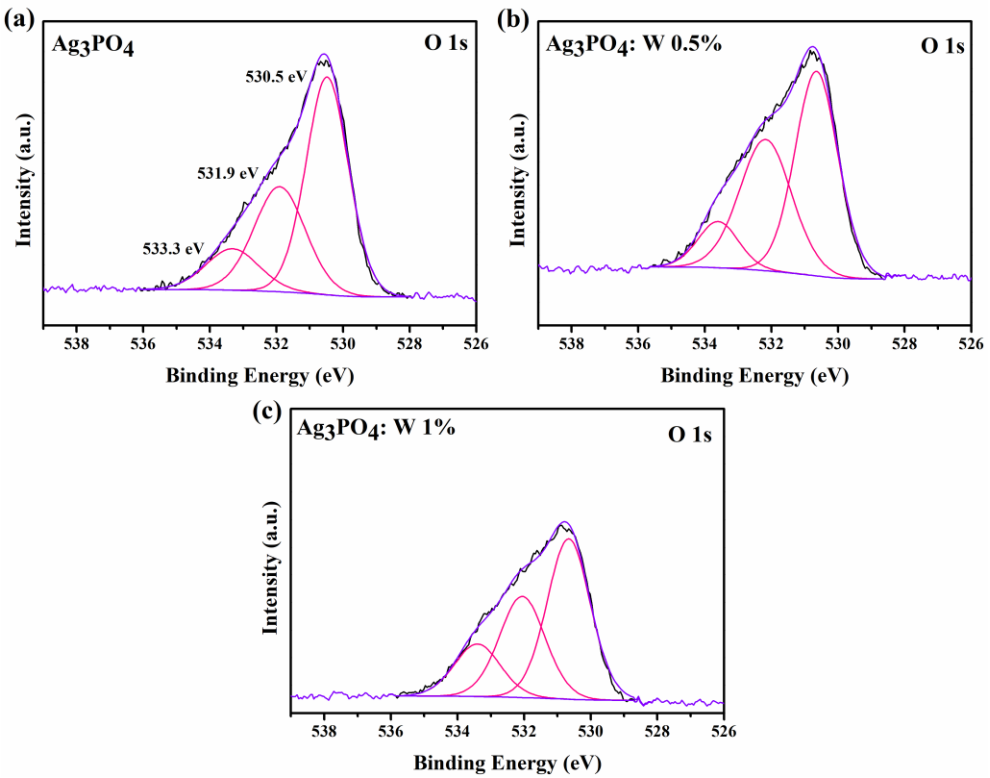

Figure S3. XPS spectrum of O 1s for pure Ag_3PO_4 (a), Ag_3PO_4:W 0.5% (b), and Ag_3PO_4:W1% (c) samples.

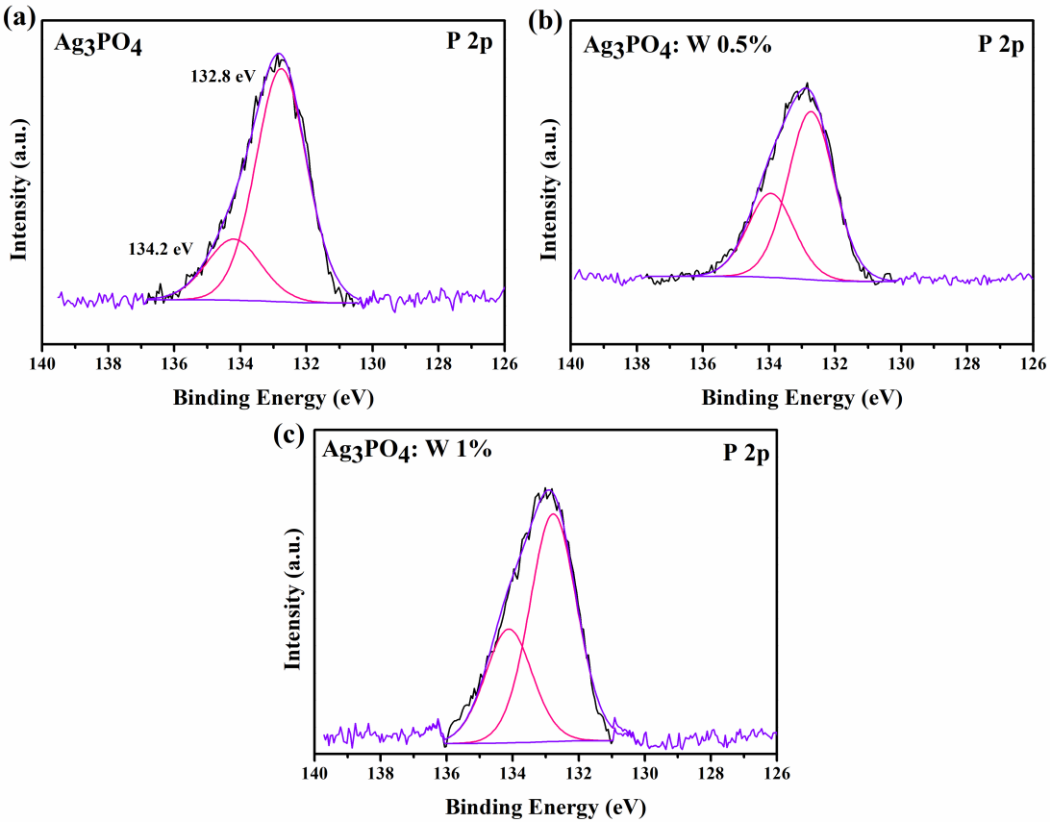

Figure S4. XPS spectrum of P 2p for pure Ag_3PO_4 (a), Ag_3PO_4:W 0.5% (b), and Ag_3PO_4:W 1% (c) samples.

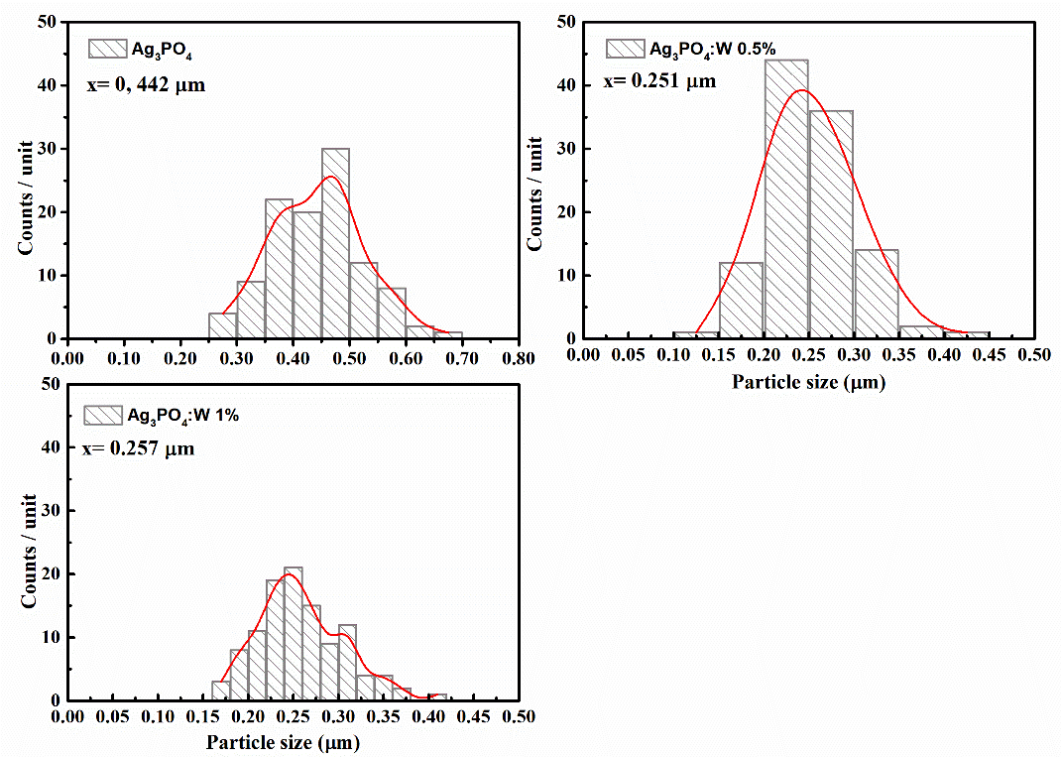

Figure S5. Particle size distribution for Ag_3PO_4, Ag_3PO_4:W 0.5%, and Ag_3PO_4:W 1%.

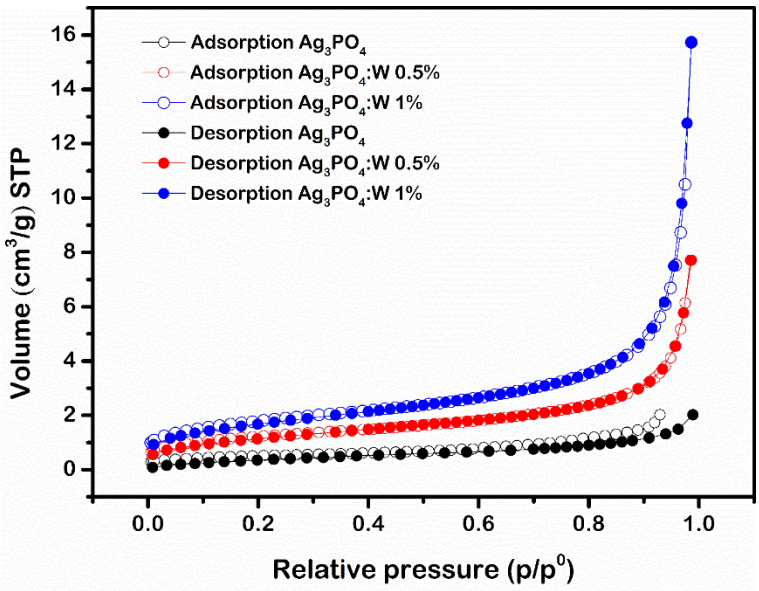

Figure S6. Adsorption-desorption isotherms of Ag_3PO_4, Ag_3PO_4:W 0.5%, and Ag_3PO_4:W 1%.

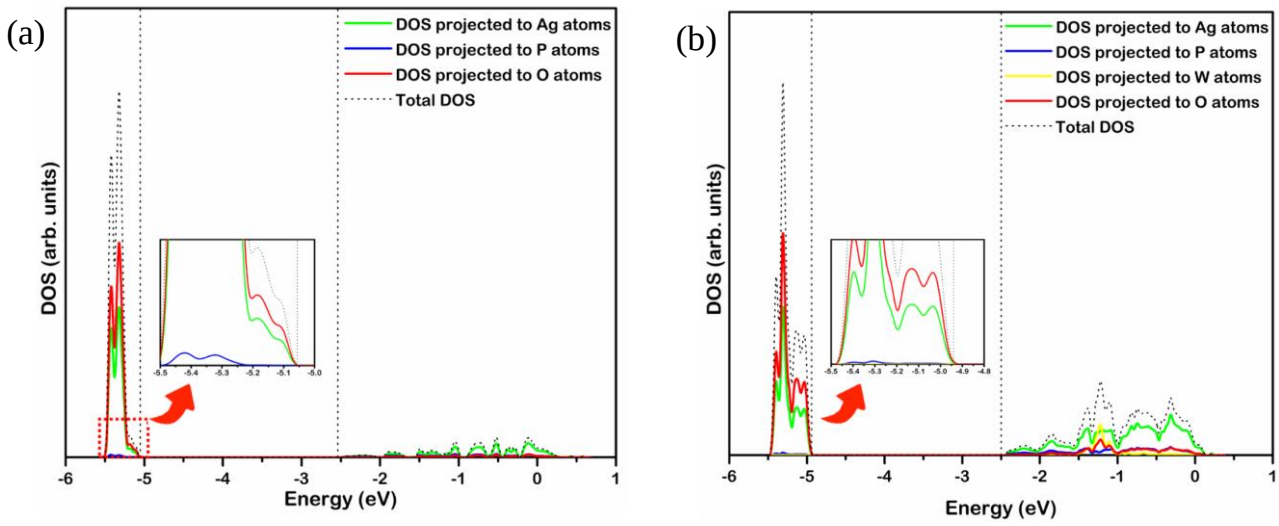

Figure S7. Density of states projected to the Ag, P and O atoms on the (a) Ag_3PO_4 and (b) Ag_3PO_4:W models.

3.2 – Interface matters: Design of an efficient α-Ag_2WO_4/Ag_3PO_4 photocatalyst

Materials Chemistry and Physics 280 (2022) 125710

Contents lists available at ScienceDirect

Materials Chemistry and Physics

journal homepage: www.elsevier.com/locate/matchemphys

Interface matters: Design of an efficient α-Ag_2WO_4/Ag_3PO_4 photocatalyst

Aline B. Trench [a], Roman Alvarez [a], Vinícius Teodoro [a], Letícia G. da Trindade [b], Thales R. Machado [a], Mayara M. Teixeira [a], Daniele de Souza [c], Ivo M. Pinatti [d], Alexandre Z. Simões [d], Yara Galvão Gobato [c], Juan Andrés [e], Elson Longo [a,*]

Interface matters: Design of an efficient α-Ag_2WO_4/Ag_3PO_4 photocatalyst

Aline B. Trench [a], Roman Alvarez [a], Vinícius Teodoro [a], Letícia G. da Trindade[b], Thales R. Machado [a], Mayara M. Teixeira [a], Daniele de Souza [c], Ivo M. Pinatti [d], Alexandre Z. Simões [d], Yara Galvão Gobato [c], Juan Andrés [e], Elson Longo [a,*]

[a] *CDMF – Department of Chemistry, Federal University of São Carlos, 13565-905, São Carlos, SP, Brazil*

[b] *Department of Chemistry, São Paulo State University, 17033-360, Bauru, SP, Brazil*

[c] *Department of Physics – Federal University of São Carlos, 13565-905, São Carlos, SP, Brazil*

[d] *Faculty of Engineering of Guaratinguetá, São Paulo State University (UNESP), 12516-410, Guaratinguetá, SP, Brazil*

[e] *Department of Analytical and Physical Chemistry, University Jaume I, 12071, Castellón, Spain*

ABSTRACT

Heterojunction engineering of complex metal oxides is an active area of research that addresses fundamental questions in solid-state systems with broad technological applications. In this work, α-Ag_2WO_4/Ag_3PO_4 heterojunctions with different amounts of α-Ag_2WO_4 (12, 24, and 36 wt%) were synthesized by the coprecipitation method and characterized by X-ray diffraction, X-ray photoelectron spectroscopy, field emission scanning electron microscopy, transmission electron microscopy, UV-vis diffuse reflectance spectroscopy, and photoluminescence. The α-Ag_2WO_4/Ag_3PO_4 heterojunction containing 24% wt of α-Ag_2WO_4 showed the most enhanced photocatalytic activity for the degradation of Rhodamine B, being much higher than Ag_3PO_4 and α-Ag_2WO_4. Trapping experiments revealed that the holes and superoxide radical, in minor extent, were the main active species in the photocatalytic degradation. Such enhanced photocatalytic performance was explained by the surface plasmon resonance effect associated with the presence of metallic Ag at the interface and the formation of a type I heterojunction between α-Ag_2WO_4 and Ag_3PO_4 semiconductors.

Keywords: α-Ag_2WO_4/Ag_3PO_4, photocatalytic activity, surface plasmon resonance, type I heterojunction.

1. Introduction

Over the past few years, semiconductor photocatalysis has attracted much interest due the synthesis of innovative materials with excellent performance for organic

pollutant degradation and waste water cleaning [36, 53]. A highly efficient semiconductor needs to have a wide range of light absorption, a fast charge separation of photo-generated electron-hole (e^-—h^+) pairs and a strong redox ability [54] [55-58]. However, it is difficult for a single-component photocatalyst to possess all these characteristics.

To overcome these drawbacks and improve the performance of a single semiconductor, in the last years two feasible methods emerged via a synergistic interaction/effect [59]. The firs refers to the formation of a heterojunction involving the combination of two or more semiconductors to form new materials [50, 60-67]. This strategy constitutes a hotspot in recent research [36, 68-74] to obtain new materials with superior electrical, optical, and catalytic properties associated with the transfer of interfacial charge and a synergistic effect between coupled semiconductors [75]. The second concerns the deposition of active metal nanoparticles (NPs) (for example, noble metals, such as Ag, Au or/and Cu nanoparticles), displaying localized surface plasmon resonance (SPR) effect on the semiconductor´s surface [76, 77]. In the first case, the photocatalytic activity of the heterojunction depends on the semiconductor type (p or n), chemical composition, band alignment, and location of valence/conduction band potentials.

The combination of metal and semiconductor significantly enhances the activity because of two main features: the formation of a Schottky barrier between the metal NPs, resulting in the increased separation efficiency of photogenerated (e^-—h^+) pairs [78]. The high electron trapping ability of NPs help to effectively promote the conductivity of NPs, which can then be directly injected into the conduction band of the semiconductors, facilitating the charge separation at the interface between NPs and the semiconductor, and consequently improving its photocatalytic ability [47, 79-91].

The interface causes induced e^- and h^+ in or near this area to move in opposite directions, promoting charge transfer and suppressing the recombination of e^-—h^+ pairs, thus increasing their stability [92] and maximizing the redox power for heterojunction photocatalysts. This quantum phenomenon occurs in a confined region and is capable of enhancing the simultaneous (successive or parallel) transformation of compounds. As it occurs in other Ag-based semiconductors, both Ag_3PO_4 and α-Ag_2WO_4 are unstable and tend to segregate Ag metal nanoparticles (Ag NPs) on the surfaces of these complex oxides, hence forming Ag NPs/Ag_3PO_4 and Ag NPs/α-Ag_2WO_4 composites, respectively. These composites present SPR effect associated with the easy formation of Ag NPs on the surface of these semiconductors [80, 82, 87, 90, 93-97].

Despite the practical importance of such composites and the fact that they have been observed for different types of heterojunction [98], so far there is a lack of studies in the literature on a consistent pattern demonstrating the synergistic influence of plasmons of Ag NPs on their photocatalytic activity. Inspired by the unique properties of both Ag_3PO_4 and α-Ag_2WO_4, it was envisaged that the coupling of the heterojunction of both materials with presence of Ag NPs at the interface could provide additional active sites, significantly improving their photocatalytic property. Therefore, the aim of the present work was to obtain a α-Ag_2WO_4/Ag_3PO_4 heterojunction via a facile coprecipitation method in order to contribute to the discussions on the topic. To this end, a wide range of α-Ag_2WO_4 compositions (12, 24, and 36 wt%) was used. The as-synthetized heterojunctions were fully characterized by X-ray diffraction (XRD), X-ray photoelectron spectroscopy (XPS), transmission electron microscopy (TEM), field emission gun scanning electron microscopy (FE-SEM) and diffuse reflectance spectroscopy in the ultraviolet-visible region (UV-vis). This work can also provide important understanding on the role played by Ag NPs at the interface of these heterojunctions during the photocatalytic process of Rhodamine B (RhB) dye degradation. After systematically characterizing and evaluating the properties of the photocatalyst, it was possible to observe that this heterojunction exhibited higher photoactivity than pure counterparts. Based on the scavenger results, the photocatalytic mechanism was proposed and discussed in detail. Finally, the stability of the material was studied via recycling and reusability experiments.

2. Experimental section

2.1 Synthesis

Ag_3PO_4 sample was synthesized by the coprecipitation method in aqueous medium at 30 °C. 50 mL of deionized water and $(NH_4)_2HPO_4$ salt (0.001 mol,) (98.6%, JT Baker) were added to a beaker. This solution was stirred at 30 °C for 10 minutes for complete salt dissolution. In another beaker, the same procedure was performed using 50 mL of deionized water and $AgNO_3$ salt (0.003 mol) (99.8%, Vetec). After salt dissolution, the solution containing $AgNO_3$ was added to the $(NH_4)_2HPO_4$ solution and kept under stirring for 10 minutes at 30 °C. Subsequently, the formed precipitate was washed with deionized water to remove residual ions, and then dried in a conventional oven at 60 °C for 12 hours.

The α-Ag_2WO_4 crystals were also prepared by the coprecipitation method at room temperature. $Na_2WO_4 \cdot 2H_2O$ (0.007M) (99.5%, Sigma-Aldrich) and $AgNO_3$ (0.0035M) (99.8 %, Sigma Aldrich) were stirred separately in a solution containing 50 mL of deionized water at room temperature until the complete dissolution of the salts. Afterwards, the $AgNO_3$

solution was added to the Na_2WO_4 solution and stirred for 10 minutes. The formed precipitate was washed with deionized water to remove residual ions, and then dried in a conventional oven at 60 °C for 12 hours.

Stoichiometric contents of precursors reagents for α-Ag_2WO_4 and Ag_3PO_4 were used to obtain α-Ag_2WO_4/Ag_3PO_4 heterojunction with 12, 24 and 36 wt% of α-Ag_2WO_4 in relation to Ag_3PO_4, which were denominated as AWP 1, AWP 2 and AWP 3, respectively. For this purpose, α-Ag_2WO_4 was dispersed in a beaker containing 20 mL of deionized water at 30 °C under constant agitation. In another beaker, $(NH_4)_2HPO_4$ salt was dissolved in 20 mL of deionized water at 30 °C under constant stirring. This solution was added to the beaker containing the dispersed α-Ag_2WO_4 and kept under stirring at 30 °C for 10 minutes. Another solution was prepared using 20 mL of deionized water and $AgNO_3$, which was dissolved under stirring at 30 °C. This solution was dripped onto the suspension containing α-Ag_2WO_4 and $(NH_4)_2HPO_4$, and the whole mixture was stirred for 10 minutes. The precipitate formed was washed with deionized water to remove residual ions, and then dried in a conventional oven at 60 °C for 12 hours.

2.2 Characterization

The obtained materials were characterized by XRD diffraction using a D/Max-2500PC diffractometer (Rigaku, Japan) with CuKα radiation (λ = 1.54056 Å) in the 2θ range of 10° to 80° at a scanning speed of 1ºmin^{-1} and step size of 0.02°. Transmission electron microscopy (TEM) was performed using a FEI Tecnai G2F20 (Netherlands) microscope operating at 200 kV. Dark field (DF) image as well as local compositional analyses and mapping via energy-dispersive X-ray spectroscopy (EDS) were recorded in the scanning TEM (STEM) mode. The morphologies of the samples were characterized by field emission gun scanning electron microscopy (FE-SEM) in a FEI instrument (Inspection Model F50) operating at 10 kV.

Measurements of X-ray photoelectron spectroscopy (XPS) were performed on a Scientia Omicron ESCA + (Germany) spectrometer using monochromatic Al Kα (1486.7 eV). The maximum deconvolution was performed using a Gaussian (70%)–Lorentzian (30%) line with Shirley nonlinear sigmoid-type baseline. For calibration of the binding energy of the elements, peak C 1s at 248.8 eV was used as a reference. To obtain ultraviolet-visible (UV-vis) absorption spectra, a Varian Cary 5G (United States) spectrophotometer was used in diffuse reflection mode.

Photoluminescence (PL) measurements were performed by using a 500M SPEX spectrometer coupled to a GaAs-PMT detector. A Kimmon He-Cd laser (325nm line) was used

as excitation source. The PL measurements were performed in the range of 380-750 nm with laser power of about 16 mW and at 300K.

2.3 Photocatalytic measurements

The photocatalytic activity of Ag_3PO_4, α-Ag_2WO_4 and heterojunction samples AWP 1, AWP 2 and AWP 3 were tested for Rhodamine B (RhB) discoloration (95%, Aldrich) under visible light irradiation. For the photocatalytic experiments, 50 mg of each sample and 50 mL of RhB (10 mg L^{-1}) were placed in a beaker, and later in an ultrasonic bath (Branson, model 1510; frequency 42 kHz) for 15 minutes, followed by stirring for another 30 minutes, always keeping samples in the dark. An aliquot was collected at time 0, and the RhB solution containing the catalyst was exposed to the irradiation of 6 lamps (Philips TL-D, 15 W). The entire system was maintained at a constant temperature of 20 °C. Aliquots were removed at certain times (0, 2, 5, and 10 minutes). All aliquots were centrifuged, and their degradation was monitored by measuring the peak of maximum RhB absorption (λ_{max} = 554 nm) using a UV-visible spectrophotometer (V-660, JASCO). A control experiment was carried out under the same conditions, but without the presence of catalysts.

To elucidate the mechanism of α-Ag_2WO_4/Ag_3PO_4 photocatalytic activity enhancement, the main active species that participated in the photocatalytic reaction were investigated. The free radicals and holes trapping experiments were carried out. The scavenger experiments were performed by the addition of tert-butyl alcohol (TBA, 0,012 mol/L) (Alfa Aesar), ammonium oxalate (AO, 0.012 mol/L) (Alfa Aesar) and benzoquinone (BQ, 0.012 mol/L) (Alfa Aesar) as scavengers of hydroxyl radical (•OH), hole (h^+) and superoxide radical (•O_2^-), respectively.

3. Results and discussion

3.1. Powders characterization

The Ag_3PO_4 and α-Ag_2WO_4 were synthesized by the coprecipitation method, as previously reported [34, 99]. The heterojunctions containing 12, 24 and 36 wt% of α-Ag_2WO_4 in relation to Ag_3PO_4 were synthesized as shown in Figure 1, and denoted as AWP 1, AWP 2 and AWP 3, respectively.

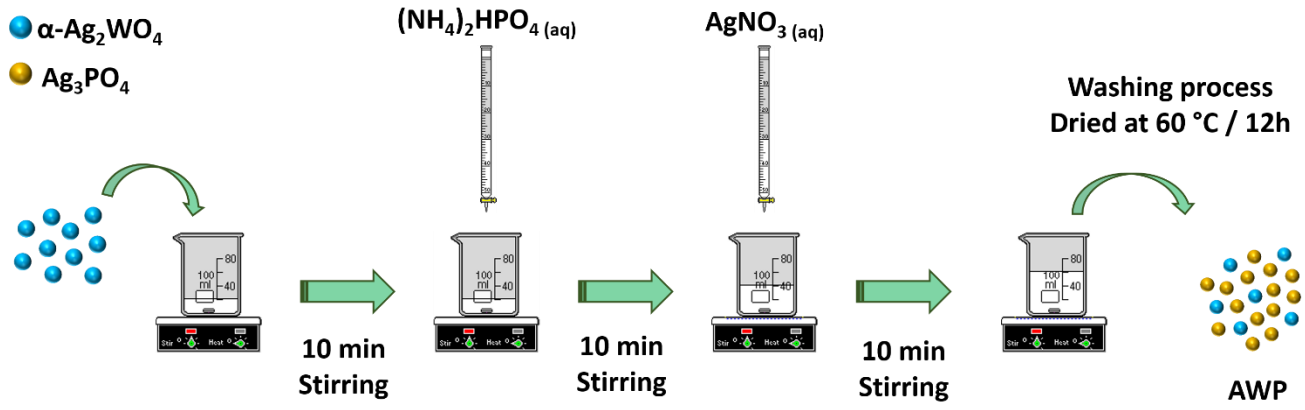

Figure 1. Schematic representation of the synthesis procedure.

Figure S1 in Supplementary Information, shows the XRD patterns of the Ag_3PO_4, AWP 1, AWP 2, AWP 3 and α-Ag_2WO_4 samples. The XRD pattern of the Ag_3PO_4 sample are in good agreement with the Inorganic Crystal Structure Database (ICSD) No. 14000, with a cubic structure and $P\bar{4}3n$ space group [100]. On the other hand, the α-Ag_2WO_4 sample has an orthorhombic structure with a *Pn2n* space group, according to ICSD No. 4165 [101].

It was observed that as the amount of α-Ag_2WO_4 increased, the XRD peaks referring to this phase intensified, which is well expected due to the higher content of this material. No characteristic peaks related to any impurities or secondary phase were noted, suggesting that the samples presented only α-Ag_2WO_4 and Ag_3PO_4 phases.

TEM analysis was performed for the sample with an intermediate amount of α-Ag_2WO_4 (AWP 2). Figure 2(a) shows a low-magnified DF-STEM image, where two main arrangement of particles in this sample comprising faceted nanospheres and elongated irregular microparticles covered by these nanospheres can be seen. Figure 2(b) shows a magnified view corresponding to the dotted square marked in Figure 2(a). An elemental characterization by EDS was conducted in the microparticle and nanospheres, as shown in Figure 2(b). The resulting EDS spectrum for the microparticle indicates the predominance of the elements Ag, P, W and O, whereas the irregular nanospheres are mainly composed of Ag, P and O. Figures 2 (c-f) show the EDS mapping of the elements Ag, P, W and O corresponding to the region in

(b), again confirming the presence of the elements referring to the heterojunction and the homogeneity of the sample.

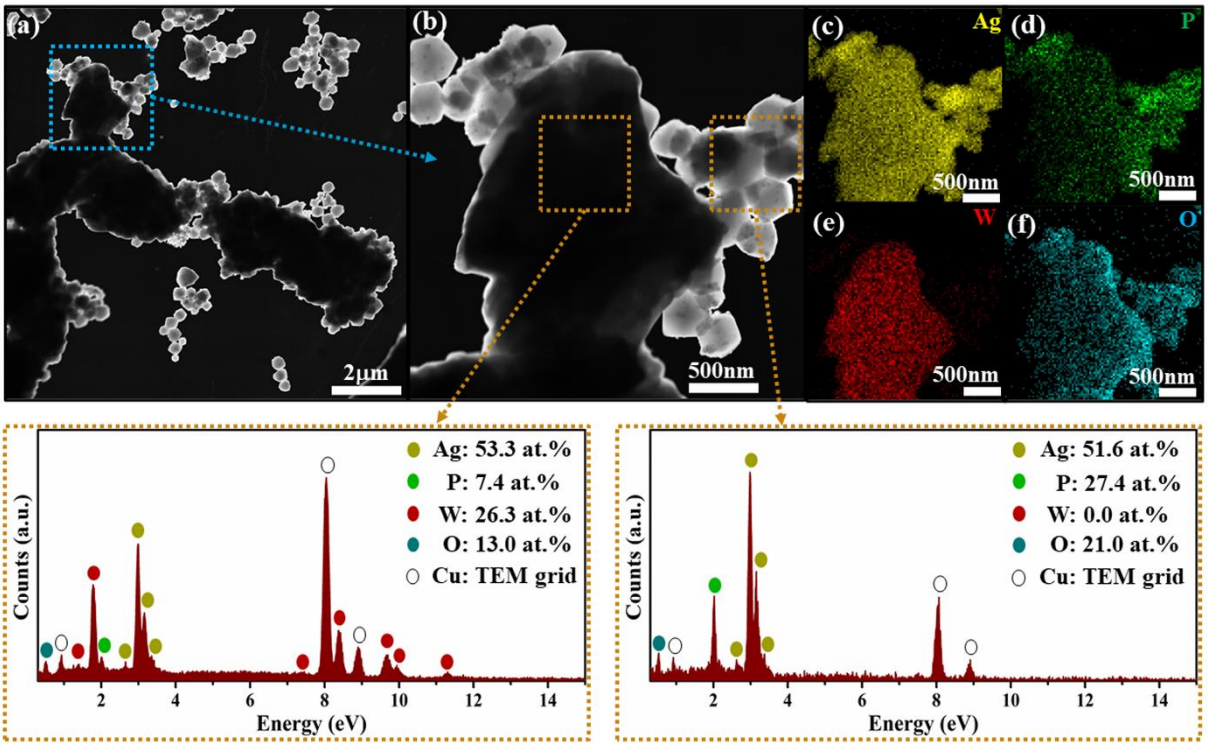

Figure 2. TEM characterization of sample AWP 2: (a) DF-STEM image, (b) high-magnification DF-STEM image and EDS spectra obtained at Ag_3PO_4 crystallized on α-Ag_2WO_4 surface, and (c-f) EDS mapping of the elements Ag, P, W, and O corresponding to the region in (b).

To complement this result, selected area electron diffraction (SAED) analyses (insets in Figure 3) were conducted in the same region of Figure 2 (b), and as indicated by the dotted arrows they reveal patterns typically observed in polycrystalline materials. The nanospheres exhibit concentric rings that can be indexed to the (220), (310), and (520) families of planes of the cubic Ag_3PO_4, while the patterns on the elongated microparticle reveal the presence of both (402) and (633) families of planes of the α-Ag_2WO_4 structure, and (233) family of planes associated with the Ag_3PO_4 structure. These results confirm the successful formation of Ag_3PO_4 nanospheres and their crystallization on the surface of α-Ag_2WO_4 microcrystals, forming the heterojunction.

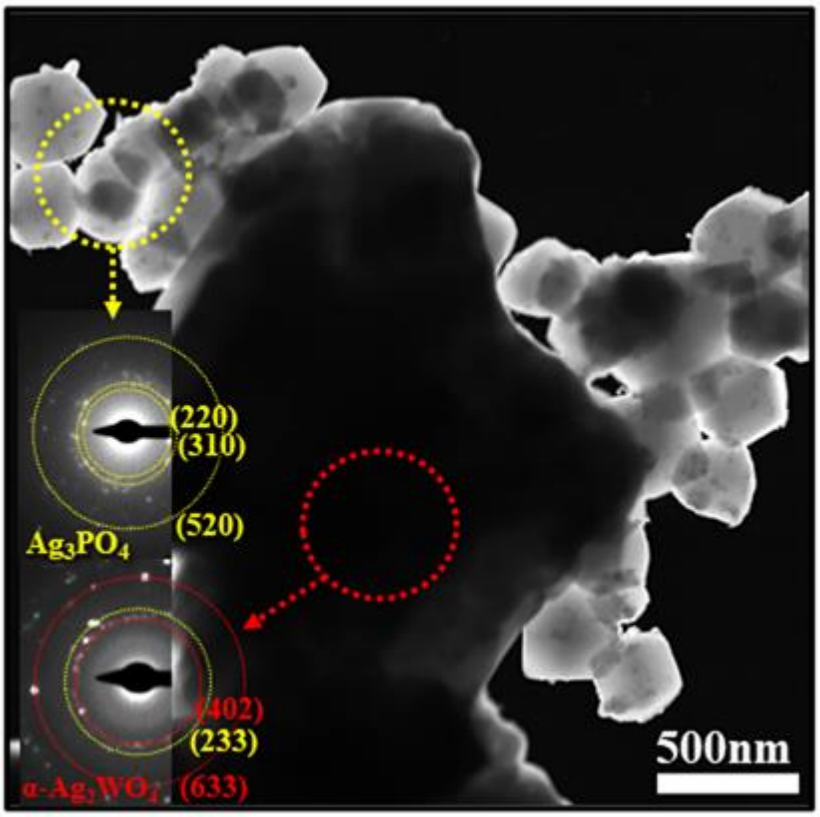

Figure 3. DF-STEM image and its corresponding SAED patterns of sample AWP 2.

Figure 4 shows the micrographs of the pure materials and the heterojunction formed in different proportions. The Ag_3PO_4 structure, represented by the orange color, exhibits a morphology with irregular nanospheres (Figure 4(a)), while the α-Ag_2WO_4 structure, represented by the blue color, displays a morphology with hexagonal microrods (Figure 4(b)). In the heterojunction (Figures 4(c-e)), it can be seen that the interaction of the materials during the synthesis process causes changes in the morphology of both materials. As presented in the TEM analysis, the elongated irregular blue microparticle is composed of the α-Ag_2WO_4 structure, whereas the smaller nanosphere orange particles are formed by the Ag_3PO_4 structure. The change in the morphology of the heterojunction is due to the dissolution and recrystallization of the rods in aqueous medium, which consequently formed larger faceted microparticles. Sample AWP1 showed an agglomerate of particles that coalesced to form a large microparticle represented by the blue color, which can be attributed to the α-Ag_2WO_4 structure (Figure 4(c)). Samples AWP2 and AWP3, on the other hand, were characterized by the presence of large microparticles with well-defined surfaces (Figures 4(d-e)). EDS results revealed that the α-Ag_2WO_4 microparticles were covered by the elements Ag, P and O, with the smaller nanoparticles corresponding to the Ag_3PO_4 structure. Moreover, the Ag_3PO_4 nanoparticles presented more defined surfaces in the heterojunction.

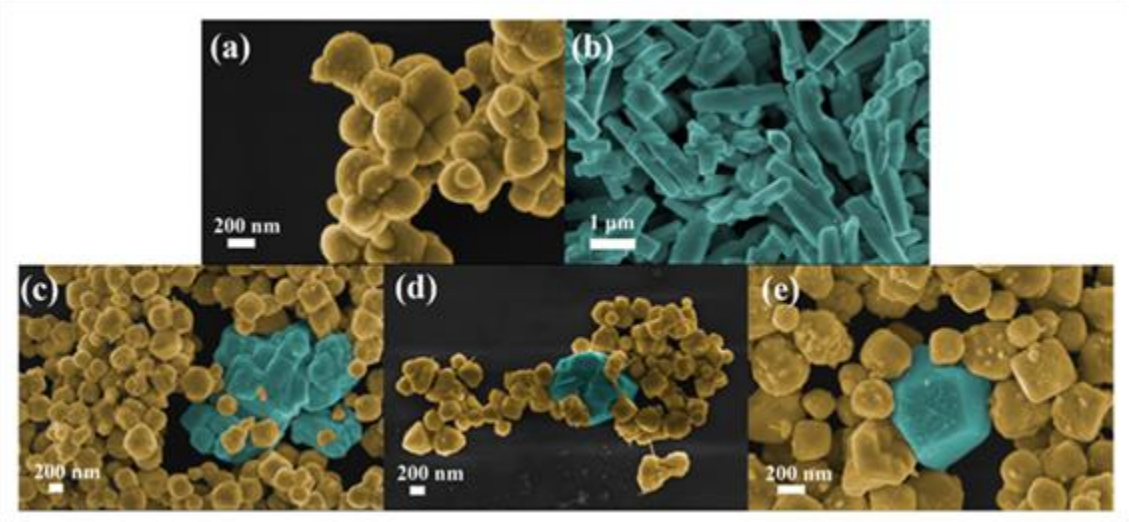

Figure 4. FE-SEM images of (a) Ag_3PO_4 (orange color), (b) α-Ag_2WO_4 (blue color), (c) AWP 1, (d) AWP 2 and (e) AWP 3.

To investigate the chemical composition and surface structure of the as-prepared samples, XPS measurements were carried out. The analysis of the high-resolution spectra of the constituent elements of α-Ag_2WO_4 and Ag_3PO_4 samples is presented in Figure S2. The deconvolution analysis of the P 2*p* spectrum of Ag_3PO_4 as well the W 4*f* spectrum of α-Ag_2WO_4 indicates the presence of P^{5+} and W^{6+} oxidation states, as shown in Figure S2(b) and Figure S2(e), respectively [102, 103]. The deconvolution analysis of the Ag 3*d* spectra for both Ag_3PO_4 and α-Ag_2WO_4 samples reveals the presence of Ag^+ and Ag^0 oxidation states according to their respective spin-orbit coupling peaks, as demonstrated in Figure S2(a) and Figure S2(d), respectively [104-106]. Figure S2(c) and Figure S2(f) show the O 1*s* spectra for the Ag_3PO_4 and α-Ag_2WO_4 samples, respectively, and their components for lattice oxygen (≈ 530 eV), oxygen vacancies (≈ 531.5 eV) and hydroxyl-bounded groups on particle surface (≈ 533 eV) [107, 108].

The heterojunction with intermediate amount of α-Ag_2WO_4 (AWP 2) was investigated by XPS. The Ag 3*d* spectrum of sample AWP 2 is shown in Figure 5(a), where it is possible to see well-defined components of the spin-orbit coupling related to both Ag^+ and Ag^0 oxidation states. The contribution of the Ag^0 oxidation state arises from the presence of metallic Ag nanoparticles on the surface of Ag_3PO_4 and α-Ag_2WO_4 particles that results in Ag metal/semiconductor interface. The deconvolution analysis of the P 2*p* spectrum for AWP 2 indicates the presence of P^{5+} oxidation state (Figure 5(b)). The O 1*s* spectrum for AWP 2 together with its main components and the survey spectra for Ag_3PO_4, α-Ag_2WO_4 and AWP 2 are shown in Figure 5(c) and Figure 5(e), respectively. Variations in the broadening of the peaks

of W 4*f* spectrum for AWP 2 in relation to pure α-Ag_2WO_4 can be observed in Figure 5(d) by the broadening of the peaks. The deconvolution results indicated the presence of two oxidation states for W in this sample: W^{6+} in major proportion and W^{5+} in minor proportion. The presented components were attributed to the spin-orbit coupling of W^{6+} $4f_{7/2}$ (35.9 eV) and W^{6+} $4f_{5/2}$ (38.0 eV), W^{5+} $4f_{7/2}$ (35.0 eV) and W^{5+} $4f_{5/2}$ (37.2 eV) [109], and a shoulder related to the W^{6+} loss feature (41.2 eV).

Several works have reported the effects of heterojunction formation in the surface structure of the materials, such as interfacial strain [110-113]. The presence of W^{5+} in sample AWP 2 can be attributed to interfacial strain due to lattice mismatch between α-Ag_2WO_4 and Ag_3PO_4 since this latter was grown upon α-Ag_2WO_4 particles. Furthermore, the W^{6+} reduction can be assigned to the charge transfer effect between α-Ag_2WO_4 and Ag_3PO_4 caused by the effective formation of the heterojunction that leads to the energy level alignment [114].

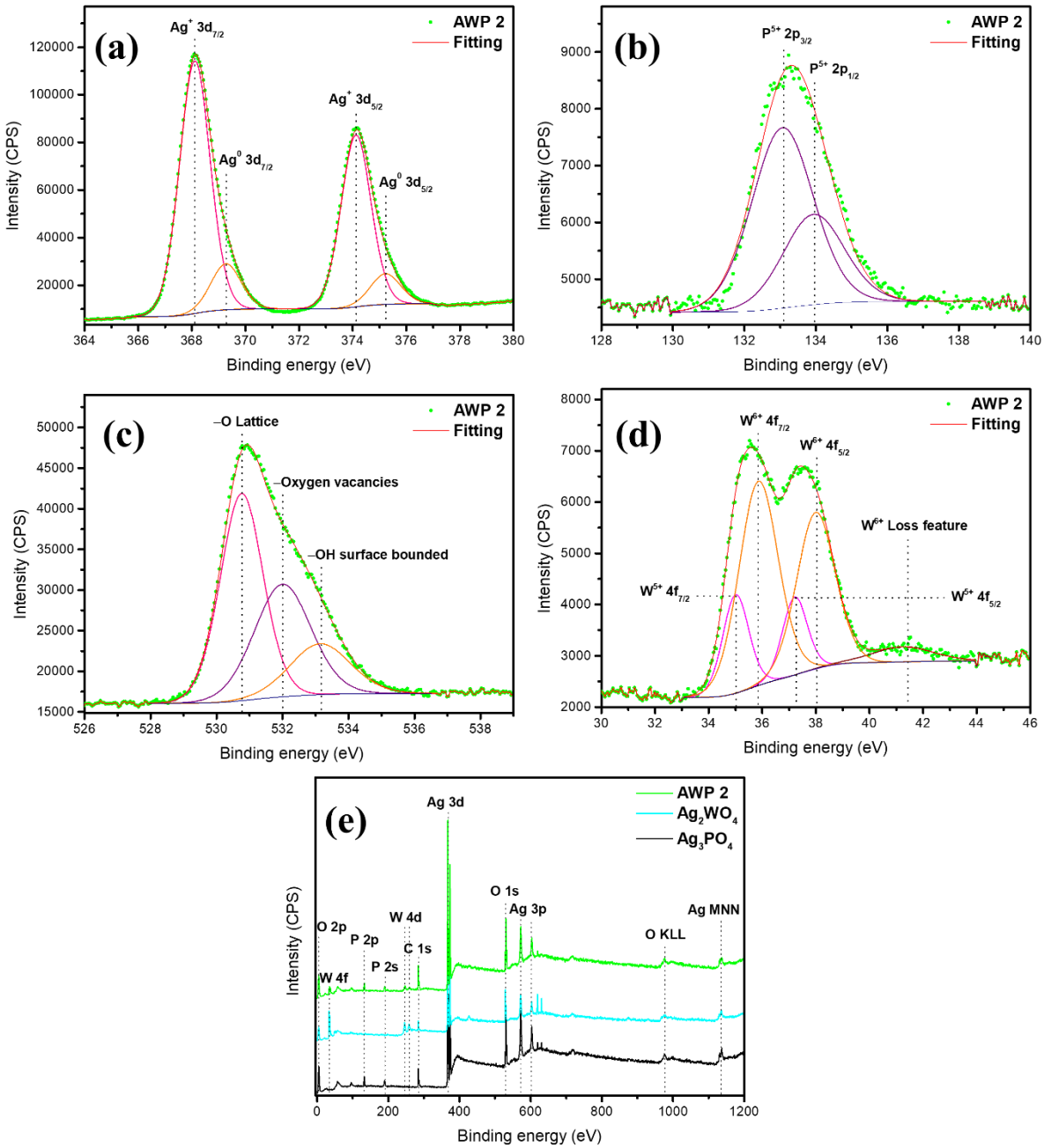

Figure 5. High-resolution XPS spectra of (a) Ag 3*d*, (b) P 2*p*, (c) O 1*s* and (d) W 4*f*, and (e) survey of AWP 2, α-Ag_2WO_4, and Ag_3PO_4.

It is well known that the photocatalytic activity of the photocatalysts is closely related to their light absorption ability. In this way, UV-vis diffuse reflectance spectroscopy was employed to determine the optical absorption properties of the pure Ag_3PO_4, α-Ag_2WO_4, and α-Ag_2WO_4/Ag_3PO_4 heterojunction. The results are represented in Figure 6. The Ag_3PO_4 and α-Ag_2WO_4 samples show an absorption edge in the visible region at 510 nm and 405 nm, respectively. It was observed in the heterojunction samples (AWP 1, AWP 2 and AWP 3) that

the spectra have two absorption edge wavelengths near these absorption edges, proving the presence of both materials, and therefore the successful formation of the heterojunction. It was also noted a slight redshift in the absorption edge at 405 nm referring to α-Ag_2WO_4, which favors the use of visible light in the photocatalytic process.

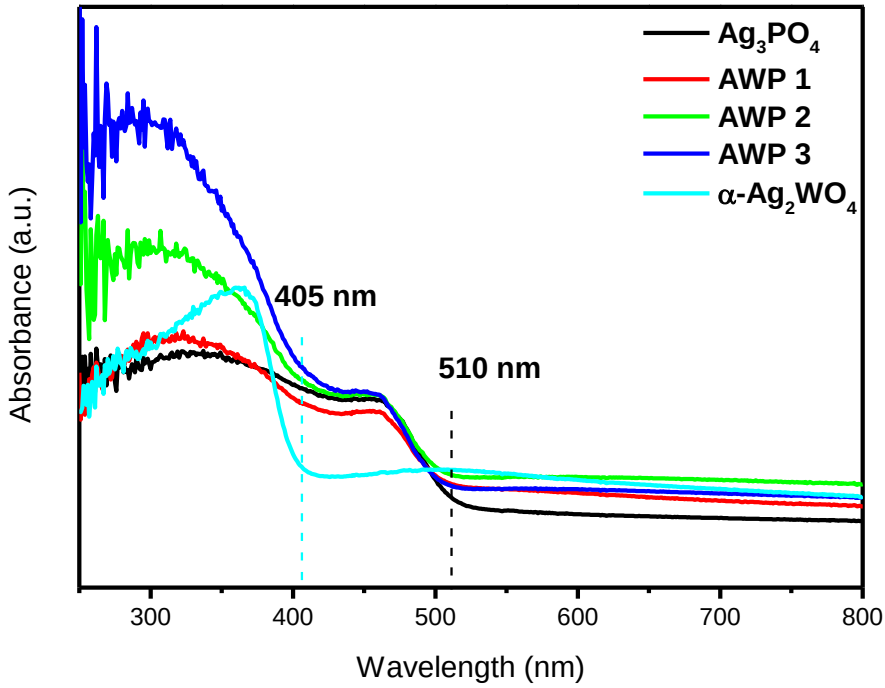

Figure 6. UV–vis diffuse reflectance spectra of Ag_3PO_4, AWP 1, AWP 2, AWP 3 and α-Ag_2WO_4.

The band gap energy (E_g) of the α-Ag_2WO_4 and Ag_3PO_4 samples (Figure S3) were calculated using the Tauc method, following Equation (1)[115]:

$$(\alpha h\nu)^{2/n} \sim h\nu - E_g, \quad (1)$$

where n = 1 for a semiconductor with direct band gap, n = 4 for a semiconductor with indirect band gap, α = absorbance, and $h\nu$ is photon energy. Ag_3PO_4 has an indirect band gap (n = 4) [116] with an experimental E_g value of 2.40 eV, as shown in Figure S3(a). The calculated E_g value is in agreement with those reported in the literature [117]. Figure S3(b) shows the experimental band gap of α-Ag_2WO_4, which has direct band gap (n = 1) [46] with a value of 3.12 eV. This experimental E_g value is also in well agreement with those reported in the literature [118].

The photoluminescence (PL) spectrum is usually employed to investigate the separation and transfer efficiency of the photogenerated (e^-—h^+) pairs during the photocatalytic process [119]. It is well known that the stronger PL intensity indicates the faster recombination speed of photogenerated charge carriers, implying that fewer photoinduced e^- and h^+ took part

in the photocatalytic oxidation and reduction reactions, resulting in lower photocatalytic activity [120]. Figure 7 exhibits the PL spectra of the as-prepared samples under the excitation wavelength of 325 nm. An analysis of the results renders that the PL spectrum of Ag_3PO_4 presents a broadband profile with the maximum emission intensity in the blue region of the visible electromagnetic spectrum at around 454 nm (2.731eV), which is in agreement with the previous results reported in the literature [95, 121]. This emission occurs mainly by the charge transfer (e^-─h^+) process between the different clusters that compose the material, such as [PO_4] tetrahedron clusters [95, 116, 122]. On the other hand, the α-Ag_2WO_4 sample showed a PL intensity peak also in the blue region centered at 456 nm (2.719eV), and another emission in the red region with a maximum emission intensity between 570 and 650 nm (about 1.984 eV). The blue emission peak is usually related to distorted [WO_6] octahedron, while the emission in the red region can be assigned to [AgO_y] clusters with y = 2, 4, 6 and 7, which arise from oxygen vacancies in the semiconductor [45, 123]. The heterojunction samples also showed emissions in the blue region at approximately 451 nm, which are close to the blue emission from the isolated materials. Particularly, samples AWP 1 and AWP 2 exhibited a broadband profile similar to Ag_3PO_4, while AWP 3 had a profile similar to α-Ag_2WO_4. This result could be associated with the fact that AWP 3 has a higher amount of α-Ag_2WO_4, resulting in a band profile similar to α-Ag_2WO_4. It can then be concluded that the PL results are consistent with the charge transfer processes of carriers between Ag_3PO_4 and α-Ag_2WO_4 semiconductors in the heterojunction.

According to the interfacial strain resulting from synergetic effects, it was possible to observe that the α-Ag_2WO_4 presented surface defects, such as a mix of W^{5+} and W^{6+} oxidation states (suggested by XPS experimental results), leading to a higher proportion of distorted [WO_6] clusters in the heterojunction. This caused the charge recombination related to these defects to increase, resulting in a higher emission in the blue region (around 454 nm) for samples AWP 1 and AWP 2, which showed higher PL intensities than the other samples. Additionally, the e^-─h^+ recombination rate in Ag_3PO_4 could be decreased, boosting its photocatalytic performance for oxidative reactions.

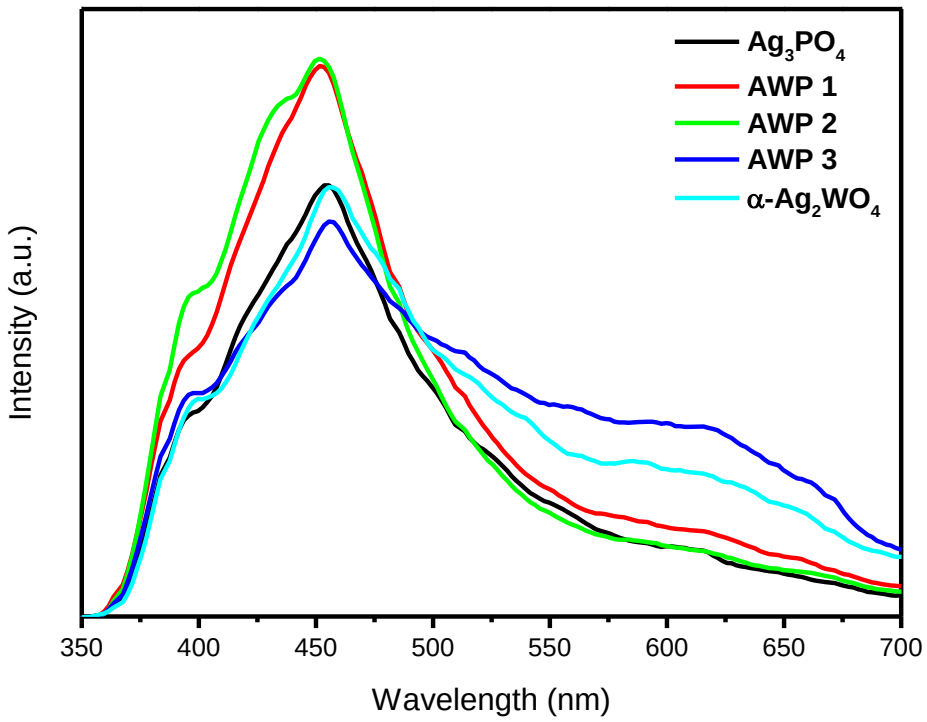

Figure 7. PL spectra of Ag_3PO_4, AWP 1, AWP 2, AWP 3 and α-Ag_2WO_4 at 300K.

3.2. Photocatalytic activity

The photocatalytic performance of α-Ag_2WO_4, Ag_3PO_4 and heterojunction samples AWP 1, AWP 2 and AWP 3 were investigated for the photodegradation of RhB dye under visible light irradiation. The degradation process was monitored by UV-vis absorption spectra at 554 nm, and the degradation curves are displayed in Figure 8. Tests on the RhB adsorption process of all samples were performed and the results are presented Figure S4. For this, after a period of 15 minutes in the ultrasound bath, the samples were under constant agitation (in the dark) for 30 minutes, with aliquots being removed every 10 minutes in order to evaluate the absorption profiles of the samples. An analysis of the results shows that the absorbance profiles are no dependent of the adsorption process. The Ag_3PO_4 sample showed a higher photocatalytic activity than α-Ag_2WO_4, degrading approximately 70% of the dye in 10 minutes of reaction, while for the latter no dye degradation was observed in the same reaction time. This low photocatalytic activity of α-Ag_2WO_4 can be attributed to the use of visible light since the material has a band gap energy that corresponds to excitation in the UV region (Figure S3(a)). As a consequence, e^- cannot be excited from the valence band (VB) to the conduction band (CB) [49]. Conversely, Ag_3PO_4 has a band gap energy that corresponds to excitation in the visible region, generating e^-—h^+ pairs under visible light irradiation, consequently degrading the dye. This makes Ag_3PO_4 a promising photocatalyst compared to α-Ag_2WO_4, as it has the

possibility of using sunlight irradiation for the degradation of organic compounds. The degradation curves for the heterojunction are also shown in Figure 8. It can be noted that all samples presented a photocatalytic activity superior to that of the isolated materials, demonstrating that the synergistic effect was effective for the formation of a heterojunction interface, responsible for the charge carrier transfer.

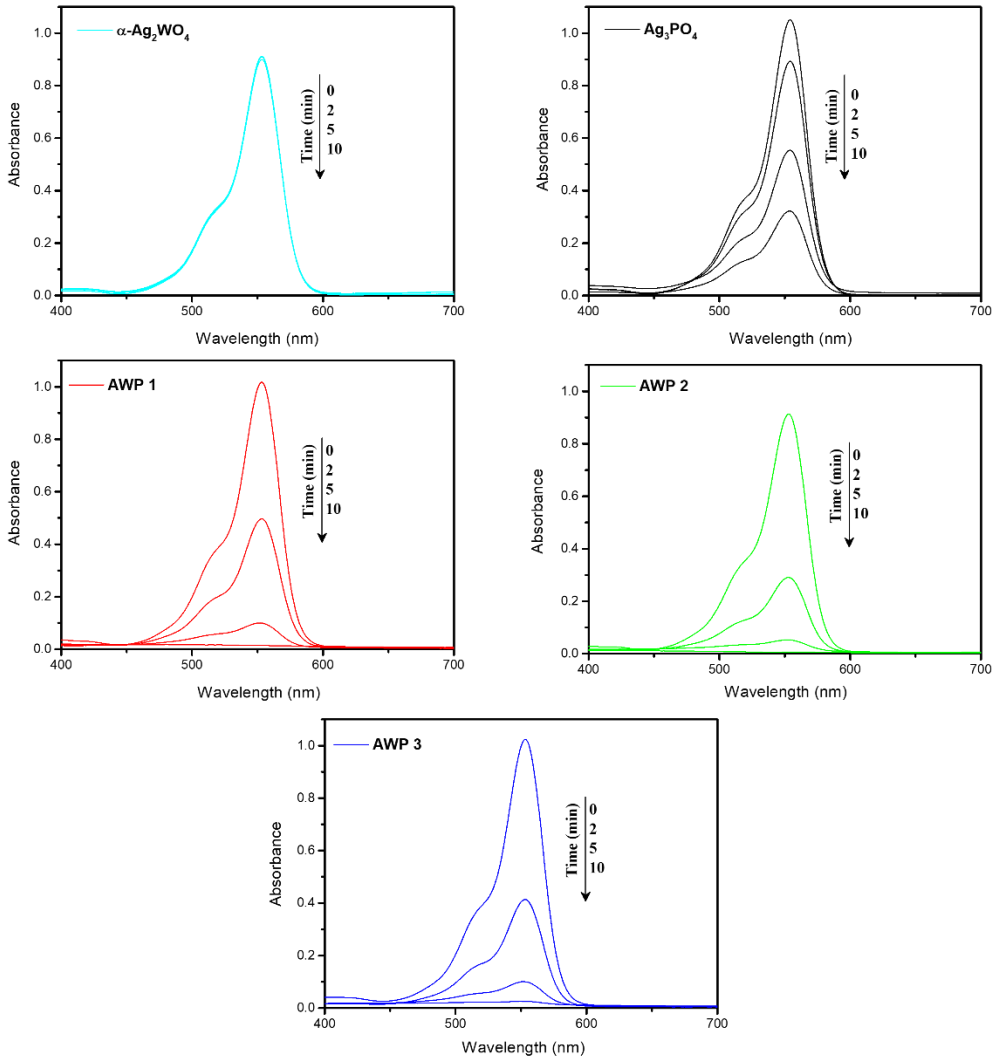

Figure 8. UV−vis absorbance plots for RhB photocatalytic degradation in the presence of 50 mg of each catalyst and 50 mL of RhB (10 mg L^{-1})

To investigate the kinetics of the RhB photodegradation reaction, the Langmuir-Hinshelwood model [50] was used, considering a pseudo-first order reaction, according to equation $-\ln (C_N / C_0) = kt$, where C_N and C_0 represent the RhB concentration at different time intervals and in the initial stage, respectively, and k and t represent the rate constant and irradiation time correspondingly, respectively. Figure 9(a) displays the variations in RhB concentration as C_N/C_0 *versus* irradiation time for the different samples. The photolysis

experiment performed is illustrated in Figure 8(a), where no degradation can be seen. Figure 9(b) shows the values found for the rate constants (k) using the Langmuir-Hinshelwood model abovementioned. It was observed that the heterojunction presented k values higher than those of isolated materials, especially sample AWP 2, which reached a value 4.13 times higher than that of Ag_3PO_4 and 458 times higher than of α-Ag_2WO_4, being the sample with the highest photocatalytic activity.

Note that the increased value of k in AWP 2 with respect to AWP 1 may have been due to the greater amount of α-Ag_2WO_4 inserted into the sample, which increased the synergistic effect between α-Ag_2WO_4 and Ag_3PO_4, enhancing the transfer of charge carriers and improving the photocatalytic activity of AWP 2. The value of k for AWP 3 possibly decreased in relation to AWP 2 as a result of the highest amount of α-Ag_2WO_4 contained in this sample in relation to the other heterojunction, thus requiring a higher proportion of UV light for the separation of the charge carriers, lowering its photocatalytic activity – which was still higher than that of isolated materials since the synergistic effect between the Ag_3PO_4 and α-Ag_2WO_4 samples prevailed. In addition, the excess of α-Ag_2WO_4 in sample AWP 3 caused a competition between the active sites and Ag_3PO_4 for the adsorption of species.

Table 1 shows the photocatalytic efficiency of the α-Ag_2WO_4/Ag_3PO_4 heterojunction synthesized in this work in comparison with other studies that used modified Ag_3PO_4 or the composite coupled to another material for RhB photodegradation. The data presented in Table 1 indicate that α-Ag_2WO_4/Ag_3PO_4 heterojunction in this work has a remarkably higher efficiency for RhB degradation, being the material with the highest rate constant among those reported there. Although Li et al. [124] synthesized an α-Ag_2WO_4/Ag_3PO_4 heterostructure for the photodegradation of bisphenol A, however without mentioning the presence of metallic silver in its heterostructure, this is the first time that the α-Ag_2WO_4/Ag_3PO_4 heterojunction in the presence of Ag NPs is studied for RhB photodegradation under visible light irradiation.

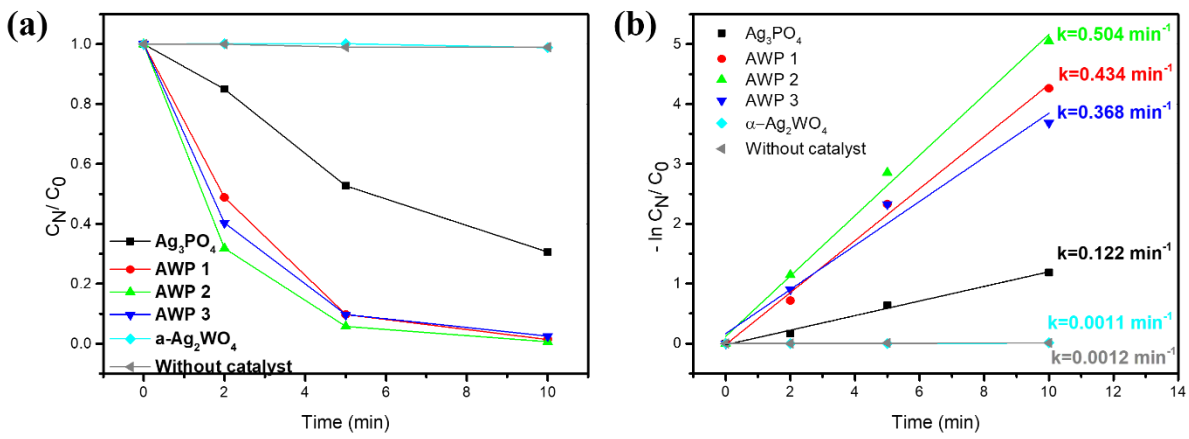

Figure 9. Photocatalytic degradation (a) and kinetic fit curves for all samples under visible-light irradiation (b).

Table 1

Comparison of photodegradation of RhB using visible light by materials containing Ag_3PO_4 with the reported literature.

Catalyst	Mass of catalyst (mg)	RhB concentration (mg/L)	Rate constant (min^{-1})	Time degradation (min)	Reference
Ag_3PO_4/N-TiO_2	20	10	0.019	120	[125]
g-C_3N_4@Ag@ Ag_3PO_4	6	20	0.030	60	[126]
Ag_2MoO_4 /Ag_3PO_4	50	10	0.359	12	[127]
Ag_3PO_4/NiO	30	5	0.224	30	[40]
Ag_3PO_4/$BiNbO_4$	15	20	0.146	30	[39]
Ag_3PO_4@$MgFe_2O_4$	20	10	0.1370	30	[128]
Ag_3PO_4:Mo	50	10	0.347	15	[34]
Ag_3PO_4:W	50	10	0.449	10	[129]
α-Ag_2WO_4/Ag_3PO_4	50	10	0.504	10	Our work

To evaluate the stability and reuse of the photocatalyst, recycling experiments were carried out under identical conditions using the sample with the highest photocatalytic activity (AWP 2). Figure 10 displays the five cycles performed for the RhB photodegradation. It can be noted that the first three cycles are relatively stable, with a catalyst deactivation of approximately 27% and 47% only in the fourth and fifth cycles, respectively. This decrease in the photocatalytic activity of AWP 2 may be related to the photocorrosion process that the sample is susceptible, which is a well-known phenomenon in Ag-based materials. To confirm the photocorrosion effect, the analysis of the XRD patterns of the AWP 2 sample was performed after the fifth cycle of the photocatalytic experiment and the results are presented in Figure S5. Note that the formation of a peak located at 2θ = 38.1°, which corresponds to the (111) diffraction plane of Ag^0 (JCPDS Card nº 89-3722). It is believed that the loss in photocatalytic activity after the third cycle is related to the increase in the production of Ag^0, since the excess of Ag^0 formed in the material decreases the light absorption, and then its performance.

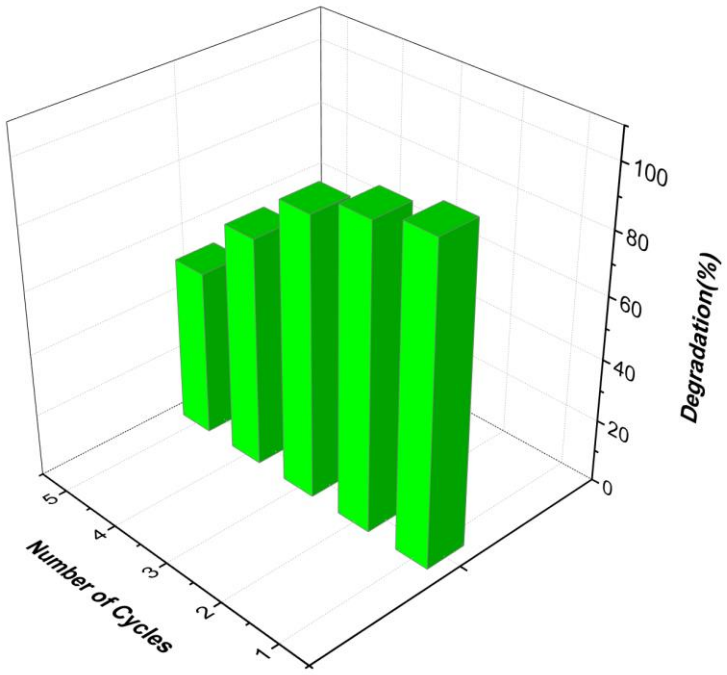

Figure 10. The RhB photodegradation cycles using 50 mg of AWP 2 sample and 50 mL of RhB (10 mg L^{-1}) under visible light irradiation.

In this study, trapping experiments were performed in sample AWP 2 to investigate the main reactive species (Figure 11). The scavenger experiments for $\bullet O_2^-$, •OH and h^+ were investigated by using the capture agents 1,4-benzoquinone (BQ), t-butyl alcohol (TBA)

and ammonium oxalate (AO), respectively [130]. Meanwhile, the RhB degradation process was inhibited by the addition of AO; however, when BQ was added, this process was moderately suppressed, i.e., the photocatalytic rate was reduced to 48%. Furthermore, no inhibition was detected when using TBA, indicating that •OH does not contribute to the degradation of RhB. These results demonstrate that h^+ and $•O_2^-$, in minor extent, are the main active species participating in the dye degradation ($h^+ > •O_2^- >> •OH$). At this point, it is important to mention that the possible mechanism for the degradation process is very dependent not only on the antioxidant capacity of scavengers, but also on the nature of the radical chain reaction. The chain reactions involving $•O_2^-$ radical participate in the degradation process, as occurred in the present case. The participation and generation of •OH along the degradation process does not rule, and the scavenging effect of BQ on $•O_2^-$ radical tends to inhibit the formation of •OH radicals. In this case, the catalytic reaction rate will be greatly reduced by adding either BQ or TBA.

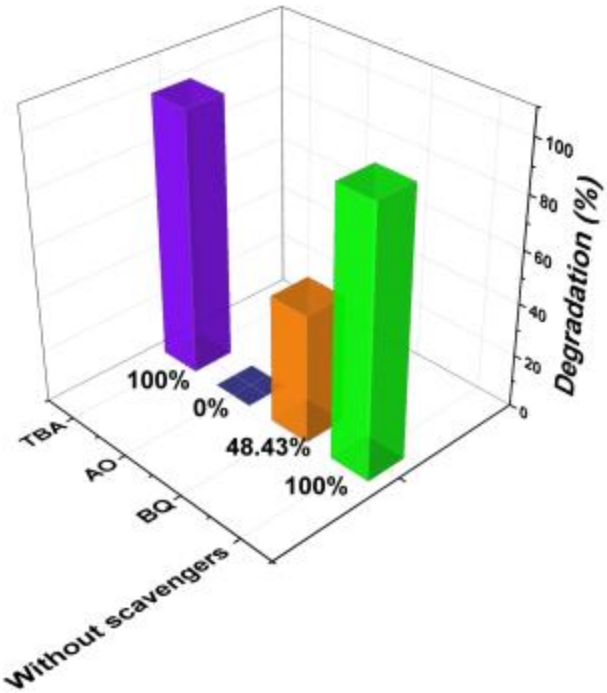

Figure 11. Effect of scavengers on the degradation efficiency.

3.3. Possible photocatalytic mechanism

It is known that the mechanism for photocatalytic degradation is closely related to the position of the conduction (CB) and valence (VB) bands of a semiconductor. Thus, to fully understand the photocatalytic reaction mechanism occurring during the photodegradation of the as-prepared α-Ag_2WO_4/Ag_3PO_4 heterojunction, the energy band edge positions of the VB and the CB of both α-Ag_2WO_4 and Ag_3PO_4 were calculated. The energy band diagram for the

heterojunction was constructed using Equations 2-3, which are based on the Mulliken's electronegativity, i.e., the geometric mean of the electronegativity of the constituent atoms in the material composition (Hill notation) [131, 132]:

$$E_{VB} = \chi - E_e + 0.5E_g \quad (2)$$

$$E_{CB} = E_{VB} - E_g, \quad (3)$$

where E_{VB} is the valence band potential, E_{CB} is the conduction band potential, E_e is the free electron energy on the hydrogen scale (~ 4.5 eV), E_g is the semiconductor band gap energy (Figure S3), and χ is the absolute electronegativity (Mulliken's electronegativity) of the semiconductor. For Ag_3PO_4, the value of χ is 5.96 eV [40], and for α-Ag_2WO_4 it is 6.00 eV [133]. Therefore, by employing Equations 2 and 3 the E_{VB} and E_{CB} values of 2.66 eV and 0.26 eV for Ag_3PO_4 and 3.06 eV and -0.06 eV for α-Ag_2WO_4, respectively, were obtained and are in agreement with those reported in the literature [134, 135].

Figure 12 illustrates two degradation mechanisms proposed for the α-Ag_2WO_4/Ag_3PO_4 heterojunction based on the obtained results. As shown in Figure 12 (a), under visible light irradiation both Ag_3PO_4 and α-Ag_2WO_4 are excited, generating e^-─h^+ pairs. Due to the energy position of the CB and the VB of each material, a type I heterojunction is formed, the photoexcited e^- in the CB of α-Ag_2WO_4 migrates to the CB of Ag_3PO_4, and the photogenerated h^+ in the VB of α-Ag_2WO_4 also migrates to the VB of Ag_3PO_4, thus generating an accumulation of charge carriers in Ag_3PO_4. In the VB of Ag_3PO_4, the h^+ that comes from α-Ag_2WO_4 and the photogenerated h^+ in the Ag_3PO_4 can directly degrade RhB [129, 136], as shown in Equation 4:

$$h^+ + RhB \rightarrow \text{degradation products} + CO_2 + H_2O \quad (4)$$

The as-mentioned reaction is in accordance with the observed scavenger results displayed in Figure 11, which indicate that h^+ is the main species acting in the RhB photodegradation.

As the CB of Ag_3PO_4 (0.26 eV) is more positive than the potential of $O_2/{\bullet}O_2^-$ ($E^0(O_2/{\bullet}O_2^-) = -0.046$ eV vs. NHE) [137], from a theoretical point of view it can be concluded that the photoexcited e^- on Ag_3PO_4 cannot react with dissolved O_2 in the reaction solution to yield ${\bullet}O_2^-$. However, this reaction between the accumulated e^- on the Ag_3PO_4 surface with the adsorbed O_2 to produce ${\bullet}O_2^-$ have been reported in several recent studies [40, 138, 139]. As seen in Figure 11, the ${\bullet}O_2^-$ species act, to a lesser degree, in the photodegradation of RhB, according to Equation 5:

$${\bullet}O_2^- + RhB \rightarrow \text{degradation products} + CO_2 + H_2O \quad (5)$$

As seen in the scavenger experiments (Figure 11), the •OH species do not participate in the degradation mechanism, and a possible explanation is that •OH would be rapidly self-consumed, forming H_2O and O_2 [34], according to Equation 6:

$$4\bullet OH \rightarrow 2H_2O + O_2 \quad (6)$$

As seen in XPS spectra results (Figure 5), the Ag NPs formed may be present at the interface of the two semiconductors and could contribute to the separation process of e^-—h^+ pairs due to the surface plasmon resonance (SPR) effect, which creates a cross-linking bridge for both semiconductors [66]. The surface plasmon excitations are generated under visible light irradiation and partially converted into energetic electrons on the surface of Ag NPs. Figure 12 (b) shows a proposed RhB degradation mechanism in the presence of Ag NPs, where it can be seen that the heterojunction remains type I and the same oxidizing species act. However, e^- photoexcited in α-Ag_2WO_4 can be transferred more quickly to Ag NPs. Thus, the e^- that are photoexcited to the CB of α-Ag_2WO_4 are able to migrate to the CB of Ag_3PO_4 more efficiently, as they use Ag NPs as a bridge. Therefore, the formation of metallic Ag NPs leads to an SPR effect, which is advantageous for the effective separation of charge carriers, resulting in improved photoactivity.

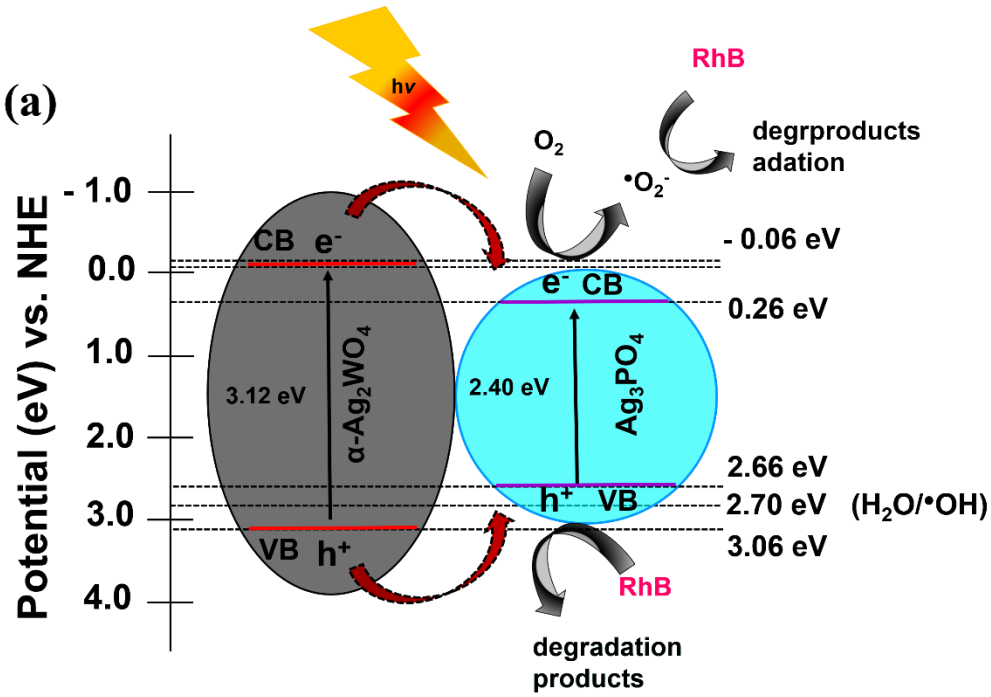

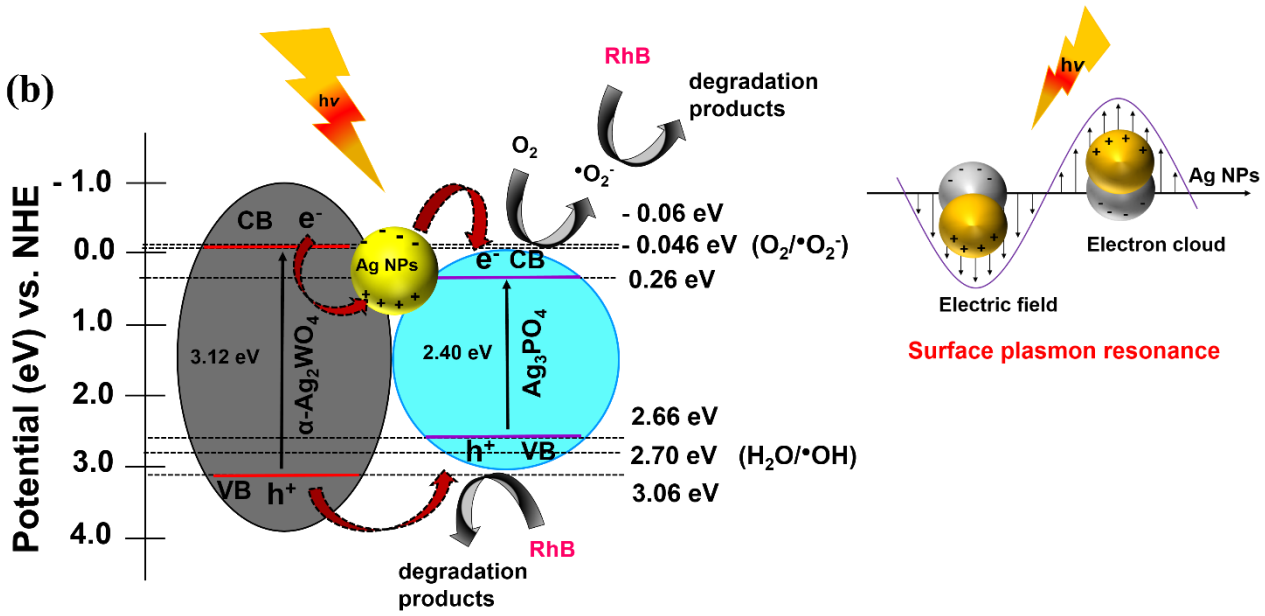

Figure 12. Possible photocatalytic mechanism diagram.

4. Conclusion

In conclusion, α-Ag_2WO_4/Ag_3PO_4 heterojunctions with different weight ratios of α-Ag_2WO_4 were fabricated by a facile chemical precipitation method. Under visible light irradiation, the as-prepared α-Ag_2WO_4/Ag_3PO_4 heterojunction displayed enhanced photocatalytic activity for the photocatalytic degradation of RhB. In particular, the sample with weight content of 24% of α-Ag_2WO_4 (named AWP 2) showed the highest photocatalytic performance for RhB photodegradation, degrading 94.3% in only 5 minutes of exposure to visible light, which is a very promising result when compared to pure Ag_3PO_4 and α-Ag_2WO_4 materials, which degraded 45 and 10%, respectively, under the same conditions. Our results demonstrate that this heterojunction can significantly enhance the absorption of visible light and successfully separate photogenerated electrons and holes after excitation. Such enhanced photocatalytic performance was explained by the surface plasmon resonance effect associated with the presence of metallic Ag at the metallic interface, as well as the formation of type I heterojunction, which served as a load transfer bridge, avoiding e^--h^+ recombination, and consequently improving the photocatalytic activity of the heterojunction since charge carriers are available to react with the adsorbed species for a longer time.

Acknowledgments

The authors acknowledge the financial support of the Brazilian research financing institutions: Fundação de Amparo à Pesquisa do Estado de São Paulo (FAPESP;

Grant Nos. 2013/07296-2, 19/23488-5, 2019/03722-3, and 2019/25944-8), Coordenação de Aperfeiçoamento de Pessoal de Nível Superior - Brasil (CAPES) - Finance Code 001 and Conselho Nacional de Desenvolvimento Científico e Tecnológico (CNPq, 142035/2017-3). J.A. acknowledges Universitat Jaume I (project UJI-B2019-30), and the Ministerio de Ciencia, Innovación y Universidades (Spain) (project PGC2018094417-B-I00) for financially supporting this research.

References

[1] J. Low, J. Yu, M. Jaroniec, S. Wageh, A.A. Al-Ghamdi, Heterojunction Photocatalysts, Adv Mater, 29 (2017) 1-20.

[2] C. Byrne, G. Subramanian, S.C. Pillai, Recent advances in photocatalysis for environmental applications, Journal of Environmental Chemical Engineering, 6 (2018) 3531-3555.

[3] X. Li, J. Li, J. Bai, Y. Dong, L. Li, B. Zhou, The Inhibition Effect of Tert-Butyl Alcohol on the TiO_2 Nano Assays Photoelectrocatalytic Degradation of Different Organics and Its Mechanism, Nanomicro Lett, 8 (2016) 221-231.

[4] Q.Z. Bocheng Qiu, Mengmeng Du, Linggang Fan, Mingyang Xing, Jinlong Zhang, Efficient Solar Light Harvesting CdS/Co_9S_8 Hollow Cubes for Z-Scheme Photocatalytic Water Splitting, Angew. Chem. Int. Ed, 56 (2017) 2684 –2688.

[5] Y. Bai, Y. Zhou, J. Zhang, X. Chen, Y. Zhang, J. Liu, J. Wang, F. Wang, C. Chen, C. Li, R. Li, C. Li, Homophase Junction for Promoting Spatial Charge Separation in Photocatalytic Water Splitting, ACS Catalysis, 9 (2019) 3242-3252.

[6] Q. Wang, M. Nakabayashi, T. Hisatomi, S. Sun, S. Akiyama, Z. Wang, Z. Pan, X. Xiao, T. Watanabe, T. Yamada, N. Shibata, T. Takata, K. Domen, Oxysulfide photocatalyst for visible-light-driven overall water splitting, Nature materials, 18 (2019) 827-832.

[7] Y. Wang, H. Suzuki, J. Xie, O. Tomita, D.J. Martin, M. Higashi, D. Kong, R. Abe, J. Tang, Mimicking Natural Photosynthesis: Solar to Renewable H_2 Fuel Synthesis by Z-Scheme Water Splitting Systems, Chem Rev, 118 (2018) 5201-5241.

[8] M.N. Mario Bartsch, The Role of Interfaces in Heterostructures, ChemPlusChem 2017, 82 (2017) 42–59.

[9] X. Lin, J. Hou, X. Guo, Y. Wang, J. Zheng, C. Liu, Y. Yang, G. Che, Heterostructured Ag_3PO_4 /Ag/Bi $_{3.64}Mo_{0.36}O_{6.55}$ nanospheres with enhanced photocatalytic activity under visible light irradiation, Separation and Purification Technology, 156 (2015) 875-880.

[10] F. Chen, Q. Yang, X. Li, G. Zeng, D. Wang, C. Niu, J. Zhao, H. An, T. Xie, Y. Deng, Hierarchical assembly of graphene-bridged Ag_3PO_4/Ag/$BiVO_4$ (040) Z-scheme photocatalyst:

An efficient, sustainable and heterogeneous catalyst with enhanced visible-light photoactivity towards tetracycline degradation under visible light irradiation, Applied Catalysis B: Environmental, 200 (2017) 330-342.

[11] Z. Wang, T. Hu, K. Dai, J. Zhang, C. Liang, Construction of Z-scheme Ag_3PO_4 /Bi_2WO_6 composite with excellent visible-light photodegradation activity for removal of organic contaminants, Chinese Journal of Catalysis, 38 (2017) 2021-2029.

[12] J. Lu, Y. Wang, F. Liu, L. Zhang, S. Chai, Fabrication of a direct Z-scheme type WO_3/Ag_3PO_4 composite photocatalyst with enhanced visible-light photocatalytic performances, Applied Surface Science, 393 (2017) 180-190.

[13] C. Ayappan, V. Jayaraman, B. Palanivel, A. Pandikumar, A. Mani, Facile preparation of novel Sb_2S_3 nanoparticles/rod-like α-Ag_2WO_4 heterojunction photocatalysts: Continuous modulation of band structure towards the efficient removal of organic contaminants, Separation and Purification Technology, 236 (2020) 116302.

[14] J.S. da Silva, T.R. Machado, A.B. Trench, A.D. Silva, V. Teodoro, P.C. Vieira, T.A. Martins, E. Longo, Enhanced photocatalytic and antifungal activity of hydroxyapatite/α-$AgVO_3$ composites, Materials Chemistry and Physics, 252 (2020) 123294.

[15] S. Rajamohan, V. Kumaravel, R. Muthuramalingam, S. Ayyadurai, A. Abdel-Wahab, B. Sub Kwak, M. Kang, S. Sreekantan, Fe_3O_4–Ag_2WO_4: facile synthesis, characterization and visible light assisted photocatalytic activity, New Journal of Chemistry, 41 (2017) 11722-11730.

[16] A. Hezam, J. Wang, Q.A. Drmosh, P. Karthik, M. Abdullah Bajiri, K. Namratha, M. Zare, T.R. Lakshmeesha, S. Shivanna, C. Cheng, B. Neppolian, K. Byrappa, Rational construction of plasmonic Z-scheme Ag-ZnO-CeO_2 heterostructures for highly enhanced solar photocatalytic H2 evolution, Applied Surface Science, 541 (2021) 148457.

[17] C. Ayappan, B. Palanivel, V. Jayaraman, T. Maiyalagan, A. Mani, One-step hydrothermal synthesis of $CaWO_4$/α-Ag_2WO_4 heterojunction: An efficient photocatalyst for removal of organic contaminants, Materials Science in Semiconductor Processing, 104 (2019) 104693.

[18] D. Sudha, P. Sivakumar, Review on the photocatalytic activity of various composite catalysts, Chemical Engineering and Processing: Process Intensification, 97 (2015) 112-133.

[19] E.K.K. Kar, Composite Materials Processing, Applications, Characterizations, Springer-Verlag Berlin, (2017).

[20] J. Ge, Y. Zhang, Y.-J. Heo, S.-J. Park, Advanced Design and Synthesis of Composite Photocatalysts for the Remediation of Wastewater: A Review, Catalysts, 9 (2019) 122.

[21] S. Bera, D.-I. Won, S.B. Rawal, H.J. Kang, W.I. Lee, Design of visible-light photocatalysts by coupling of inorganic semiconductors, Catalysis Today, 335 (2019) 3-19.

[22] B. Shao, X. Liu, Z. Liu, G. Zeng, Q. Liang, C. Liang, Y. Cheng, W. Zhang, Y. Liu, S. Gong, A novel double Z-scheme photocatalyst $Ag_3PO_4/Bi_2S_3/Bi_2O_3$ with enhanced visible-light photocatalytic performance for antibiotic degradation, Chemical Engineering Journal, 368 (2019) 730-745.

[23] Z. Liu, Y. Jiang, X. Liu, G. Zeng, B. Shao, Y. Liu, Y. Liu, W. Zhang, W. Zhang, M. Yan, X. He, Silver chromate modified sulfur doped graphitic carbon nitride microrod composites with enhanced visible-light photoactivity towards organic pollutants degradation, Composites Part B: Engineering, 173 (2019) 106918.

[24] T. Wu, X. Liu, Y. Liu, M. Cheng, Z. Liu, G. Zeng, B. Shao, Q. Liang, W. Zhang, Q. He, W. Zhang, Application of QD-MOF composites for photocatalysis: Energy production and environmental remediation, Coordination Chemistry Reviews, 403 (2020) 213097.

[25] S. Kumar, K. Ojha, A.K. Ganguli, Interfacial Charge Transfer in Photoelectrochemical Processes, Advanced Materials Interfaces, 4 (2017) 1600981.

[26] W. Hou, S.B. Cronin, A Review of Surface Plasmon Resonance-Enhanced Photocatalysis, Advanced Functional Materials, 23 (2013) 1612-1619.

[27] K. Ueno, H. Misawa, Surface plasmon-enhanced photochemical reactions, Journal of Photochemistry and Photobiology C: Photochemistry Reviews, 15 (2013) 31-52.

[28] X. Bai, R. Zong, C. Li, D. Liu, Y. Liu, Y. Zhu, Enhancement of visible photocatalytic activity via $Ag@C_3N_4$ core–shell plasmonic composite, Applied Catalysis B: Environmental, 147 (2014) 82-91.

[29] F.A. Sofi, K. Majid, O. Mehraj, The visible light driven copper based metal-organic-framework heterojunction:HKUST-1@Ag-Ag_3PO_4 for plasmon enhanced visible light photocatalysis, Journal of Alloys and Compounds, 737 (2018) 798-808.

[30] F.A. Sofi, K. Majid, Plasmon induced interfacial charge transfer across Zr-based metal-organic framework coupled Ag_2WO_4 heterojunction functionalized by Ag NPs: Efficient visible light photocatalyst, Chemical Physics Letters, 720 (2019) 7-14.

[31] J. Li, F. Liu, Y. Li, Fabrication of an Ag/Ag_2MoO_4 plasmonic photocatalyst with enhanced photocatalytic performance for the degradation of ciprofloxacin, New Journal of Chemistry, 42 (2018) 12054-12061.

[32] Y. Song, W. Xie, C. Yang, D. Wei, X. Su, L. Li, L. Wang, J. Wang, Humic acid-assisted synthesis of Ag/Ag_2MoO_4 and Ag/Ag_2WO_4 and their highly catalytic reduction of nitro- and azo-aromatics, Journal of Materials Research and Technology, 9 (2020) 5774-5783.

[33] Z. Xia, J. Min, S. Zhou, H. Ma, B. Zhang, X. Tang, Photocatalytic performance and antibacterial mechanism of Cu/Ag-molybdate powder material, Ceramics International, (2021).
[34] X. Zhou, G. Liu, J. Yu, W. Fan, Surface plasmon resonance-mediated photocatalysis by noble metal-based composites under visible light, Journal of Materials Chemistry, 22 (2012) 21337.
[35] G.M. Faccin, M.A. San-Miguel, J. Andres, E. Longo, E.Z. da Silva, Computational Modeling for the Ag Nanoparticle Coalescence Process: A Case of Surface Plasmon Resonance, The Journal of Physical Chemistry C, 121 (2017) 7030-7036.
[36] E.Z. da Silva, G.M. Faccin, T.R. Machado, N.G. Macedo, M. de Assis, S. Maya-Johnson, J.C. Sczancoski, J. Andrés, E. Longo, M.A. San-Miguel, Connecting Theory with Experiment to Understand the Sintering Processes of Ag Nanoparticles, The Journal of Physical Chemistry C, 123 (2019) 11310-11318.
[37] J. Andrés, A.F. Gouveia, L. Gracia, E. Longo, G. Manzeppi Faccin, E.Z. da Silva, D.H. Pereira, M.A. San-Miguel, Formation of Ag nanoparticles under electron beam irradiation: Atomistic origins from first-principles calculations, International Journal of Quantum Chemistry, 118 (2018) e25551.
[38] K. Nubla, N. Sandhyarani, Ag nanoparticles anchored Ag_2WO_4 nanorods: An efficient methanol tolerant and durable Pt free electro-catalyst toward oxygen reduction reaction, Electrochimica Acta, 340 (2020) 135942.
[39] A. Koyappayil, S. Berchmans, M.H. Lee, Dual enzyme-like properties of silver nanoparticles decorated Ag_2WO_4 nanorods and its application for H_2O_2 and glucose sensing, Colloids and surfaces. B, Biointerfaces, 189 (2020) 110840.
[40] M. Assis, E. Cordoncillo, R. Torres-Mendieta, H. Beltran-Mir, G. Minguez-Vega, R. Oliveira, E.R. Leite, C.C. Foggi, C.E. Vergani, E. Longo, J. Andres, Towards the scale-up of the formation of nanoparticles on alpha-Ag_2WO_4 with bactericidal properties by femtosecond laser irradiation, Scientific reports, 8 (2018) 1884.
[41] N.G. Macedo, T.R. Machado, R.A. Roca, M. Assis, C.C. Foggi, V. Puerto-Belda, G. Mínguez-Vega, A. Rodrigues, M.A. San-Miguel, E. Cordoncillo, H. Beltrán-Mir, J. Andrés, E. Longo, Tailoring the Bactericidal Activity of Ag Nanoparticles/α-Ag_2WO_4 Composite Induced by Electron Beam and Femtosecond Laser Irradiation: Integration of Experiment and Computational Modeling, ACS Applied Bio Materials, 2 (2019) 824-837.
[42] P.S.S. Lemos, G. S; Roca, R. A; Assis, M.; Torres-Mendieta, R.; Beltrán-Mir, H.; Mínguez-, G.C. Vega, E.; Andrés, J.; and Longo, E., Laser and electron beam-induced formation of Ag/Cr structures on Ag_2CrO_4, Phys. Chem. Chem. Phys., 21 (2019) 6101-6111.

[43] C.-G.N. Hai Guo, Lei Zhang, Xiao-Ju Wen, Chao Liang, Xue-Gang Zhang, Dan-Lin Guan, Ning Tang, and Guangming Zeng, Construction of Direct Z-Scheme AgI/$Bi_2Sn_2O_7$ Nanojunction System with Enhanced Photocatalytic Activity: Accelerated Interfacial Charge Transfer Induced Efficient Cr(VI) Reduction, Tetracycline Degradation and Escherichia coli Inactivation. , ACS Sustainable Chemistry & Engineering, 6 (2018) 8003–8018.

[44] D. Liu, W. Huang, L. Li, L. Liu, X. Sun, B. Liu, B. Yang, C. Guo, Experimental and theoretical investigation on photocatalytic activities of 1D Ag/Ag_2WO_4 nanostructures, Nanotechnology, 28 (2017) 385702.

[45] J. Paulo de Campos da Costa, M. Assis, V. Teodoro, A. Rodrigues, C. Cristina de Foggi, M.A. San-Miguel, J.P. Pereira do Carmo, J. Andrés, E. Longo, Electron beam irradiation for the formation of thick Ag film on Ag_3PO_4, RSC Advances, 10 (2020) 21745-21753.

[46] G. Botelho, J.C. Sczancoski, J. Andres, L. Gracia, E. Longo, Experimental and Theoretical Study on the Structure, Optical Properties, and Growth of Metallic Silver Nanostructures in Ag_3PO_4, The Journal of Physical Chemistry C, 119 (2015) 6293-6306.

[47] T. Yan, W. Guan, Y. Xiao, J. Tian, Z. Qiao, H. Zhai, W. Li, J. You, Effect of thermal annealing on the microstructures and photocatalytic performance of silver orthophosphate: The synergistic mechanism of Ag vacancies and metallic Ag, Applied Surface Science, 391 (2017) 592-600.

[48] Z. Liu, Y. Liu, P. Xu, Z. Ma, J. Wang, H. Yuan, Rational Design of Wide Spectral-Responsive Heterostructures of Au Nanorod Coupled Ag_3PO_4 with Enhanced Photocatalytic Performance, ACS applied materials & interfaces, 9 (2017) 20620-20629.

[49] S. Linic, P. Christopher, D.B. Ingram, Plasmonic-metal nanostructures for efficient conversion of solar to chemical energy, Nature materials, 10 (2011) 911-921.

[50] A.B. Trench, T.R. Machado, A.F. Gouveia, M. Assis, L.G. da Trindade, C. Santos, A. Perrin, C. Perrin, M. Oliva, J. Andrés, E. Longo, Connecting structural, optical, and electronic properties and photocatalytic activity of Ag_3PO_4:Mo complemented by DFT calculations, Applied Catalysis B: Environmental, 238 (2018) 198-211.

[51] A.F.G. Roman Alvarez-Roca, Camila Cristina de Foggi, Pablo Santana Lemos, Lourdes Gracia, Luís Fernando da Silva, Carlos Eduardo Vergani, Miguel San-Miguel, Elson Longo, and Juan Andrés, Selective Synthesis of α-, β-, and γ-Ag_2WO_4 Polymorphs: Promising Platforms for Photocatalytic and Antibacterial Materials, Inorg. Chem, 60 (2021) 1062−1079.

[52] T. R. Masse, I., Durif, A., Refinement of Crystal-Structure of Silver Monophosphate, Ag_3PO_4-Existence of High-Temperature Form, Zeitschrift Fur Kristallographie, 144 (1976) 76-81.

[53] S.G. P.M. Skarstad, $(W_4O_{16})^{8-}$ POLYION IN THE HIGH TEMPERATURE MODIFICATION OF SILVER TUNGSTATE, Mat. Res. Bull., 10 (1975) 791-800,.

[54] T. Cai, W. Zeng, Y. Liu, L. Wang, W. Dong, H. Chen, X. Xia, A promising inorganic-organic Z-scheme photocatalyst Ag_3PO_4/PDI supermolecule with enhanced photoactivity and photostability for environmental remediation, Applied Catalysis B: Environmental, 263 (2020) 118327.

[55] J. Huang, D. Li, Y. Liu, R. Li, P. Chen, H. Liu, W. Lv, G. Liu, Y. Feng, Ultrathin Ag_2WO_4-coated P-doped g-C_3N_4 nanosheets with remarkable photocatalytic performance for indomethacin degradation, Journal of hazardous materials, 392 (2020) 122355.

[56] G.W. Hao Zhang, Da Chen, Xiaojun Lv, and Jinghong Li, Tuning Photoelectrochemical Performances of Ag-TiO_2 Nanocomposites via Reduction/Oxidation of Ag, Chem. Mater. , 20 (2008) 6543–6549.

[57] Y. Liu, L. Fang, H. Lu, Y. Li, C. Hu, H. Yu, One-pot pyridine-assisted synthesis of visible-light-driven photocatalyst Ag/Ag_3PO_4, Applied Catalysis B: Environmental, 115-116 (2012) 245-252.

[58] C. Zhang, K. Yu, Y. Feng, Y. Chang, T. Yang, Y. Xuan, D. Lei, L.-L. Lou, S. Liu, Novel 3DOM-$SrTiO_3$/Ag/Ag_3PO_4 ternary Z-scheme photocatalysts with remarkably improved activity and durability for contaminant degradation, Applied Catalysis B: Environmental, 210 (2017) 77-87.

[59] D.H. Yoon, Y.J. Tak, S.P. Park, J. Jung, H. Lee, H.J. Kim, Simultaneous engineering of the interface and bulk layer of Al/sol-NiOx/Si structured resistive random access memory devices, J. Mater. Chem. C, 2 (2014) 6148-6154.

[60] B. Sasi, K.G. Gopchandran, Nanostructured mesoporous nickel oxide thin films, Nanotechnology, 18 (2007) 115613.

[61] P. Castillero, V. Rico-Gavira, C. López-Santos, A. Barranco, V. Pérez-Dieste, C. Escudero, J.P. Espinós, A.R. González-Elipe, Formation of Subsurface W^{5+} Species in Gasochromic Pt/WO_3 Thin Films Exposed to Hydrogen, The Journal of Physical Chemistry C, 121 (2017) 15719-15727.

[62] S. Koohfar, A.B. Georgescu, I. Hallsteinsen, R. Sachan, M.A. Roldan, E. Arenholz, D.P. Kumah, Effect of strain on magnetic and orbital ordering of $LaSrCrO_3$/$LaSrMnO_3$ heterostructures, Physical Review B, 101 (2020).

[63] Z. Wu, X. Chen, E. Mu, Y. Liu, Z. Che, C. Dun, F. Sun, X. Wang, Y. Zhang, Z. Hu, Lattice Strain Enhances Thermoelectric Properties in Sb_2Te_3/Te Heterostructure, Advanced Electronic Materials, 6 (2019) 1900735.

[64] Y. Tian, Q. Zheng, J. Zhao, Tensile Strain-Controlled Photogenerated Carrier Dynamics at the van der Waals Heterostructure Interface, The Journal of Physical Chemistry Letters, 11 (2020) 586-590.

[65] P. Jiang, M.-C. Record, P. Boulet, First-principles calculations on $CuInSe_2$/AlP heterostructures, Journal of Materials Chemistry C, 8 (2020) 4732-4742.

[66] H.T. Kung, P. Li, J.J. Lee, Y. Zhao, A. Dumont, Z.H. Lu, Reaction and Energy Levels at Oxide–Oxide Heterojunction Interfaces, Advanced Materials Interfaces, 6 (2019) 1901456.

[67] D.L. Wood, J. Tauc, Weak Absorption Tails in Amorphous Semiconductors, Physical Review B, 5 (1972) 3144-3151.

[68] G. Botelho, J. Andres, L. Gracia, L.S. Matos, E. Longo, Photoluminescence and Photocatalytic Properties of Ag_3PO_4 Microcrystals: An Experimental and Theoretical Investigation, ChemPlusChem, 81 (2016) 202-212.

[69] M. Ge, Z. Li, Recent progress in Ag_3PO_4 -based all-solid-state Z-scheme photocatalytic systems, Chinese Journal of Catalysis, 38 (2017) 1794-1803.

[70] F.X. Nobre, I.S. Bastos, R.O. Dos Santos Fontenelle, E.A.A. Junior, M.L. Takeno, L. Manzato, J.M.E. de Matos, P.P. Orlandi, J. de Fatima Souza Mendes, W.R. Brito, P.R. da Costa Couceiro, Antimicrobial properties of alpha-Ag_2WO_4 rod-like microcrystals synthesized by sonochemistry and sonochemistry followed by hydrothermal conventional method, Ultrasonics sonochemistry, 58 (2019) 104620.

[71] J. Lv, K. Dai, J. Zhang, L. Lu, C. Liang, L. Geng, Z. Wang, G. Yuan, G. Zhu, In situ controllable synthesis of novel surface plasmon resonance-enhanced Ag_2WO_4 /Ag/Bi_2MoO_6 composite for enhanced and stable visible light photocatalyst, Applied Surface Science, 391 (2017) 507-515.

[72] T. Simon, N. Bouchonville, M.J. Berr, A. Vaneski, A. Adrovic, D. Volbers, R. Wyrwich, M. Doblinger, A.S. Susha, A.L. Rogach, F. Jackel, J.K. Stolarczyk, J. Feldmann, Redox shuttle mechanism enhances photocatalytic H_2 generation on Ni-decorated CdS nanorods, Nature materials, 13 (2014) 1013-1018.

[73] L. Wang, J. Ding, Y. Chai, Q. Liu, J. Ren, X. Liu, W.L. Dai, CeO_2 nanorod/g-C_3N_4/N-rGO composite: enhanced visible-light-driven photocatalytic performance and the role of N-rGO as electronic transfer media, Dalton transactions, 44 (2015) 11223-11234.

[74] C. Tang, E. Liu, J. Wan, X. Hu, J. Fan, Co_3O_4 nanoparticles decorated Ag_3PO_4 tetrapods as an efficient visible-light-driven heterojunction photocatalyst, Applied Catalysis B: Environmental, 181 (2016) 707-715.

[75] A. Phuruangrat, N. Ekthammathat, S. Thongtem, T. Thongtem, Preparation of $LaPO_4$ nanowires with high aspect ratio by a facile hydrothermal method and their photoluminescence, Research on Chemical Intermediates, 39 (2012) 1363-1371.

[76] P.F.S. Pereira, C.C. Santos, A.F. Gouveia, M.M. Ferrer, I.M. Pinatti, G. Botelho, J.R. Sambrano, I.L.V. Rosa, J. Andrés, E. Longo, α-$Ag_{2-2x}Zn_xWO_4$ ($0 \leq x \leq 0.25$) Solid Solutions: Structure, Morphology, and Optical Properties, Inorganic Chemistry, 56 (2017) 7360-7372.

[77] E. Longo, D.P. Volanti, V.M. Longo, L. Gracia, I.C. Nogueira, M.A.P. Almeida, A.N. Pinheiro, M.M. Ferrer, L.S. Cavalcante, J. Andrés, Toward an Understanding of the Growth of Ag Filaments on α-Ag_2WO_4 and Their Photoluminescent Properties: A Combined Experimental and Theoretical Study, The Journal of Physical Chemistry C, 118 (2014) 1229-1239.

[78] R.A. Roca, J.C. Sczancoski, I.C. Nogueira, M.T. Fabbro, H.C. Alves, L. Gracia, L.P.S. Santos, C.P. de Sousa, J. Andrés, G.E. Luz, E. Longo, L.S. Cavalcante, Facet-dependent photocatalytic and antibacterial properties of α-Ag_2WO_4 crystals: combining experimental data and theoretical insights, Catalysis Science & Technology, 5 (2015) 4091-4107.

[79] T. Li, H. Wei, H. Jia, T. Xia, X. Guo, T. Wang, L. Zhu, Mechanisms for Highly Efficient Mineralization of Bisphenol A by Heterostructured Ag_2WO_4/Ag_3PO_4 under Simulated Solar Light, ACS Sustainable Chemistry & Engineering, 7 (2019) 4177-4185.

[80] N.R. Khalid, U. Mazia, M.B. Tahir, N.A. Niaz, M.A. Javid, Photocatalytic degradation of RhB from an aqueous solution using Ag_3PO_4/N-TiO_2 heterostructure, Journal of Molecular Liquids, 313 (2020) 113522.

[81] X. Li, T. Wan, J. Qiu, H. Wei, F. Qin, Y. Wang, Y. Liao, Z. Huang, X. Tan, In-situ photocalorimetry-fluorescence spectroscopy studies of RhB photocatalysis over Z-scheme g-C_3N_4@Ag@Ag_3PO_4 nanocomposites: A pseudo-zero-order rather than a first-order process, Applied Catalysis B: Environmental, 217 (2017) 591-602.

[82] W. Cao, Y. An, L. Chen, Z. Qi, Visible-light-driven Ag_2MoO_4/Ag_3PO_4 composites with enhanced photocatalytic activity, Journal of Alloys and Compounds, 701 (2017) 350-357.

[83] R.K. Santos, T.A. Martins, G.N. Silva, M.V.S. Conceicao, I.C. Nogueira, E. Longo, G. Botelho, Ag_3PO_4/NiO Composites with Enhanced Photocatalytic Activity under Visible Light, ACS omega, 5 (2020) 21651-21661.

[84] N. Li, S. Miao, X. Zheng, J. Lai, S. Lv, X. Gu, M. Zhang, J. Yang, S. Cui, Construction of $Ag_3PO_4/BiNbO_4$ heterojunction photocatalysts with high activity for Rhodamine B removal under simulated sunlight irradiation, Ceramics International, 45 (2019) 24260-24268.

[85] T. Zhou, G. Zhang, P. Ma, X. Qiu, H. Zhang, H. Yang, G. Liu, Efficient degradation of rhodamine B with magnetically separable Ag_3PO_4@$MgFe_2O_4$ composites under visible irradiation, Journal of Alloys and Compounds, 735 (2018) 1277-1290.

[86] A.B. Trench, T.R. Machado, A.F. Gouveia, C.C. Foggi, V. Teodoro, I. Sánchez-Montes, M.M. Teixeira, L.G. da Trindade, N. Jacomaci, A. Perrin, C. Perrin, J.M. Aquino, J. Andrés, E. Longo, Rational Design of W-Doped Ag_3PO_4 as an Efficient Antibacterial Agent and Photocatalyst for Organic Pollutant Degradation, ACS omega, 5 (2020) 23808-23821.

[87] S. Li, S. Hu, W. Jiang, Y. Liu, J. Liu, Z. Wang, Facile synthesis of flower-like Ag_3VO_4/Bi_2WO_6 heterojunction with enhanced visible-light photocatalytic activity, Journal of colloid and interface science, 501 (2017) 156-163.

[88] M. Sun, R. Senthil, J. Pan, S. Osman, A. Khan, A Facile Synthesis of Visible-Light Driven Rod-on-Rod like α-FeOOH/α-$AgVO_3$ Nanocomposite as Greatly Enhanced Photocatalyst for Degradation of Rhodamine B, Catalysts, 8 (2018) 392.

[89] S.K. Ray, D. Dhakal, S.W. Lee, Rapid degradation of naproxen by AgBr-α-$NiMoO_4$ composite photocatalyst in visible light: Mechanism and pathways, Chemical Engineering Journal, 347 (2018) 836-848.

[90] H. Xu, Y. Cao, J. Xie, J. Hu, Y. Li, D. Jia, A construction of Ag-modified raspberry-like $AgCl/Ag_2WO_4$ with excellent visible-light photocatalytic property and stability, Materials Research Bulletin, 102 (2018) 342-352.

[91] H. Li, Y. Zhang, Q. Zhang, Y. Wang, Y. Fan, X. Gao, J. Niu, Boosting visible-light photocatalytic degradation of indomethacin by an efficient and photostable Ag_3PO_4/NG/WO_3 composites, Applied Surface Science, 490 (2019) 481-491.

[92] U. Rafiq, O. Mehraj, S. Lone, M. Wahid, K. Majid, Solvothermal synthesis of Ag_2WO_4/Sb_2WO_6 heterostructures for enhanced charge transfer properties and efficient visible-light-driven photocatalytic activity and stability, Journal of Environmental Chemical Engineering, 8 (2020) 104301.

[93] Y. Sang, X. Cao, G. Dai, L. Wang, Y. Peng, B. Geng, Facile one-pot synthesis of novel hierarchical Bi_2O_3/Bi_2S_3 nanoflower photocatalyst with intrinsic p-n junction for efficient photocatalytic removals of RhB and Cr(VI), Journal of hazardous materials, 381 (2020) 120942.

[94] W. Shi, F. Guo, S. Yuan, In situ synthesis of Z-scheme Ag_3PO_4 /$CuBi_2O_4$ photocatalysts and enhanced photocatalytic performance for the degradation of tetracycline under visible light irradiation, Applied Catalysis B: Environmental, 209 (2017) 720-728.

[95] X. Yang, H. Tang, J. Xu, M. Antonietti, M. Shalom, Silver phosphate/graphitic carbon nitride as an efficient photocatalytic tandem system for oxygen evolution, ChemSusChem, 8 (2015) 1350-1358.

[96] E. Abroshan, S. Farhadi, A. Zabardasti, Novel magnetically separable $Ag_3PO_4/MnFe_2O_4$ nanocomposite and its high photocatalytic degradation performance for organic dyes under solar-light irradiation, Solar Energy Materials and Solar Cells, 178 (2018) 154-163.

Supplementary Information

Interface matters: Design of an efficient α-Ag_2WO_4/Ag_3PO_4 photocatalyst

Aline B. Trench [a], Roman Alvarez [a], Vinícius Teodoro [a], Letícia G. da Trindade[b] , Thales R. Machado [a], Mayara M. Teixeira [a], Daniele de Souza [c], Ivo M. Pinatti [d], Alexandre Z. Simões [d], Yara Galvão Gobato [c], Juan Andrés [e], Elson Longo [a,*]

[a] *CDMF – Department of Chemistry, Federal University of São Carlos, 13565-905, São Carlos, SP, Brazil*

[b] *Department of Chemistry, São Paulo State University, 17033-360, Bauru, SP, Brazil*

[c] *Department of Physics – Federal University of São Carlos, 13565-905, São Carlos, SP, Brazil*

[d] *Faculty of Engineering of Guaratinguetá, São Paulo State University (UNESP), 12516-410, Guaratinguetá, SP, Brazil*

[e] *Department of Analytical and Physical Chemistry, University Jaume I, 12071, Castellón, Spain*

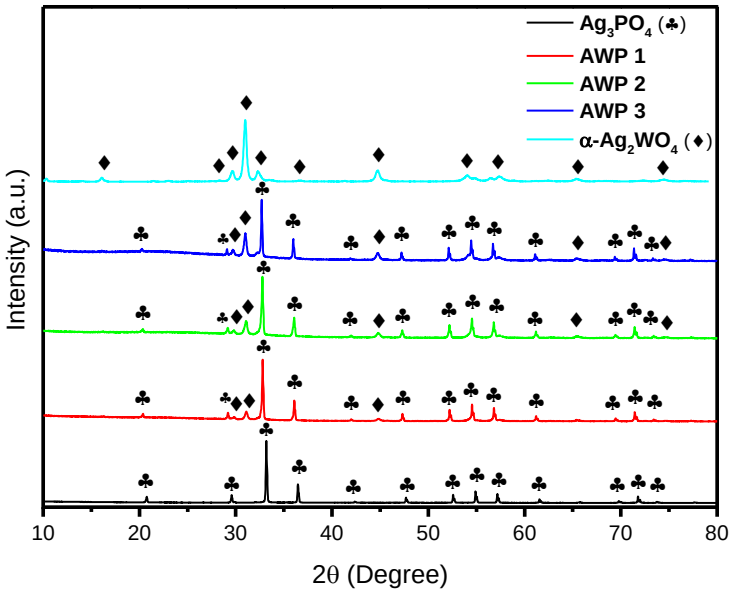

Figure S1. XRD patterns of Ag_3PO_4, AWP 1, AWP 2, AWP 3, and α-Ag_2WO_4

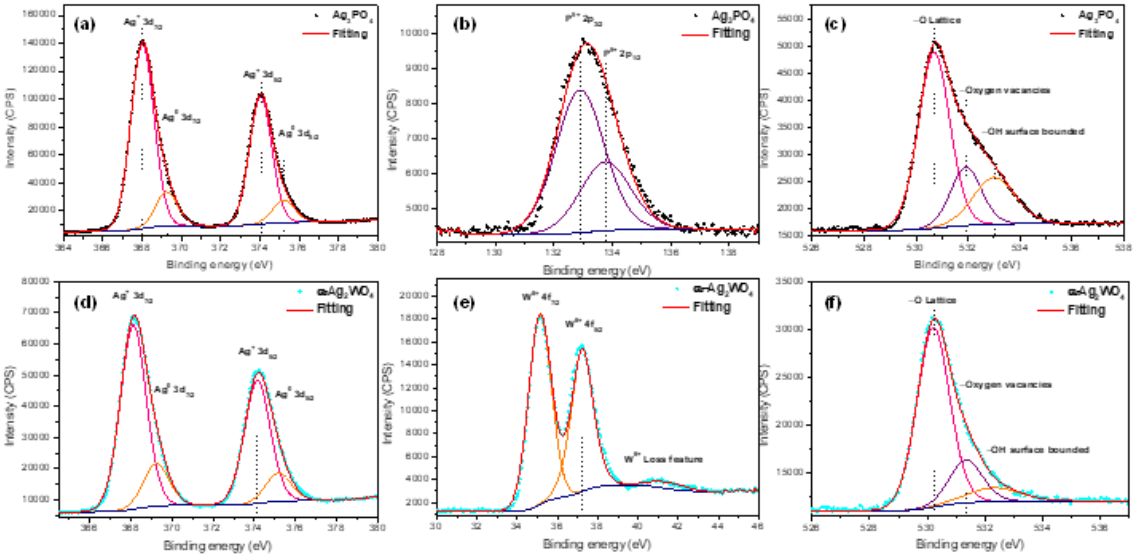

Figure S2. High-resolution XPS spectra of (a) Ag 3*d*, (b) P 2*p* and (c) O 1*s* of Ag_3PO_4 sample, and (d) Ag 3*d*, (e) W 4*f* and (f) O 1*s* of α-Ag_2WO_4 sample.

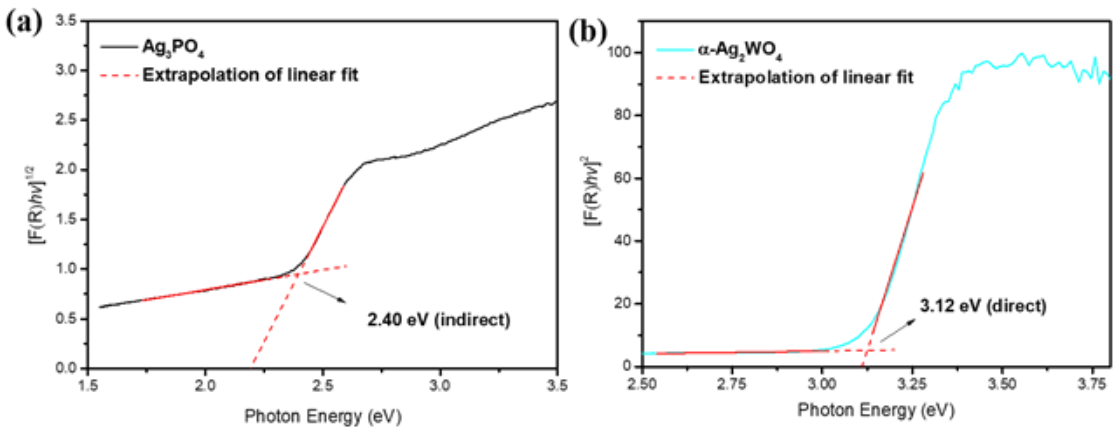

Figure S3. Tauc plot for (a) Ag_3PO_4 and (b) α-Ag_2WO_4 samples.

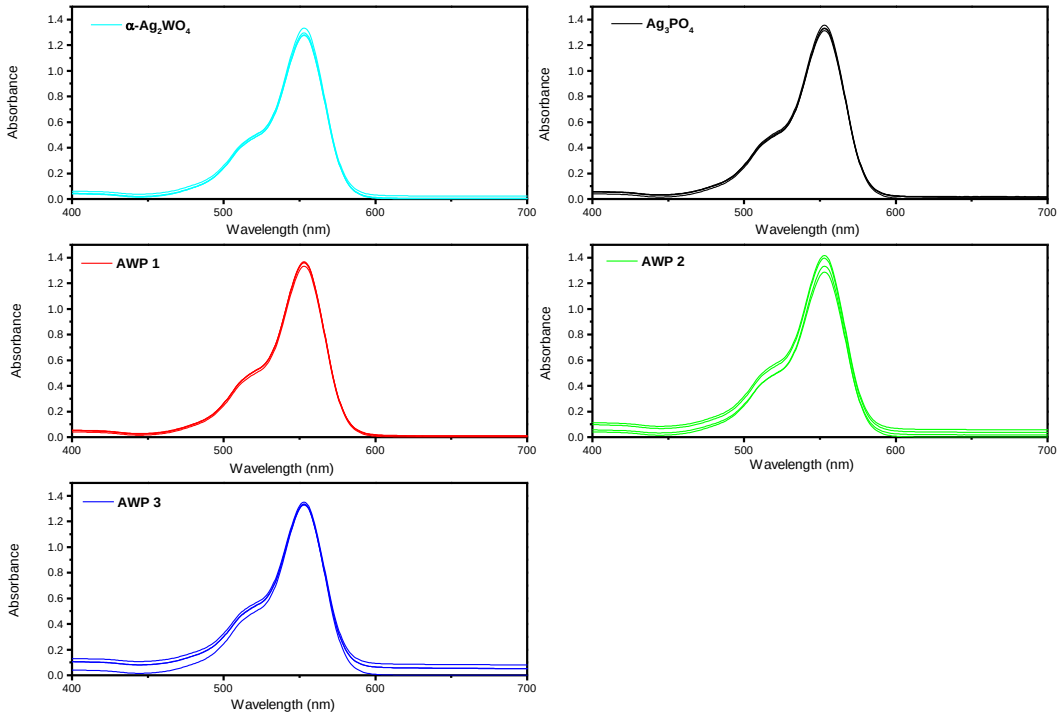

Figure S4. Absorbance profile vs wavelength of α-Ag_2WO_4, Ag_3PO_4, AWP 1, AWP 2, and AWP 3 samples

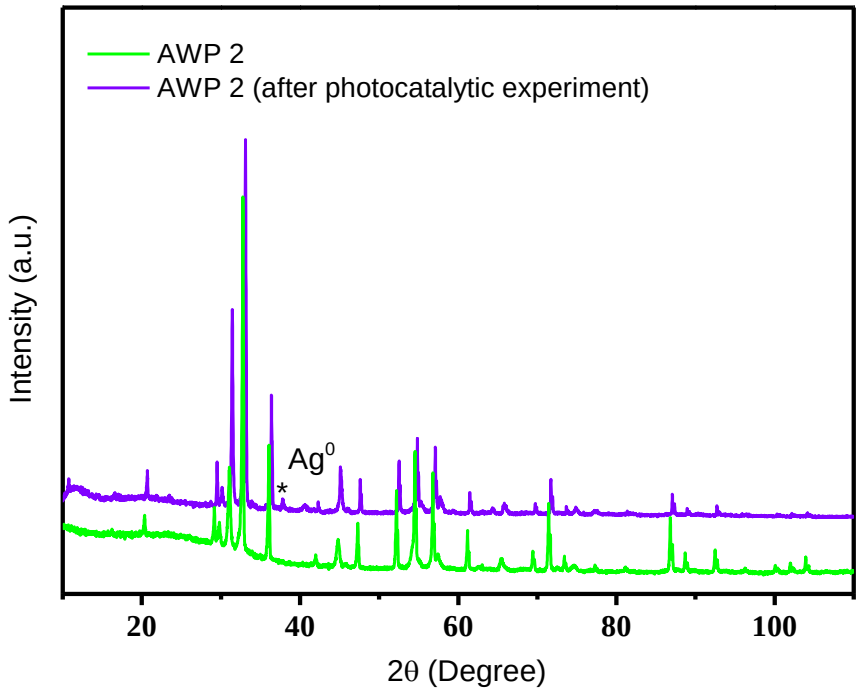

Figure S5. XRD patterns of AWP 2 sample and after fifth stability cycle.

4 – CONCLUSIONS

Doping and heterojunction formation were methodologies considered promising for improving the photocatalytic activity of Ag_3PO_4. Doping with W in the Ag_3PO_4 structure caused the formation of disordered [AgO_4], [PO_4], and [WO4] clusters, which generate intermediate energy levels in the band gap region. These energy levels delayed the electron-hole pair recombination process, increasing its availability for oxidation and reduction reactions with the reaction medium and consequently improving the material's photocatalytic performance. The material doped with 1 at% of W showed remarkable superior photocatalytic activity compared to the pure material for the degradation of Rhodamine B dye, Cephalexin antibiotic, and Imidacloprid pesticide under visible light irradiation. In addition, the presence of W in Ag_3PO_4 showed a 16-fold increase in bactericidal performance against methicillin-resistant *Staphylococcus aureus* bacteria. For heterojunction formation, it was observed that the material containing 24 wt% of α-Ag_2WO_4 showed superior photocatalytic activity for the degradation of Rhodamine B dye compared to the separated materials. According to the results of photocatalytic experiments with species scavengers, the holes showed predominant activity for the degradation of Rhodamine B, followed by the action of superoxide radicals. Based on the reduction potentials of the valence and conduction bands of α-Ag_2WO_4 and Ag_3PO_4 obtained experimentally by the Mulliken electronegativity method, a type I heterojunction charge transfer mechanism was proposed for these materials. Photoexcited electrons and photogenerated holes in α-Ag_2WO_4 migrate to the conduction band and valence band of Ag_3PO_4, respectively. This charge transfer leads to an accumulation of holes in Ag_3PO_4, which interact with Rhodamine B molecules, and also of electrons, which interact with the adsorbed O_2 to generate superoxide radical. In addition, the formation of metallic silver nanoparticles was observed at the semiconductors interface, acting as a bridge and increasing the transfer and separation of charges between the semiconductors. Thus, with the use of doping and heterojunction formation, it was possible to obtain photocatalyst materials and improve the photocatalytic properties of Ag_3PO_4.

5 – REFERENCES

[1] W.S. Koe, J.W. Lee, W.C. Chong, Y.L. Pang, L.C. Sim, An overview of photocatalytic degradation: photocatalysts, mechanisms, and development of photocatalytic membrane, Environmental science and pollution research international, 27 (2020) 2522-2565.

[2] E. Jequier, F. Constant, Water as an essential nutrient: the physiological basis of hydration, European journal of clinical nutrition, 64 (2010) 115-123.

[3] N.S.A. Mutamim, Z.Z. Noor, M.A.A. Hassan, G. Olsson, Application of membrane bioreactor technology in treating high strength industrial wastewater: a performance review, Desalination, 305 (2012) 1-11.

[4] R. Das, Application Photocatalysis for Treatment of Industrial Waste Water—A Short Review, Open Access Library Journal, 01 (2014) 1-17.

[5] C.M. Lee, P. Palaniandy, I. Dahlan, Pharmaceutical residues in aquatic environment and water remediation by TiO_2 heterogeneous photocatalysis: a review, Environmental Earth Sciences, 76 (2017).

[6] M.B. Asif, F.I. Hai, J. Kang, J.P. van de Merwe, F.D.L. Leusch, W.E. Price, L.D. Nghiem, Biocatalytic degradation of pharmaceuticals, personal care products, industrial chemicals, steroid hormones and pesticides in a membrane distillation-enzymatic bioreactor, Bioresource technology, 247 (2018) 528-536.

[7] W. Luo, M. Xie, X. Song, W. Guo, H.H. Ngo, J.L. Zhou, L.D. Nghiem, Biomimetic aquaporin membranes for osmotic membrane bioreactors: Membrane performance and contaminant removal, Bioresource technology, 249 (2018) 62-68.

[8] B. Chen, Z. Chen, S. Lv, A novel magnetic biochar efficiently sorbs organic pollutants and phosphate, Bioresource technology, 102 (2011) 716-723.

[9] K.W. Jung, K.H. Ahn, Fabrication of porosity-enhanced MgO/biochar for removal of phosphate from aqueous solution: Application of a novel combined electrochemical modification method, Bioresource technology, 200 (2016) 1029-1032.

[10] H.B. Abdullah, R. Irmawati, I. Ismail, N.A. Yusof, Utilization of waste engine oil for carbon nanotube aerogel production using floating catalyst chemical vapor deposition, Journal of Cleaner Production, 261 (2020) 121188.

[11] X. Chen, R. Tang, Y. Wang, S. Yuan, W. Wang, I.M. Ali, Z.H. Hu, Effect of ultrasonic and ozone pretreatment on the fate of enteric indicator bacteria and antibiotic resistance genes, and anaerobic digestion of dairy wastewater, Bioresource technology, 320 (2021) 124356.

[12] D.B. Miklos, C. Remy, M. Jekel, K.G. Linden, J.E. Drewes, U. Hubner, Evaluation of advanced oxidation processes for water and wastewater treatment - A critical review, Water research, 139 (2018) 118-131.

[13] R. Ameta, M.S. Solanki, S. Benjamin, S.C. Ameta, Chapter 6 - Photocatalysis, Advanced Oxidation Processes for Waste Water Treatment, Academic Press, (2018) 135-175.

[14] T. Ali, P. Tripathi, A. Azam, W. Raza, A.S. Ahmed, A. Ahmed, M. Muneer, Photocatalytic performance of Fe-doped TiO_2 nanoparticles under visible-light irradiation, Materials Research Express, 4 (2017) 015022.

[15] A. Sudhaik, P. Raizada, P. Shandilya, D.-Y. Jeong, J.-H. Lim, P. Singh, Review on fabrication of graphitic carbon nitride based efficient nanocomposites for photodegradation of aqueous phase organic pollutants, Journal of Industrial and Engineering Chemistry, 67 (2018) 28-51.

[16] S. Gisbertz, B. Pieber, Heterogeneous Photocatalysis in Organic Synthesis, ChemPhotoChem, 4 (2020) 456-475.

[17] M. Malakootian, N. Olama, M. Malakootian, A. Nasiri, Photocatalytic degradation of metronidazole from aquatic solution by TiO_2-doped Fe^{3+} nano-photocatalyst, International Journal of Environmental Science and Technology, 16 (2018) 4275-4284.

[18] X. Chen, Z. Wu, D. Liu, Z. Gao, Preparation of ZnO Photocatalyst for the Efficient and Rapid Photocatalytic Degradation of Azo Dyes, Nanoscale research letters, 12 (2017) 143.

[19] C. Sun, J. Yang, M. Xu, Y. Cui, W. Ren, J. Zhang, H. Zhao, B. Liang, Recent intensification strategies of SnO_2-based photocatalysts: A review, Chemical Engineering Journal, 427 (2022) 131564.

[20] K.K. Bera, M. Chakraborty, M. Mondal, S. Banik, S.K. Bhattacharya, Synthesis of α-β Bi_2O_3 heterojunction photocatalyst and evaluation of reaction mechanism for degradation of RhB dye under natural sunlight, Ceramics International, 46 (2020) 7667-7680.

[21] S. Adhikari, K. Sarath Chandra, D.-H. Kim, G. Madras, D. Sarkar, Understanding the morphological effects of WO_3 photocatalysts for the degradation of organic pollutants, Advanced Powder Technology, 29 (2018) 1591-1600.

[22] X. Tang, Z. Wang, Y. Wang, Visible active N-doped TiO_2/reduced graphene oxide for the degradation of tetracycline hydrochloride, Chemical Physics Letters, 691 (2018) 408-414.

[23] X. Chen, Y. Dai, X. Wang, Methods and mechanism for improvement of photocatalytic activity and stability of Ag_3PO_4: A review, Journal of Alloys and Compounds, 649 (2015) 910-932.

[24] X. Li, P. Xu, M. Chen, G. Zeng, D. Wang, F. Chen, W. Tang, C. Chen, C. Zhang, X. Tan, Application of silver phosphate-based photocatalysts: Barriers and solutions, Chemical Engineering Journal, 366 (2019) 339-357.

[25] G. He, W. Yang, W. Zheng, L. Gong, X. Wang, Y. An, M. Tian, Facile controlled synthesis of Ag_3PO_4 with various morphologies for enhanced photocatalytic oxygen evolution from water splitting, RSC Advances, 9 (2019) 18222-18231.

[26] F. Lipsky, L.H.d.S. Lacerda, S.R. de Lazaro, E. Longo, J. Andrés, M.A. San-Miguel, Unraveling the relationship between exposed surfaces and the photocatalytic activity of Ag_3PO_4: an in-depth theoretical investigation, RSC Advances, 10 (2020) 30640-30649.

[27] L.K. Ribeiro, M. Assis, L.R. Lima, D. Coelho, M.O. Goncalves, R.S. Paiva, L.N. Moraes, L.F. Almeida, F. Lipsky, M.A. San-Miguel, L.H. Mascaro, R.M.T. Grotto, C.P. Sousa, I.L.V. Rosa, S.A. Cruz, J. Andres, E. Longo, Bioactive Ag_3PO_4/Polypropylene Composites for Inactivation of SARS-CoV-2 and Other Important Public Health Pathogens, The journal of physical chemistry. B, 125 (2021) 10866-10875.

[28] Y.-J. Lee, J.-K. Kang, S.-J. Park, C.-G. Lee, J.-K. Moon, P.J.J. Alvarez, Photocatalytic degradation of neonicotinoid insecticides using sulfate-doped Ag_3PO_4 with enhanced visible light activity, Chemical Engineering Journal, 402 (2020) 126183.

[29] X. Yan, Q. Gao, J. Qin, X. Yang, Y. Li, H. Tang, Morphology-controlled synthesis of Ag_3PO_4 microcubes with enhanced visible-light-driven photocatalytic activity, Ceramics International, 39 (2013) 9715-9720.

[30] S. Zhang, S. Zhang, L. Song, Super-high activity of Bi^{3+} doped Ag_3PO_4 and enhanced photocatalytic mechanism, Applied Catalysis B: Environmental, 152-153 (2014) 129-139.

[31] L. Song, Z. Chen, T. Li, S. Zhang, A novel Ni^{2+}-doped Ag_3PO_4 photocatalyst with high photocatalytic activity and enhancement mechanism, Materials Chemistry and Physics, 186 (2017) 271-279.

[32] H. El Masaoudi, I. Benabdallah, B. Jaber, M. Benaissa, Enhanced visible light photocatalytic activity of Cu^{2+}-doped Ag_3PO_4 nanoparticles, Chemical Physics, 545 (2021) 111133.

[33] M. Afif, U. Sáulaeman, A. Riapanitra, R. Andreas, S. Yin, Use of Mn doping to suppress defect sites in Ag_3PO_4: Applications in photocatalysis, Applied Surface Science, 466 (2019) 352-357.

[34] A.B. Trench, T.R. Machado, A.F. Gouveia, M. Assis, L.G. da Trindade, C. Santos, A. Perrin, C. Perrin, M. Oliva, J. Andrés, E. Longo, Connecting structural, optical, and electronic properties and photocatalytic activity of Ag_3PO_4:Mo complemented by DFT calculations, Applied Catalysis B: Environmental, 238 (2018) 198-211.

[35] M. Al Kausor, S.S. Gupta, D. Chakrabortty, Ag_3PO_4-based nanocomposites and their applications in photodegradation of toxic organic dye contaminated wastewater: Review on material design to performance enhancement, Journal of Saudi Chemical Society, 24 (2020) 20-41.

[36] J. Low, J. Yu, M. Jaroniec, S. Wageh, A.A. Al-Ghamdi, Heterojunction Photocatalysts, Adv Mater, 29 (2017) 1-20.

[37] N. Li, J. Chen, X. Chen, Y. Lai, C. Yu, L. Yao, Y. Liang, Novel visible-light-driven $SrCoO_3/Ag_3PO_4$ heterojunction with enhanced photocatalytic performance for tetracycline degradation, Environmental science and pollution research international, 29 (2022) 9693-9706.

[38] C. Chi, J. Pan, M. You, Z. Dong, W. Zhao, C. Song, Y. Zheng, C. Li, The porous TiO_2 nanotubes/Ag_3PO_4 heterojunction for enhancing sunlight photocatalytic activity, Journal of Physics and Chemistry of Solids, 114 (2018) 173-178.

[39] N. Li, S. Miao, X. Zheng, J. Lai, S. Lv, X. Gu, M. Zhang, J. Yang, S. Cui, Construction of $Ag_3PO_4/BiNbO_4$ heterojunction photocatalysts with high activity for Rhodamine B removal under simulated sunlight irradiation, Ceramics International, 45 (2019) 24260-24268.

[40] R.K. Santos, T.A. Martins, G.N. Silva, M.V.S. Conceicao, I.C. Nogueira, E. Longo, G. Botelho, Ag_3PO_4/NiO Composites with Enhanced Photocatalytic Activity under Visible Light, ACS omega, 5 (2020) 21651-21661.

[41] H. He, S. Xue, Z. Wu, C. Yu, K. Yang, L. Zhu, W. Zhou, R. Liu, Synthesis and characterization of robust Ag_2S/Ag_2WO_4 composite microrods with enhanced photocatalytic performance, Journal of Materials Research, 31 (2016) 2598-2607.

[42] S.K. Gupta, K. Sudarshan, P.S. Ghosh, S. Mukherjee, R.M. Kadam, Doping-Induced Room Temperature Stabilization of Metastable β-Ag_2WO_4 and Origin of Visible Emission in α- and β-Ag_2WO_4: Low Temperature Photoluminescence Studies, The Journal of Physical Chemistry C, 120 (2016) 7265-7276.

[43] L.S. Cavalcante, M.A. Almeida, W. Avansi, Jr., R.L. Tranquilin, E. Longo, N.C. Batista, V.R. Mastelaro, M.S. Li, Cluster coordination and photoluminescence properties of alpha-Ag_2WO_4 microcrystals, Inorg Chem, 51 (2012) 10675-10687.

[44] N.G. Macedo, A.F. Gouveia, R.A. Roca, M. Assis, L. Gracia, J. Andrés, E.R. Leite, E. Longo, Surfactant-Mediated Morphology and Photocatalytic Activity of α-Ag_2WO_4 Material, The Journal of Physical Chemistry C, 122 (2018) 8667-8679.

[45] P.F.S. Pereira, C.C. Santos, A.F. Gouveia, M.M. Ferrer, I.M. Pinatti, G. Botelho, J.R. Sambrano, I.L.V. Rosa, J. Andrés, E. Longo, α-$Ag_{2-2x}Zn_xWO_4$ ($0 \leq x \leq 0.25$) Solid Solutions: Structure, Morphology, and Optical Properties, Inorganic Chemistry, 56 (2017) 7360-7372.

[46] F.X. Nobre, I.S. Bastos, R.O. Dos Santos Fontenelle, E.A.A. Junior, M.L. Takeno, L. Manzato, J.M.E. de Matos, P.P. Orlandi, J. de Fatima Souza Mendes, W.R. Brito, P.R. da Costa Couceiro, Antimicrobial properties of alpha-Ag_2WO_4 rod-like microcrystals synthesized by

sonochemistry and sonochemistry followed by hydrothermal conventional method, Ultrasonics sonochemistry, 58 (2019) 104620.

[47] A. Koyappayil, S. Berchmans, M.H. Lee, Dual enzyme-like properties of silver nanoparticles decorated Ag_2WO_4 nanorods and its application for H2O2 and glucose sensing, Colloids and surfaces. B, Biointerfaces, 189 (2020) 110840.

[48] B.-Y. Wang, G.-Y. Zhang, G.-W. Cui, Y.-Y. Xu, Y. Liu, C.-Y. Xing, Controllable fabrication of α-Ag_2WO_4 nanorod-clusters with superior simulated sunlight photocatalytic performance, Inorganic Chemistry Frontiers, 6 (2019) 209-219.

[49] R.A. Roca, J.C. Sczancoski, I.C. Nogueira, M.T. Fabbro, H.C. Alves, L. Gracia, L.P.S. Santos, C.P. de Sousa, J. Andrés, G.E. Luz, E. Longo, L.S. Cavalcante, Facet-dependent photocatalytic and antibacterial properties of α-Ag_2WO_4 crystals: combining experimental data and theoretical insights, Catalysis Science & Technology, 5 (2015) 4091-4107.

[50] S. Rajamohan, V. Kumaravel, R. Muthuramalingam, S. Ayyadurai, A. Abdel-Wahab, B. Sub Kwak, M. Kang, S. Sreekantan, Fe_3O_4–Ag_2WO_4: facile synthesis, characterization and visible light assisted photocatalytic activity, New Journal of Chemistry, 41 (2017) 11722-11730.

[51] P. Demircivi, E.B. Simsek, Visible-light-enhanced photoactivity of perovskite-type W-doped $BaTiO_3$ photocatalyst for photodegradation of tetracycline, Journal of Alloys and Compounds, 774 (2019) 795-802.

[52] L. Shan, H. Liu, G. Wang, Preparation of tungsten-doped $BiVO_4$ and enhanced photocatalytic activity, Journal of Nanoparticle Research, 17 (2015).